PILLAR-BASED PHONONIC CRYSTAL STRUCTURES FOR HIGH-FREQUENCY APPLICATIONS

A Dissertation
Presented to
The Academic Faculty

by

Reza Pourabolghasem

In Partial Fulfillment
of the Requirements for the Degree
Doctor of Philosophy in the
School of Electrical and Computer Engineering

Georgia Institute of Technology
May 2016

PILLAR-BASED PHONONIC CRYSTAL STRUCTURES FOR HIGH-FREQUENCY APPLICATIONS

Approved by:

Professor Ali Adibi, Advisor
School of Electrical and Computer Engineering
Georgia Institute of Technology

Professor Oliver Brand
School of Electrical and Computer Engineering
Georgia Institute of Technology

Professor F Levent Degertekin
School of Electrical and Computer Engineering
Georgia Institute of Technology

Professor Azad Naeemi
School of Electrical and Computer Engineering
Georgia Institute of Technology

Professor Laurence J Jacobs
School of Civil and Environmental Engineering
Georgia Institute of Technology

Date Approved: 11 December 2015

To my father,

Yousef.

ACKNOWLEDGEMENTS

First and foremost, I would like to thank my doctoral advisor, Prof. Ali Adibi, for his continuous support throughout my time at Georgia Tech and for his trust in me to work on the fascinating topic of phononic crystals. This work wouldn't have come to fruition without Prof. Adibi's extensive experience in the field, his high standard for academic achievement, and his acumen in guiding the direction of this research project.

I would also like to thank my Ph.D. committee members, Prof. Oliver Brand, Prof. F Levent Degertekin, Prof. Azad Naeemi, and Prof. Laurence J Jacobs, for their dedication in reviewing this dissertation and their valuable suggestions to further the depth and impact of this project.

When I embarked on this journey, given my background in electronics, I had to start from the basics of phononics and mechanics of elastic waves in solids. I was lucky to have Dr. Abdelkrim Khelif, one of the pioneers in the field, in our group to make this transition seamless. Many of the initial ideas in this work are the outcome of our collaboration with Dr. Khelif.

This work, in many ways, is the continuation of the pioneering work of Dr. Saeed Mohammadi on the properties of the hole-based phononic crystal membranes. The initial period of my Ph.D. research coincided with Dr. Mohammadi's presence in our group as a Ph.D. candidate and then a post-doctoral fellow. His mentorship and vast experience in the experimental and theoretical aspects of the field provided the necessary foundation for this research getting off the ground.

I wish to thank Dr. Reza Eftekhar for offering his constant guidance and support during this research. His help in guiding the direction of this work, his suggestions

in overcoming the obstacles, and his experience in recognizing high-impact research opportunities were all instrumental in this research.

I would like to thank my colleague and good friend, Razi Dehghannasiri, for his collaboration in the later part of this work. Razi's suggestions in the design and simulation stage, as well as his help in the fabrication phase have been invaluable in the successful outcome of this work.

I would like to acknowledge the efforts of the IEN staff, specially Devin Brown, in managing and keeping the Georgia Tech's cleanroom facilities operational. The experimental parts of this work would not have been possible without their exceptional work.

I am specially grateful to my senior colleagues at photonics research group who mentored me and taught me the basics of fabrication, including Payam Alipour, Amir Atabaki, Maysam Chamanzar, Ehsan Shah Hosseini, and Qing Li. My special thanks goes to Majid Sodagar for generously offering his expertise and time, without which the fabrication of the phononic waveguides would have progressed much slower. I would also like to express my gratitude to Hesam Moradinejad, who kindly offered his help and suggestions in time of fabrication difficulties. I express my gratitude to my friends, Hossein Taheri, Hossein, and Mohammad Taghinejad, who kindly offered their help in proof-reading this dissertation.

I wish to acknowledge the camaraderie of my friends, Farshid Ghasemi, Ali Behrooz, Amirhossein Hosseinnia, Hamed Mousavi, Roozbeh Tabrizian, Mohsen Sardari, and Ahmad Beirami. Their friendship turned my time at Georgia Tech into a memorable period of my life.

None of this would have happened if it wasn't for the support and love of my family. I can never thank my dear wife, Sara, enough for her constant support and sacrifice, and her endless encouragements and unconditional love. Her companionship every step of the way was the source of strength and optimism during this journey.

Most of all, I would like to thank my parents and my sisters, Shabnam and Parisa, for providing a home for me lit with love and life. I am deeply grateful for having them in my life.

TABLE OF CONTENTS

LIST OF FIGURES

SUMMARY

The physical mechanisms of phononic bandgap (PnBG) formation in the pillar-based phononic crystals (PnCs) are theoretically studied. The comparison of PnBGs in three different lattice types (i.e., square, triangular, and honeycomb) with different pillar geometries shows that different PnBGs have varying degrees of dependency on the lattice symmetry based on the interplay of the local resonances and the Bragg effect. The details of this interplay are discussed. The significance of locally resonating pillars on PnBGs is discussed and verified by examining the PnBG position and width in perturbed lattices. It is shown that the PnBGs caused by the local resonance of the pillars are more resilient to the lattice perturbations than those caused by Bragg scattering. Furthermore, strong experimental evidence is presented for the existence of a complete phononic bandgap, for Lamb waves, in the high frequency regime (i.e., 800 MHz) for a pillar-based PnC membrane with a triangular lattice of gold pillars on top. The results of experiments are analyzed, and the physics behind the attenuation in different spectral windows is explained methodically by assessing the type of Bloch modes and the in-plane symmetry of the displacement profile. In addition, a theoretical design for a waveguide/resonator device operating at the GHz frequency range based on the pillar-based PnC membranes is presented and experimental evidence is provided for the waveguiding property of the proposed structure. Additionally, several designs for surface acoustic wave (SAW) PnCs and PnC-based waveguides are introduced and theoretically studied. These designs are optimized to provide low radiation loss and high design flexibility in terms of engineering the frequency and the number of guided modes.

CHAPTER I

INTRODUCTION

Phononic crystals [18, 44, 51, 64, 75] (PnCs) are synthetic periodic structures with vibrational properties that can be significantly different from their constituent bulk materials. PnCs can display interesting properties ranging from sound isolation for meter-scale structures [43] to heat conduction manipulation for sub-micron feature sizes [13]. This flexibility in a mechanical structure as PnCs is due to the fact that PnCs, if carefully designed, can exhibit phononic (acoustic) stop bands (also known as bandgaps) in which no propagating mechanical wave can exist [22, 31]. In other words, PnCs can block the propagation of mechanical waves within a certain range of frequencies, also known as phononic bandgaps (PnBGs).

PnCs are similar to their optical counterpart, photonic crystals [19, 20, 42], in that they can also be scaled down in order to adjust the frequency of the PnBGs; hence, broadening its use in the whole spectrum of the acoustic waves. Silicon-based PnCs are especially interesting owing to the well-established silicon (Si) fabrication techniques — widely used in the CMOS technology and micro-electromechanical systems (MEMS) — and its potential for integration with the electronic circuits on a single chip. This property makes PnCs a viable choice for the design and fabrication of compact on-chip signal processing units including RF filters [27], resonators [16, 17, 49, 50, 79], waveguides [26, 52, 70], and multiplexers/demultiplexers [47, 57].

Formation of PnBGs in the PnCs is governed by two physical effects: 1) the destructive superposition of the waves scattered from the periodic features of the PnC (also known as Bragg scattering [4]) and 2) the resonance of the structural features of the PnC that are coupled through the host material [15, 41]. According

to Bragg scattering, shrinking the lattice constant and the geometrical dimensions of the structure results in a proportional increase in the frequency of the PnBGs, and therefore a scale-up in the operation frequency of the device. This has been the main strategy for designing a PnC device for a certain target frequency. The second phenomenon offers another method to adjust the center frequency of the PnBGs, and that is through designing periodic features, such as inclusions in a host material, resonating at certain frequencies. This scheme can potentially eliminate the need to scale up or down the whole structure of the PnCs, while providing the ability to engineer their operation frequency. However, the effects of the aforementioned physical factors are not equally weighted in different PnCs. An extreme example is the hole-based PnC [46, 48] that has no resonating periodic feature to contribute to the formation of PnBGs. These physical and geometrical constraints make the effective use of the locally resonant features in the engineering of the PnCs a non-trivial practice.

To better understand the physics of the PnCs, researchers have long been interested in calculating the elastic dispersion properties of them [4, 28]. The calculated dispersion diagrams (also known as band structures) provide a glimpse of the different eigenmodes of the PnC as well as the relation between the eigenfrequency and the corresponding wave number. Furthermore, band structures give us an overview of the pass bands and the stop bands (i.e., PnBGs) of the structure. In the early 1990s, researchers embarked on the theoretical study of the elastic properties of composite periodic structures [65] in search of PnBGs. Two-dimensional (2D) arrangement of solids, fluids, or voids in a host material (with the third dimension assumed to be infinite) were among the first PnCs theoretically proven to support PnBGs [30, 31, 33, 34, 43, 63].

In addition to the 2D structures, several other structures have been proposed as alternative PnCs. For example, three dimensional (3D) arrangement of inclusions (or

voids) in a host material is one type of PnCs that can control the propagation of bulk waves in a 3D medium. The existence of the PnBGs for the 3D PnCs are theoretically studied [22, 32] and for truncated structures experimentally demonstrated [41].

2D PnCs have been used in MEMS devices to guide confined acoustic waves [52] and to isolate the elastic vibrations [6]. However, these structures have remained mostly a theoretical curiosity because of the inherent geometrical assumption that is used in designing these structures and that is having an infinitely thick or infinitely thin structure [11]. As mentioned earlier, truncated 3D PnCs have been experimentally demonstrated to support PnBGs [41]; however, fabricating layers of scatterers embedded in a host material does not lead to cost efficient devices, especially for high-frequency applications. To address these practical limitations, other categories of PnCs have been proposed. For example, PnCs based on the propagation of surface acoustic waves (SAWs) on a half-space (semi-infinite) structure can mitigate the geometric limitation of the 2D PnCs and the fabrication challenges of 3D PnCs [37, 71]. Because of the finite penetration depth of the SAW modes, truncating the semi-infinite substrate does not lead to major perturbations in these structures [7]; therefore, SAW-based PnCs can be a practical alternative to the two- and three-dimensional PnCs. The third category of PnCs is based on the propagating lamb waves in a membrane with periodic holes or inclusions [23, 35, 46, 48]. These structures provide complete 3D energy confinement along with a feasible fabrication process for high frequency applications.

Tailoring the properties of the PnBGs in membrane-based PnCs is only possible via designing the geometrical shape of the holes and changing the thickness of the membrane—and the choice of the material for fillings, in the case of inclusions. This can limit the utility of the membrane-based PnCs as the shape of the holes and the thickness of the membrane may not provide enough flexibility in the design of PnBGs. To mitigate this limitation, a new class of PnCs based on depositing a periodic array

of pillars on a host material (either a membrane or a semi-infinite substrate) has been introduced [53, 56, 58, 77, 78]. More specifically, pillar-based PnC membranes are Lamb-wave-based structures composed of a continuous host material (membrane with possibly multiple layers) with periodic pillars (also known as stubs) on top arranged in two-dimensional (2D) lattice (e.g., square, triangular, or honeycomb).

These structures provide three-dimensional (3D) elastic wave confinement through (1) 2D nature of Lamb waves and (2) in-plane confinement resulting from PnBGs. This is in contrast to the 3D PnCs [22, 41], the fabrication process of which can be challenging. However, as mentioned earlier, pillar-based PnCs can also be formed on half-space structures based on the propagation of SAW modes [3]. Even though the existence of PnBGs in such SAW-based devices and low-loss SAW-based PnCs have been experimentally demonstrated [1], the potential coupling of the SAW modes to the bulk acoustic modes of the half-space [69] by the PnC defects (e.g., waveguide bends or point defects that form resonators) can limit the flexibility of the SAW-based PnCs in forming functional PnC-based devices such as waveguides and resonators. On the other hand, the 2D confinement of elastic waves in the PnC membranes can make the design of low-loss devices easier when compared to the SAW-based PnCs [7, 25].

In comparison to other membrane-based PnCs (i.e., membranes with periodic holes or inclusions) [23, 35, 46, 48], pillar-based PnCs offer more design parameters (i.e., height of pillars and the choice of the material for pillars) and greater flexibility in designing PnCs using specific physical properties of the pillars [72], including the possibility of designing PnCs based on the local resonance of the pillars [2, 24, 54, 59]. Pillar-based PnCs have a new geometrical parameter (i.e., the height of the pillars) that can be used, along with other geometrical parameters, to adjust the frequency of the acoustic modes and consequently, the position of the PnBGs [2, 24, 58].

Previous studies show that several factors—including the height of the pillars and their lattice type—affect the formation and position of the PnBGs [59]. In addition,

the presence of the pillars introduces local resonances that can affect the properties of these PnCs, and this makes the physics of propagation and confinement of the acoustic waves in pillar-based PnCs more complex than the hole-based PnCs. Thus, to leverage these properties in designing the PnC devices, further understanding of the physical mechanisms governing the behavior of pillar-based PnCs is required.

While experimental results for ultrasonic PnBGs in pillar-based structures have been reported, these results are not in the ultra high-frequency regime [2, 18, 75]. Nevertheless, other PnCs have been shown to support PnBGs in the ultra high-frequency range [5, 12, 66, 67]. Su et al. have shown that a PnC membrane of periodic tungsten (W) inclusions in a silicon dioxide (SiO_2) membrane supports a directional PnBG in the 600 MHz–1 GHz frequency range along the Γ–X direction of the square lattice. Soliman et al. improved this result by demonstrating a directional PnBG in the 1 GHz–1.7 GHz frequency range using W inclusions in a silicon (Si) membrane. Furthermore, hole-based PnC membranes composed of an aluminum nitride (AlN) membrane [29] and a stacked AlN and SiO_2 membrane [12] have been shown to have PnBGs around 800 MHz, 900 MHz, and 1.1 GHz along the Γ–X direction of the square lattice. Considering the flexibility of the pillar-based PnC membranes (in terms of design parameters) and the high utilization of the 800 MHz–1 GHz frequency range in wireless applications, it is important to demonstrate functional pillar-based PnCs with PnBGs at this frequency regime.

Designing and fabricating PnCs with ultra high-frequency PnBGs are only the first step in developing a complete signal processing platform based on PnCs at this frequency regime. The next logical step is to develop the frequency selective building blocks (e.g., resonators [50]) along with the devices that can carry the acoustic waves (i.e., waveguides [45, 70]). These building blocks can be combined by coupling the acoustic waves between waveguides [68], resonators [27], or a combination of the two [47]. In addition to the frequency scaling and the micro-fabrication challenges that

ensue, one major improvement opportunity looms for the integration of the acoustic waveguides that are part of a larger system, and that is the efficient coupling of the acoustic energy generated by a plane-wave transducer to the waveguides in the system. Several theoretical studies have shown that using a specialized PnC-based structure known as the gradient index (GRIN) waveguide can improve the coupling efficiency of a plane-wave source to a PnC-based waveguide [38, 39, 74]. However, experimental demonstrations of ultra high-frequency functional GRIN waveguides are yet to be reported.

The objective of this work is to study the physical mechanisms of PnBG formation in the pillar-based PnCs, theoretically and experimentally, and to utilize this understanding in designing the building blocks of a signal processing platform based on the pillar-based PnCs.

Initially, we present a systematic theoretical study of the PnC structure composed of an array of cylindrical tungsten (W) pillars deposited over a silicon (Si) plate. The existence of PnBGs in three different symmetries (square, triangular, and honeycomb) will be theoretically shown, and the effect of lattice symmetry on the PnBGs will be discussed. It will be shown that the triangular lattice is the favorable symmetry system for the pillar-based structure to provide the widest bandgaps, which is in contrast to the hole-based 2D PnCs that have the largest PnBG in the honeycomb lattice [46]. It will also be shown that introducing the 4th parameter (i.e., the height of pillars) into the design space can alleviate the fabrication challenges associated with the high filling fraction observed in the previous PnC designs. The choice of Si/W material system is due to the good mechanical impedance mismatch between Si and W, which is crucial for opening PnBGs [52].

To better understand the factors affecting PnBGs, the physical mechanisms that control the formation of PnBGs in pillar-based PnCs are investigated in detail. Specifically, the individual roles and the interplay of two dominant physical mechanisms in

these structures are studied. These two dominant physical mechanisms are 1) Bragg scattering [4]; and 2) resonance of the structural features of the PnCs (i.e., pillars) coupled through the host material [35, 41, 53]. The theoretical evidence—based on numerical calculations—of the effect of Bragg scattering and local resonance for pillars arranged in different lattice types is presented, and the geometrical regimes, where each is the dominant factor, are identified. Using this understanding, the effects of design parameters on the formation of PnBGs are theoretically investigated, and the robustness of PnBGs in these PnCs against geometrical perturbation caused by fabrication imperfection is discussed.

Following the theoretical study of PnBGs in the pillar-based PnCs, the experimental demonstration of pillar-based PnC membranes supporting complete PnBGs in the ultra high-frequency regime is presented. The PnBGs in three major crystallographic directions are characterized, and the observed extent of these PnBGs is found to be around 800 MHz. These findings are compared and justified with the theoretical predictions provided by simulations performed using the finite element method (FEM). It should be noted that to accommodate for the practical implications of the piezoelectric transduction, the structural integrity of the device, and the feasibility of the fabrication process, a modified version of the material system is used for the experimental demonstration, the details of which will be discussed accordingly.

To account for the apparent discrepancies between the experimental results and the theoretically expected outcome, a theoretical analysis methodology based on the comparison of the polarizations of the Bloch modes of the PnC, their symmetry, and those of the acoustic wave source is developed. This methodology enriches our theoretical understanding of the PnCs and helps us to accurately explain the experimental results.

After experimental demonstration of the ultra high-frequency PnBGs in the pillar-based PnCs, a waveguide design based on the pillar-based PnC membrane is theoretically studied, and the conditions on the geometrical parameters for its optimal operation are discussed. This design serves as the starting point for the experimental demonstration of ultra high-frequency waveguide structures formed using pillar-based PnC membranes. Specifically, a new design for a pillar-based PnC membrane is introduced that supports a PnBG at 1.1 GHz. This design is used to develop a waveguiding device in the GHz frequency range. The experimental evidence is provided that demonstrates the existence of waveguiding effect in the proposed device.

To optimize the coupling of the generated acoustic waves, a new design and simulation methodology is developed to enable the focusing of the acoustic energy into the aperture of the waveguides being characterized [36, 61, 73, 76]. The effectiveness of this design is shown experimentally, as well.

Built upon the successful demonstration of the waveguiding effect, two reference resonator designs are introduced. The physical mechanisms underlying each design is introduced, and the advantage of each is discussed. Furthermore, effective excitation methods for each of these designs are introduced, and the effectiveness of these techniques are validated through numerical simulations.

Finally, a reference design is presented for a pillar-based SAW PnC. The proposed design has a similar material platform used in the experimental demonstration of the pillar-based PnC membranes. Based on these SAW PnCs, several practical waveguide designs are introduced and theoretically studied. These SAW-based waveguide designs are step-by-step optimized in order to satisfy three design criteria: 1) controllability of the lateral confinement of the waveguide modes as well as their penetration depth, 2) feasibility of direct excitation of the waveguide, and 3) providing multitude of design parameters to enable the engineering of the number of the waveguide modes and their frequencies.

Given the straightforward fabrication process of SAW PnCs and their structural rigidity, and despite their potential for radiation loss, the SAW-based PnC and waveguide structures can prove valuable in realizing the final objective of developing functional and low-cost signal processing building blocks based on the pillar-based PnCs.

CHAPTER II

PILLAR-BASED PNC MEMBRANES

The structure of the planar pillar-based PnCs realized in square, triangular, and honeycomb lattices along with their corresponding primitive cells and reduced Brillouin zones are shown in Figs. 1(a)–1(c), respectively. To theoretically study the PnBGs in pillar-based PnCs, the substrate is chosen to be Si and the cylindrical pillars are W. The reduced Brillouin zone for the triangular and honeycomb lattices are chosen by considering both the PnC lattice symmetry and the anisotropy of the mechanical properties of the Si plate. As shown in Fig. 1, the x, y, and z directions represent the crystallographic directions of the Si substrate.

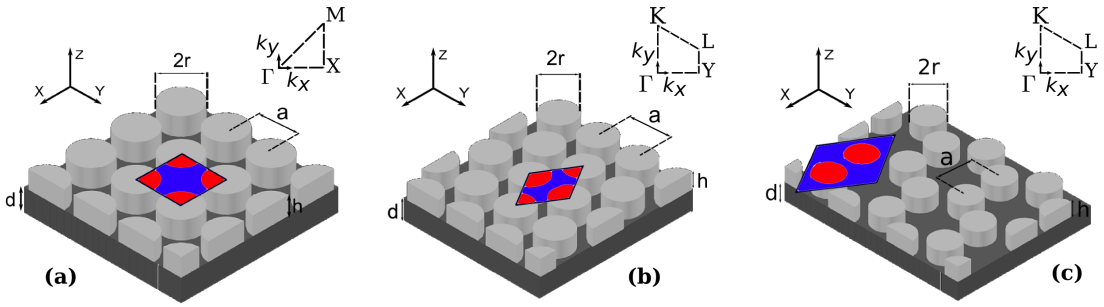

Figure 1: Schematic, unit cell, and the reciprocal lattice of the pillar-based PnCs with (a) square, (b) triangular, and (c) honeycomb lattice types. The lattice constant, radius and height of pillars, and the membrane thickness are denoted as a, r, h, and d, respectively. The x, y, and z coordinate directions are aligned with the crystallographic directions of the membrane material (i.e., Si).

The numerical simulation technique used for the calculation of the phononic band structure of the PnCs is based on the FEM implemented using the COMSOL Multiphysics® software package. The underlying physical model is based on the following equation:

$$\nabla \times (c \times \nabla_s u) = \rho \frac{\partial^2}{\partial t^2} u, \tag{1}$$

where c is the stiffness matrix, ρ is the mass density, and u is the displacement vector. The nonzero stiffness tensor parameters and the material density used in these calculations for Si are as follows: $c_{11} = 16.6 \times 10^{10}\,\mathrm{N/m^2}$, $c_{12} = 6.4 \times 10^{10}\,\mathrm{N/m^2}$, $c_{44} = 8.0 \times 10^{10}\,\mathrm{N/m^2}$, and $\rho = 2330\,\mathrm{kg/m^3}$. The corresponding values for W are $c_{11} = 52.5 \times 10^{10}\,\mathrm{N/m^2}$, $c_{12} = 20.5 \times 10^{10}\,\mathrm{N/m^2}$, and $\rho = 19300\,\mathrm{kg/m^3}$. The 2D periodic structure is modeled using the Bloch-Floquet periodic boundary conditions (BCs) in the $x - y$ plane [37], and the band structure is calculated by repeatedly applying these BCs (dictated by the wave vectors along the reduced Brillouin zone boundary, as depicted in Fig. 1) and calculating the mode frequencies for each wave vector [58].

2.1 Phononic Bandgap: Evidence of Bragg Scattering and Local Resonance

The band structure of three lattice types (i.e., square, triangular, and honeycomb) is calculated using FEM for the Si/W material system. The geometrical parameters used in the simulation are as follows: $r = 0.4a$, $h = 0.4a$, and $d = 0.5a$, where a, r, h, d are lattice constant, pillar radius, pillar height, and membrane thickness, respectively. The corresponding band diagrams are shown in Figs. 2(a)–2(c). These geometrical parameters are chosen to represent a typical design, where the aspect ratios are close to unity and the structure supports wide PnBGs. As seen in Figs. 2(a)–2(c), for the square and the triangular lattices, a wide PnBG can be opened around the normalized frequency of $f.a = 2000$ m/s. The ratio of the bandgap width (upper edge − lower edge) to the center frequency of the gap is around 40%. This gap-to-midgap ratio is sufficient for almost all practical applications including resonators and filters designed for wireless systems. Figure 2(c) shows the band structure of the PnC structure with honeycomb lattice demonstrating the existence of two narrower bandgaps around $f.a$ 1700 m/s (gap-to-midgap ratio $\approx$ 5%) and $f.a$ 2200 m/s (gap-to-midgap ratio $\approx$ 10%) for this lattice. Other narrow bandgaps can also be seen for triangular and

honeycomb lattices around 1000 m/s and 600 m/s, respectively.

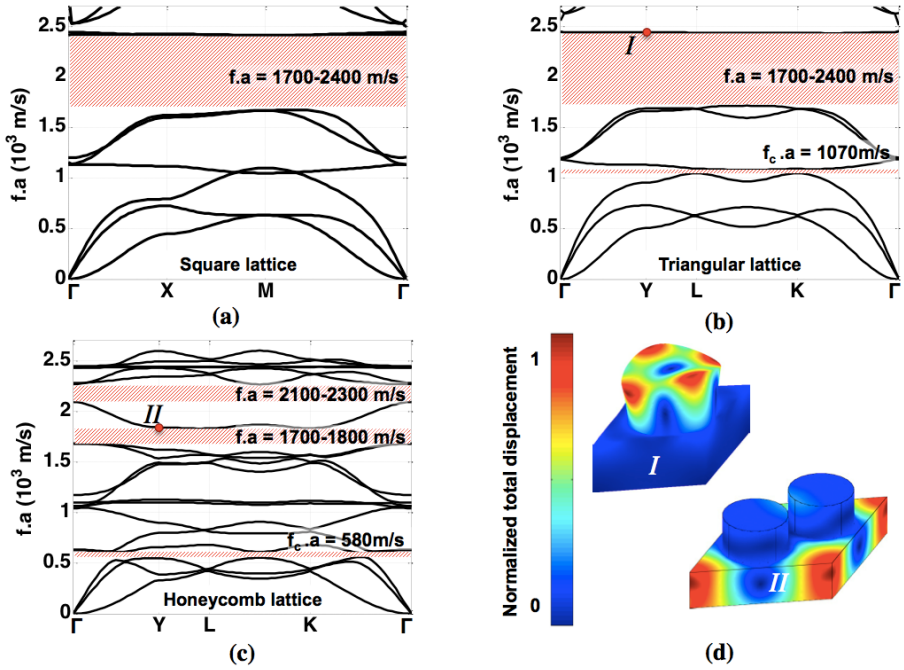

Figure 2: Band structure of a pillar-based PnC for (a) square lattice, (b) triangular lattice, and (c) honeycomb lattice with W pillars and Si membrane. The corresponding geometrical parameters are as follows: $r/a = 0.4$, $h/a = 0.4$, and $d/a = 0.5$. The extent of PnBGs are highlighted by the shaded regions. (d) The displacement profile of modes I and II as marked in (b) and (c), respectively.

In order to study the effect of Bragg scattering and local resonance in pillar-based PnCs, the similarities and differences among the PnBGs of the three studied PnC lattices, as shown in Fig. 2, can be examined. For example, a first narrow gap is observed around the normalized frequency of $f.a = 1070$ m/s for the triangular lattice and around $f.a = 580$ m/s for the honeycomb lattice (this PnBG occurs between the third and fourth branches of the dispersion diagram of these structures with each branch represented by one curve in the band structure). A more important observation is that the ratio of the center frequencies of this first PnBG in the two lattices is approximately $\sqrt{3}$ (with 94% accuracy). In Sec. 2.2, it will be discussed that this ratio is the inverse of the lattice period ratio between triangular (a) and honeycomb ($a \times \sqrt{3}$) lattices, as predicted by the Bragg scattering principle [4]. This

class of PnBGs will be referred to as the first PnBG. It should be mentioned that, with the chosen geometrical parameters, the third and fourth branches of the square lattice PnC intersect with each other and, therefore, this lattice does not support this first PnBG.

At higher frequencies, square and triangular lattice PnCs support a wide PnBG in the normalized frequency range of $f.a$ = 1700–2400 m/s. Honeycomb lattice, on the other hand, supports two PnBGs int the same range; the first one spanning in the $f.a$ = 1700–1800 m/s range and the second one in the $f.a$ = 2100–2300 m/s range with a single branch separating the two PnBGs. While this single branch between the two PnBGs makes the distinction with the other lattice types, the combined range of these two PnBGs are otherwise very close to the single PnBG in other lattice types. This behavior is in contrast with the expected behavior of Bragg-based PnBGs (as predicted by Bragg principle) and does not exhibit the same dependency on the lattice period as the first PnBG does.

The difference between the first PnBG and the higher-frequency PnBGs shows that Bragg scattering cannot accurately explain the properties of all the PnBGs in the structure and therefore, a second physical phenomenon must affect the behavior of these higher-frequency PnBGs. This phenomenon is due to the local resonance of the individual pillars in the PnC structure. The effect of the local resonance in the formation of high-frequency PnBGs can be verified by examining the mode shape of the structure in the branches surrounding these PnBGs.

Figure 2(d) depicts two sample displacement profiles for triangular and honeycomb lattices, both at the high symmetry point Y, as labeled in the corresponding band structures with I and II [see Figs. 2(b) and 2(c)], respectively. In Fig. 2(d), mode profile I shows the displacement field of the triangular lattice at point Y for the upper edge of the second (high-frequency) PnBG, and mode profile II shows the displacement field of the honeycomb lattice at point Y for the branch crossing the two

adjacent (high-frequency) PnBGs. As seen in these mode profiles, mode I has a large displacement in the pillar region, thus, having a larger portion of its elastic energy density in the pillar part. On the contrary, mode II has a large displacement (and, therefore, greater elastic energy density) in the membrane region. Since the energy of the mode I is mostly concentrated in the pillar region, this mode is expected to have little variation with the lattice type as long as the pillar geometry does not change. This is, therefore, the reason that branches surrounding the high-frequency PnBGs of the square and triangular lattice PnCs and those surrounding the second and third PnBGs in honeycomb lattice PnC in Fig. 2 look similar.

As for the middle branch in the honeycomb lattice, which includes mode II in Fig. 2(c), since it is a mode with its energy concentrated in the substrate, its behavior is more prone to changes in the periodicity of the structure. This is the reason that this branch for the honeycomb lattice is not present in the other two lattices. The similarity of the high-frequency PnBG (in the normalized frequency range of $f.a$ = 1700–2400 m/s) in all lattice types is due to the local resonances of the pillars rather than the Bragg effect, which results from the periodicity of the PnCs.

2.2 Effect of Pillar Geometry

As discussed earlier, one feature of the pillar-based PnCs is introducing the 4th geometrical parameter (h) to the design space (as compared to the hole-based PnCs [72]). In order to further investigate the effect of this parameter in opening PnBGs, the evolution of PnBGs (also known as gap maps) for the 3 lattices are studied in this section. Figure 3 shows the evolution of the PnBG openings as the height of pillars increase for the 3 lattice types with $d = 0.5a$, and $r = 0.4a$. As seen from Fig. 3, several PnBGs exist for each lattice type. It is also observed that the PnBGs are generally wider for the square and triangular lattices. On the other hand, triangular and honeycomb lattice PnCs have more gaps than the square lattice in a given frequency

range. These results suggest that triangular lattice outperforms the other two lattice types in terms of the width and the number of gaps opened.

From Fig. 3, it is also obvious that by increasing the height of W pillars, the center frequency of PnBGs decrease. Specifically, it can be seen that increasing the pillar height decreases the frequency of the upper and lower edges of the PnBGs. The $\sqrt{3}$ relationship between the first PnBG (denoted by B1) in the honeycomb and triangular lattices — imposed by the Bragg effect and mentioned in the Sec. 2.1 — can also be observed. For example, for the pillar with $h/a = 0.3$, the normalized center frequency of the first PnBG, for the triangular lattice PnC, is ≈ 1250 m/s; and for the honeycomb lattice PnC, it is ≈ 700 m/s. This gives the ratio of 1.79, which is within 5% of the expected $\sqrt{3}$.

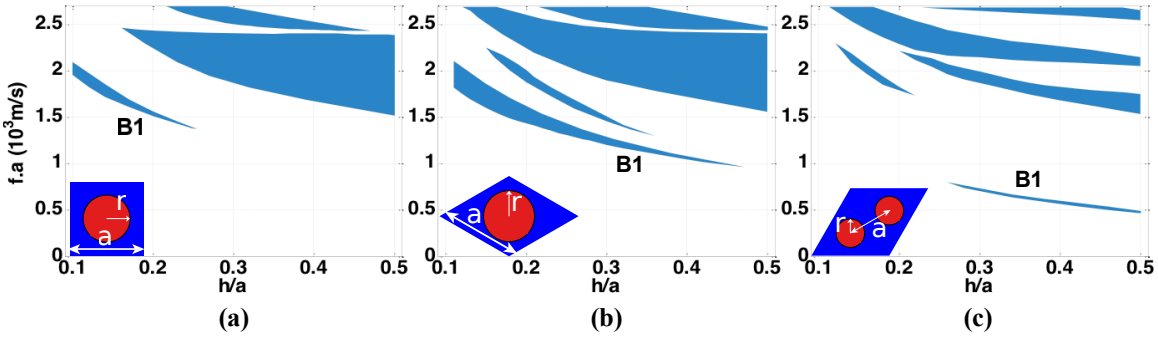

Figure 3: Evolution of the PnBGs in pillar-based PnCs with respect to the normalized height of pillars (h/a) in (a) square, (b) triangular, and (c) honeycomb lattices with W pillars and Si membrane. Normalized radius of the pillars (r/a) and the membrane thickness (d/a) are 0.4 and 0.5, respectively. The extent of the PnBGs is shown by the shaded region.

Moreover, it can be observed that for the square and triangular lattices, the ratio between the center frequency of the first PnBG (B1) is unity. For example, for the pillar with $h/a = 0.2$, the normalized center frequency of the first PnBG for both the triangular and square lattice PnCs is ≈ 1550 m/s. This is consistent with the previous argument, as the lattice periods of these two structures are the same (equal to a).

The difference between the three lattice types in having different ranges of h/a values that open the B1 PnBG is not unexpected. Generally, certain symmetries may be more favorable for opening certain PnBGs (specially, those caused by the Bragg effect, which is the case here) for a specific geometric structure [48, 58]. In the case of pillar-based PnCs, the triangular lattice PnC provides the most favorable symmetry for opening the B1 PnBG in a wide range of h/a values [58].

The decreasing trend of the center frequency of the PnBGs with increasing the pillar height (Fig. 3) indicates that the vibrational properties of the cylindrical pillars have a distinguishable effect on the position and formation of the PnBGs. This decreasing trend can be explained by observing that the resonance frequency of a pillar in the structure tends to decrease as its length increases [62]. The dependence of the PnBGs on the pillar height in the PnCs suggests that the formation of PnBGs in these structures is affected by the local resonance of the pillars.

It is important to note that this decreasing trend in the position of the PnBGs can not be explained by a lumped model of the unit cell and relying on an argument based on the increasing mass of the pillar. This can be verified by examining the evolution of the PnBGs in these structures with respect to the radius of the pillars as shown in Fig. 4. It is seen in Fig. 4 that increasing the radius of the pillars does not have any consistent effect on the position of the PnBGs.

Figure 4 shows that the first PnBG in the triangular and honeycomb lattices — which was argued that they follow the frequency ratio predicted by the Bragg effect — does not observably change its center frequency as the radius of the pillar increases. Based on the lumped model assumption, as the radius of the pillar increases, the total mass of the unit cell increases; and this should effectively decrease the group velocity of the elastic waves propagating in the membrane and, therefore, scale down the center frequency of the first PnBG. Nevertheless, the center frequency of the first PnBG does not decrease as the radius of the pillars increases. If the effect of

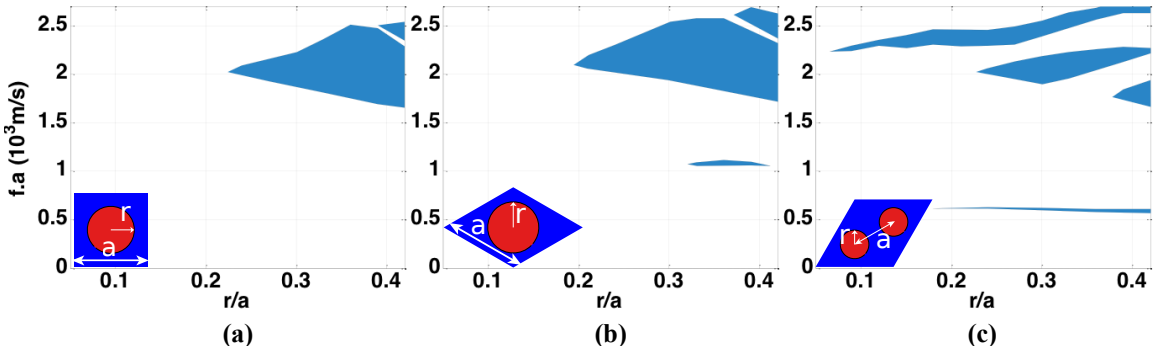

Figure 4: Evolution of the PnBGs in pillar-based PnCs with respect to the normalized radius of pillars (r/a) in (a) square, (b) triangular, and (c) honeycomb lattices with W pillars and Si membrane. Normalized height of the pillars (h/a) and the membrane thickness (d/a) are 0.4 and 0.5, respectively. The extent of the PnBGs are shown by the shaded region.

the local resonance of the pillars on the formation of the PnBGs in these structures is also considered, it can be argued that as the radius of the pillars increases, the resonance frequency of the pillars increases [62] as well. As the decreasing impact on the frequency of the PnBG derived from the lumped model along with the increasing impact of the local resonance of the pillar compete with each other, no substantial change in the center frequency of the first PnBG is seen in Figs. 4(a) and 4(b).

The same argument holds for the higher-frequency PnBGs. The center frequency of the second PnBG of the square and triangular lattice PnCs exhibits a slightly increasing trend for lower r/a values, and as r/a increases this trend changes to a decreasing one [see Figs. 4(a) and 4(b)]. This suggests that, initially, the effect of mass in the lumped model is dominating the physics of the PnBG formation, and as r/a increases, the local resonance becomes the dominant effect. For the honeycomb lattice PnC, all the higher-frequency PnBGs exhibit an increasing trend as the radius of the pillars increases [see Fig. 4(c)]. This suggests that for the range of r/a values in this study, the local resonance of the pillars dominate the formation of the PnBG in the honeycomb lattice at higher normalized frequencies.

It should be noted that the argument based on the combination of the lumped

model and the local resonance of pillars does not lead to competing effects as the height of the pillars increases. In other words, as h/a increases, the mass of the pillar increases leading to lower elastic-wave velocity and lower center frequency of the PnBGs; similarly, higher h/a values lead to a lower resonance frequency of the pillars and contribute to the lower center frequency of the PnBGs. Therefore, an increase in the mass of the unit cell can not necessarily explain the changes in the position of the PnBGs; it is the effect of local resonance of the pillars that can explain the decreasing (or increasing) trend of the center frequency of the PnBGs in certain geometrical regimes.

As an extreme case, Fig. 5 shows the band structure of the pillar-based PnCs where the height of the pillars is increased to five times the lattice constant (i.e., $h/a = 5$). Figure 5 shows that the PnBGs in all three lattice types have identical lower and upper edges. The normalized center frequency of these PnBGs occurs at $f.a \approx 300$ m/s, and the gap width (ratio of the PnBG extent to its center frequency) is ≈20%. As shown earlier, the theoretical Bragg PnBG is around 2100 m/s for the square and triangular lattices and around 1200 m/s for the honeycomb lattice. Therefore, the observed PnBGs in these structures are much lower than the Bragg PnBG.

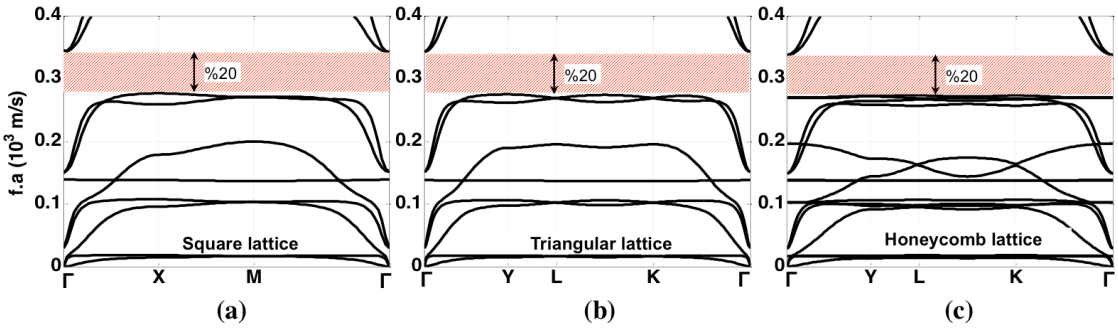

Figure 5: Band structure of a pillar-based PnC for (a) square lattice, (b) triangular lattice, and (c) honeycomb lattice with W pillars and a Si membrane. The corresponding geometrical parameters in all lattices are as follows: $r/a = 0.4$, $h/a = 5.0$, and $d/a = 0.5$. The extent of the PnBGs are highlighted by the shaded regions.

These identical PnBGs also can be attributed to the dominant effect of the local resonance of the pillars compared to the effect of Bragg scattering and lattice periodicity. To corroborate this statement, Fig. 6 compares the mode profiles in the unit cell of a square lattice PnC with those of the individual pillars with the same height and radius as those in the case of tall pillars (i.e., $h/a = 5.0$ and $r/a = 0.4$). The displacement profiles of the first five distinct modes at the high symmetry point M in a square lattice with the same geometrical parameters as those in Fig. 5 (i.e., $h/a = 5.0$, $r/a = 0.4$, and $d/a = 0.5$) are depicted as M1–M5 in Fig. 6(a). Modes M1, M2, and M5 represent overlapping degenerate modes with the same displacement profile. Figure 6(b) shows the displacement profiles of the first five distinct modes of a cylindrical pillar with identical geometrical parameters as those of the PnC in Fig. 6(a). These pillars are modeled with the fixed BC at one end and the free BC at the other end. The close similarity between the shear mode profiles (M1, M2, and M5), the breath mode profile (M3), and the longitudinal mode profile (M4) in the two structures [i.e., the PnC in Fig. 6(a) and an individual pillar in Fig. 6(b)] shows the effect of the resonance of individual pillars on determining the position of branches in the band structure of the PnC, which, consequently, determines the position of the PnBGs.

2.3 Effect of Lattice Symmetry

The effect of Bragg scattering on the formation of the PnBGs depends on the lattice periodicity, while the resonance of individual pillars depends only on the geometry of the pillars. In Sec. 2.2, this statement was examined by changing the geometry of the pillars. In this section, the role of the second factor (i.e., the lattice periodicity) in determining the interplay of Bragg scattering and local resonance is studied. To perturb this interplay, the positions of the pillars are randomly perturbed in a supercell (without changing their heights or radii), and the center frequency and width of

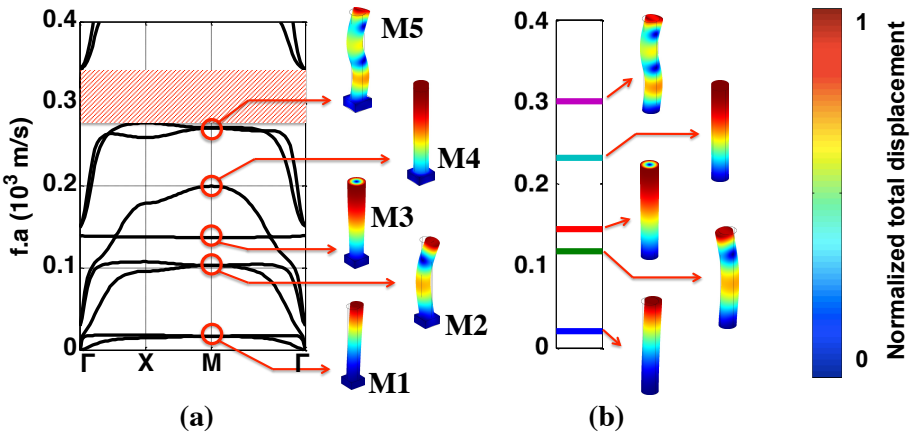

Figure 6: Comparison of the mode profiles of (a) a pillar-based PnC with W pillars arranged in a square lattice on a Si membrane with a thickness (d/a) of 0.5 at the high symmetry point M and (b) individual W pillars with the fixed BC at one end without Si membrane. The normalized radius (r/a) and height (h/a) of pillars in both cases are 0.4 and 5.0, respectively.

the PnBGs are calculated. The results of these simulations are compared for pillars with different heights. These perturbations are expected to have greater effect on the PnBGs formed through Bragg scattering — especially when the pillars are short compared to the lattice constant, and the local resonance effect is not the dominant factor in the PnBG formation. As the height of the pillars increases and the local resonance becomes dominant, the effect of lattice perturbation is expected to become less significant.

Figure 7(a) illustrates the perturbation scheme that is used in the calculations to demonstrate the effect of lattice perturbation on the formation of PnBGs in a square lattice. As shown, a 3×3 supercell is modeled with each pillar displaced following a Gaussian distribution in the x and y directions. Such a displacement scheme yields to a Rayleigh distribution for the relative distance (denoted by dis_{ij}) from the original position of each pillar and a uniform distribution for the angle of displacement (denoted by ϕ_{ij}). The thickness of the membrane and the radii of the pillars are fixed at $0.5a$ and $0.4a$, respectively, for the purpose of this study. The whole

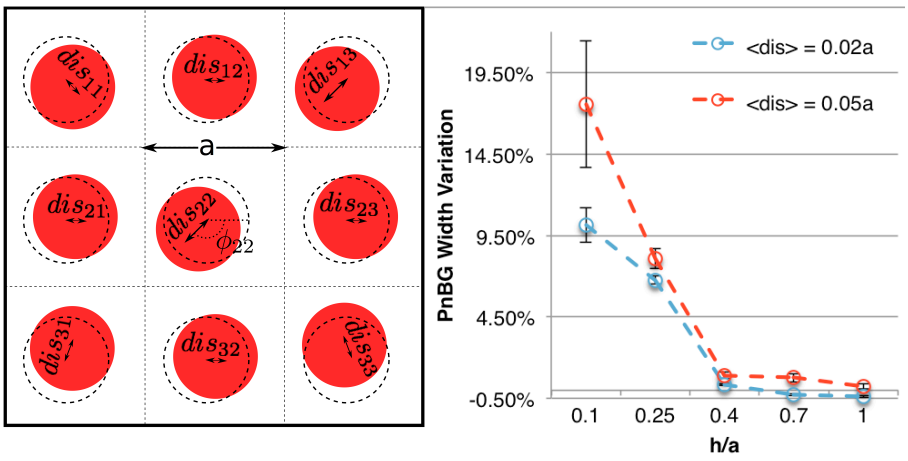

(a) **(b)**

Figure 7: Effect of lattice perturbation on the widths and positions of the PnBGs in a 3×3 supercell of W pillars on a Si membrane. The PnC is formed by periodically repeating this supercell in both x and y directions. (a) Pillar displacement scheme used for modeling the effect of lattice perturbation on PnBGs. dis_{ij} and ϕ_{ij} denote the displacement distance and angle of the center of the pillar number ij (from that in a perfectly periodic PnC). The unperturbed structure, as depicted by dashed circles, is a square lattice PnC with lattice constant a. (b) Variations of the PnBG width (compared to the unperturbed square lattice structure) are shown for different pillar heights and mean displacements. The PnBG in unperturbed lattice is used as the reference for calculating the relative changes shown in the figure. The error bars show the extent of the standard error (σ) obtained for the Monte Carlo simulation.

PnC is formed by periodically repeating this supercell in both x and y directions. It should be noted that the unperturbed structure gives a square lattice PnC with lattice constant a. These simulations are repeated 20 times for each chosen pillar height to model the effect of random pillar distribution for each structure, and the average center frequencies and widths of the PnBGs are calculated accordingly. The relative change in the average PnBG width compared to that of the unperturbed structure is shown in Fig. 7(b) for two different values of the mean displacement.

As shown in Fig. 7(b), for a supercell with $h/a = 0.1$, the lattice perturbation with a mean displacement ($\langle dis \rangle$) of $0.05a$ causes an average change of 17% in the width of the PnBG. It is important to note that this is the same first PnBG (B1) — as discussed in Section 2.2 and illustrated in Fig. 3(a) — that has a high dependency

on the Bragg effect. For taller pillars, as B1 closes for the square lattice PnC, this perturbation causes a much smaller change (below 1%) in the width of the PnBG and becomes negligible as the height of pillars increases beyond $h/a = 0.4$. In comparison, for a perturbation scheme with smaller mean displacement (i.e., $\langle dis \rangle = 0.02a$), the average change in the PnBG width is smaller, but the curve follows the same trend as the pillar height increases. These results also show that for the range of h/a values in this study (i.e., $h/a = 0.1 - 1.0$), the center frequency of the PnBG remains within 1% of that of the unperturbed structure. The results shown in Fig. 7 suggest that there is a strong correlation between the height of pillars and the resilience of the corresponding PnBG against lattice perturbations.

The calculations in this section, therefore, show that the lattice symmetry is less of a determining factor in opening the PnBGs in pillar-based PnCs with taller pillars ($h/a > 0.4$), and the pillar geometry is the dominant geometrical feature of these structures. This is in line with the previous arguments that for PnCs with taller pillars the effect of local resonance is the dominant factor in opening the PnBGs.

2.4 Experimental Evidence of High-Frequency PnBG

The PnC structure discussed in this section is formed by a triangular lattice of gold (Au) pillars on a free-standing membrane that consists of three thin layers of aluminum nitride (AlN), molybdenum (Mo), and Si, from top to bottom. Figures 8(a) and 8(b) show the scanning electron microscope (SEM) images of the PnC structure and the arrangement of the three layers in the membrane, respectively. To characterize the first PnBG of this structure, the transmission of acoustic waves at different frequencies through the structure is monitored by placing a pair of identical sinc-cosine weighted IDTs [8] with thin (80 nm) aluminum (Al) electrodes on the two sides of the PnC, as shown in Fig. 8(c). The piezoelectric nature of the AlN film provides the necessary transduction of the electrical and elastic energy. The middle Mo layer

in the membrane acts as the ground layer for piezoelectric transduction. The geometrical parameters for the chosen structure are $a = 3\,\mu$m, $r = 1\,\mu$m, $h = 240\,$nm, $d_{\mathrm{AlN}} = 1\,\mu$m, $d_{\mathrm{Mo}} = 100\,$nm, and $d_{\mathrm{Si}} = 340\,$nm, where a, r, h denote the lattice constant; pillar radius; and pillar height; and d_{AlN}, d_{Mo}, and d_{Si} denote the AlN, Mo, and Si thicknesses, respectively.

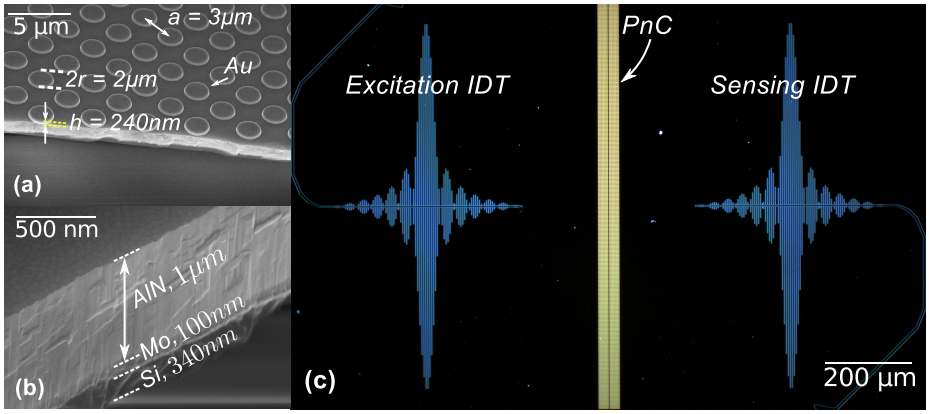

Figure 8: Fabricated pillar-based PnC membrane with excitation and sensing IDT electrodes on the sides. (a) SEM image of the PnC membrane with Au pillars deposited on the AlN/Mo/Si membrane. (b) SEM image of the cross-section of the AlN/Mo/Si membrane. (c) Dark-field histogram-balanced micrograph of the device showing the IDT structure.

The FEM simulations show that this structure supports a complete PnBG in the frequency range of 760 MHz–820 MHz. Figure 9 shows the band structure of the PnC along the boundary of the irreducible Brillouin zone and directional band diagrams along the three major crystallographic directions (i.e., Γ–Y, Γ–L, and Γ–K) of the triangular lattice formed by the arrangement of the pillars on the membrane. The unit cell of the triangular lattice used in the FEM simulations is depicted in Fig. 9. It is important to note that the Γ–Y and Γ–K directions are aligned with the 100 and 010 crystallographic directions of the Si film used in the membrane.

The sinc-cosine weighting of the IDTs is designed to achieve a wide frequency response required for sweeping a frequency range wider than the PnBG of the structure. The IDTs in the structure are designed to excite the antisymmetric (AS) modes of

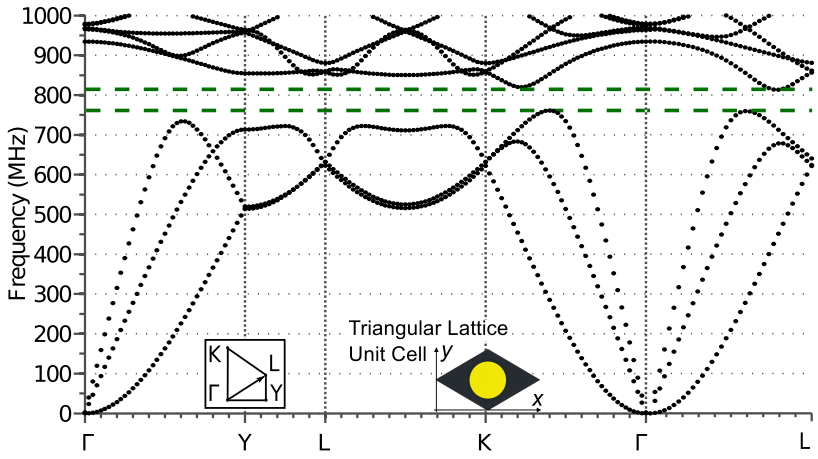

Figure 9: Band structure of the triangular pillar-based PnC membrane of Fig. 8 along the edges of the irreducible Brillouin zone of the triangular lattice and along the Γ–L direction, as shown in the inset. The unit cell of the triangular lattice is shown for reference. The extent of the PnBG is shown by the dashed lines.

the structure; however, the symmetric (S) modes are also expected to be excited due to the strong coupling of the S and AS modes in the 3-layer stacked membrane. In contrast to the S and AS modes, the shear-horizontal (SH) modes of the structure are not expected to be excited.

An optimal fabrication process for these PnC structures was developed in this research. The fabrication of this structure starts from a silicon-on-insulator (SOI) wafer with Mo and AlN layers deposited on the wafer. The deposition process of Mo and AlN was performed in Tegal Corporation. The AlN layer is patterned with the conventional photolithography and wet etching techniques to form the ground pad openings. In the next step, a layer of electron-beam resist (PMMA, by MicroChem) is deposited on the structure, and the PnC pattern is formed by electron-beam lithography. The Au pillars are then formed by electron-beam evaporation followed by a lift-off step. The Al electrodes for the IDT pairs are patterned using a similar process. The final step of the fabrication is releasing the PnC membrane by selectively etching the backside Si wafer using backside alignment, photolithography, and dry etching of Si using the Bosch process followed by wet etching of the buried oxide layer using the

buffered oxide etch (BOE) solution. Figure 10 illustrates these fabrication steps. All the fabrication processes were developed and optimized at the facilities operated by the Georgia Tech Institute for Electronics and Nanotechnology (IEN).

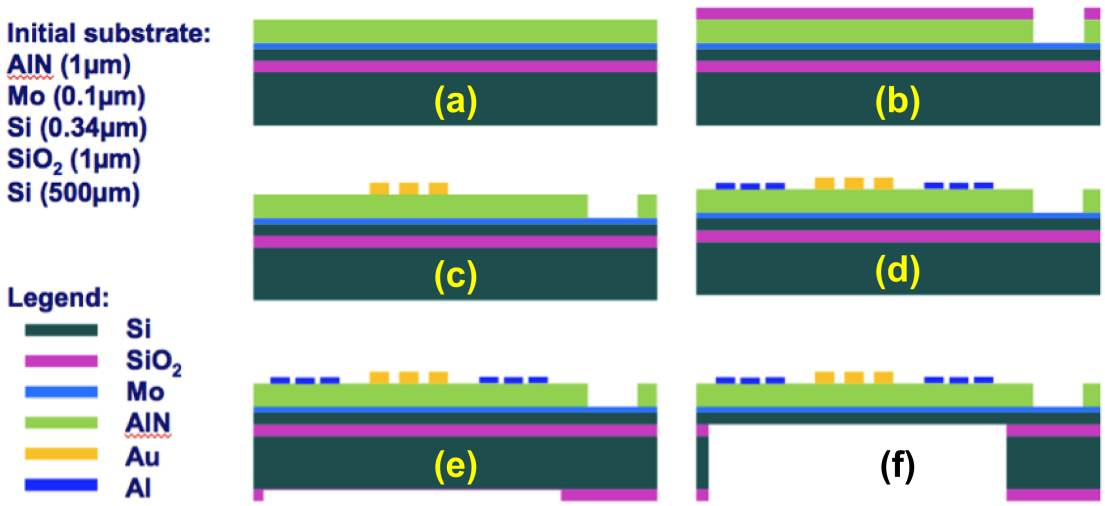

Figure 10: Fabrication steps for implementing a metallic pillar-based PnC structure with IDTs on the sides for excitation and sensing. (a) Initial layers of the substrate consisting of AlN, Mo, Si, SiO_2, and Si. The thicknesses of these layers are listed in the graph. (b) Etching AlN for electrical connection with the bottom Mo layer. (c) Depositing and patterning metallic pillars using electron-beam lithography and lift-off process. (d) Depositing and patterning IDT electrodes using the same process as that of the metallic pillars. (e) Backside alignment and hard mask patterning of the substrate using photolithography. (d) Backside etching of the substrate using Bosch process and removal of the SiO_2 layer underneath the structure.

To characterize the PnBGs in different crystallographic directions, multiple PnCs are fabricated with similarly patterned IDTs rotated and aligned with major crystallographic directions, namely Γ–Y, Γ–L, and Γ–K. To have a reference point for the baseline transmission between each IDT pair, for every device with a PnC between two IDTs, a reference IDT pair is fabricated without the PnCs between them. Characterization of these devices is performed using an HP 8753D network analyzer and measuring the S_{21} parameter of the structure. To compensate for the frequency response of the IDTs, the response of the PnC structure is normalized to that of the

corresponding reference device.

The results of the measurements are shown in Figs. 11(a)–11(c). It can be seen that for all three characterized directions, the observed normalized transmission falls below −20 dB for frequencies within the theoretically calculated directional PnBGs. The observed attenuations for Γ–Y and Γ–K directions are even stronger at −25 dB transmission throughout the expected PnBG regions. This level of attenuation validates the theoretical simulations that the chosen pillar-based PnC membrane supports a PnBG around 800 MHz in all three major crystallographic directions. Note that the attenuation in each direction also depends on the length of the structure in that direction. In these experiments, the length of the structure in the Γ–Y, Γ–L, Γ-K directions are 9, 16, and 16 periods, respectively, resulting in estimated attenuations of 2.7 dB/period, 1.25 dB/period, and 1.6 dB/period, respectively for the three directions. To the best of my knowledge, this is the first experimental demonstration of an ultra high-frequency PnBG in a pillar-based PnC membrane.

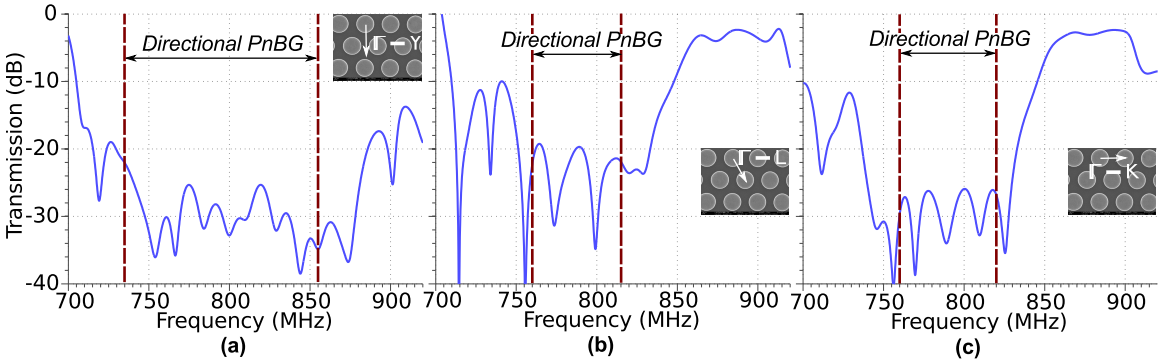

Figure 11: Normalized transmission (S_{21} parameter) of the fabricated triangular pillar-based PnC lattice in the (a) Γ–Y, (b) Γ–L, and (c) Γ–K directions. The arrow in the inset in each part represents the direction along which the experimental measurement is conducted. The dashed lines illustrate the theoretical boundary of the directional PnBGs for each direction.

2.4.1 PnBG Widening

It can be seen from the measured transmission spectrum in Fig. 11 that in addition to the large attenuation at the PnBG frequencies, the transmission at frequencies outside the PnBG window are also suppressed, resulting in a wider experimentally observed bandgap than the theoretical PnBG. This attenuation can be justified by studying the nature of different PnC modes at the edges of the PnBG and the excitation of each PnC mode through its coupling to the generated acoustic waves in the membrane by the IDTs. In general, the modes that the IDTs generate can excite only a subset of the supported Bloch modes in the studied PnC membrane. Specifically, it is expected that the majority of the transduced elastic energy will be carried by S and AS modes; it is not expected that the SH modes will be excited by the IDTs. This effect alone may cause the measured PnBG to appear wider than expected if the Bloch mode at the edge of the PnBG is of the SH type [12, 60, 78].

The second reason for observing a wider-than-expected region of high attenuation in the transmission measurements can be the mismatch (e.g., opposite symmetry) between the incident mode generated by the IDTs and that of the Bloch mode inside the PnC [14]. Certain Bloch modes in a PnC have antisymmetric displacement profiles along the in-plane axis normal to the direction of wave propagation [referred to as in-plane perpendicular axis (IPPA)]. This leads to very low elastic energy coupling of the plane waves generated by IDTs (which are symmetric along the IPPA) to such antisymmetric Bloch modes. The symmetric and antisymmetric Bloch modes along the IPPA will be denoted as IPPA-S and IPPA-AS to distinguish them from the Lamb S and AS modes. It is clear that if the PnC mode at the edge of the PnBG is an IPPA-AS mode, the observed high-attenuation region will be larger than expected due to poor excitation of this mode.

The third factor affecting the S_{21} measurements is the mismatch in the group velocity of the propagating modes inside and outside the PnC structure. Essentially,

this mismatch results in lower observed transmission even for matching AS modes with the symmetric profile along the IPPA as the group velocity of the PnC mode at the band edge is usually small.

To understand the role of these three mechanisms in expanding the high-attenuation region for the studied PnC structure, the PnC band structure in the Γ–K direction along with the type of the PnC modes (i.e., S, AS, SH) and their symmetry along the IPPA are shown in Fig. 12(a) and 12(b), respectively. For comparison, the measured transmission spectrum is shown in Fig. 12(c). The Bloch mode types in Fig. 12(a) are assigned by considering the dominant component of the displacement vector. The IPPA symmetric/antisymmetric modes in Fig. 12(b) are identified using the phase difference between the displacement phasor on the two sides of the unit cell. This approach will give a phase of π rad for IPPA-AS modes and a phase of 0 rad for IPPA-S modes. To illustrate this concept more clearly, two mode profiles (one for an IPPA-S mode and one for an IPPA-AS mode) are shown in Fig. 12(b).

Side-by-side comparison of Bloch modes in Figs. 12(a) and 12(b) reveals that the Bloch modes to the left of the lower edge of the PnBG (i.e., at lower frequencies than 760 MHz) are of S and AS types and are symmetric along the IPPA. However, the modes closer to the band edge exhibit a very low and close-to-zero group velocity. This near-zero group velocity and its mismatch with the group velocity of the incident mode results in low transmission to the left of the PnBG edge and extends the high-attenuation region to frequencies lower than 760 MHz [see Fig. 12(c)].

A similar comparison for the upper edge of the PnBG shows that in the 820 MHz–860 MHz range, the PnC supports only SH modes and, as mentioned previously, these modes are not excited by the IDTs. In addition, these modes have antisymmetric profile along the IPPA as seen in Fig. 12(b). Thus, to the right of the PnBG (i.e., higher frequencies), the transmission can only grow when the PnC supports S modes (with IPPA-S symmetry) beyond 860 MHz [see Figs. 12(a) and 12(b)]. This is in

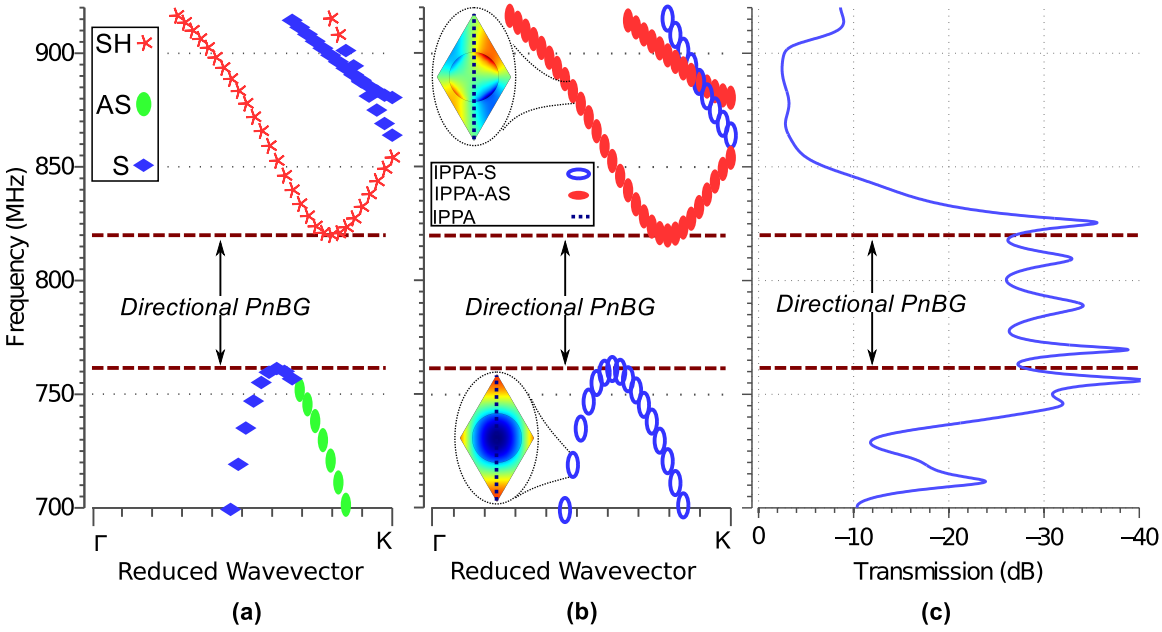

Figure 12: Comparison of the (a) types of Bloch modes in the band structure of the PnC in the Γ–K direction and (b) their symmetry/antisymmetry along the IPPA with (c) the measured normalized transmission of the fabricated PnC in the same crystallographic direction. The theoretically calculated PnBG is shown by dashed lines.

agreement with the experimental observation shown in Fig. 12(c).

To conclude this section, we have also performed a frequency domain simulation to numerically calculate the low-transmission regions of the structure for the Γ–K direction. The methodology of our simulation follows the same methodology by Khelif et al. [25]. The only difference here is that since our structure is not a SAW-based structure, we are using a sagittally polarized surface source (instead of a line source) in the cross-section of the structure to excite the Lamb waves. The schematic of the simulated structure and the estimated transfer function are shown in Fig. 13. It should be noted that the source is placed on the left side of the structure and the detector is placed on the right side of the structure in these simulations.

As seen in Fig. 13, the attenuation trend in this simulation agrees with the experimental result. The existence of the deaf band in the 820 MHz–860 MHz range can also

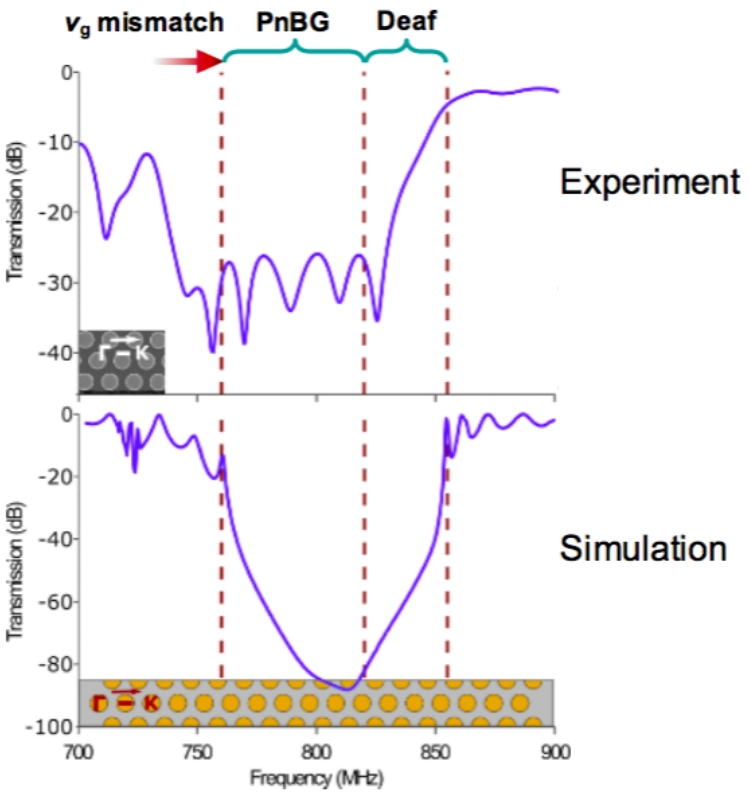

Figure 13: Comparison of the (a) experimental normalized transmission of the fabricated PnC in the Γ–K direction with (b) the simulated frequency response in the same crystallographic direction. The boundaries of the theoretically calculated PnBG and the deaf band are shown by dashed lines. The schematic of the simulated PnC membrane is shown in the inset.

be verified with reasonable agreement with the experimental result, as seen in Fig. 13. Additionally, lower transmission at the frequency range below 760 MHz, which is explained by the group velocity mismatch, can be seen in this numerical result. The difference in the maximum attenuation between the simulation and the measurement results can be attributed to the fabrication imperfections and low signal-to-noise ratio in the measurement data, as well as the material loss effect of the PnC structure in the frequencies out of the PnBG.

CHAPTER III

PNC-BASED GHZ WAVEGUIDES AND RESONATORS

Waveguides and resonators, along with the PnCs, are the building blocks of a signal processing platform that is based on the propagation of the elastic vibrations. These building blocks facilitate the design and implementation of more sophisticated modules including frequency multiplexers/demultiplexers, delay lines, filters, etc. Consequently, theoretical study and experimental demonstration of these devices are of high priority for any PnC platform.

In previous chapters, we have studied the physics of bandgap formation in the pillar-based PnC membranes. We have also experimentally demonstrated the existence of the complete PnBG around 800 MHz in one such structure. In this chapter, we will build upon our understanding of these basic elements to design fundamental PnC-based devices such as waveguides and resonators. We will improve the design of our PnC unit cell to realize a PnBG beyond 1 GHz. We will then modify the structure of the PnC to enable acoustic waveguiding inside a PnC structure. Experimental evidence will be provided that supports the existence of waveguiding in the proposed structure. We conclude our discussion on the PnC-based waveguides and resonators in this chapter with introducing a design approach for lateral-mode and waveguide-based PnC resonators.

3.1 PnBG Optimization for GHz Waveguiding

The starting point for the design of a PnC-based waveguide is choosing an optimal PnC structure that supports a PnBG at the desired frequency range. As our goal here is to demonstrate a waveguide operating at the GHz range, we have to alter our previous design based on the Au pillars, which possesses a PnBG at around

800 MHz. From our study on the physics of the bandgap formation, we understand that using shorter Au pillars or pillars with reduced diameter leads to bandgaps at higher frequencies, but at the same time, results in a narrower bandgap (and eventually closing of the bandgap). Recalling that our previous design parameters were chosen to achieve an optimal trade-off between bandgap frequency versus gap-to-mid gap ratio, the only remaining geometrical parameter is the lattice constant.

To explain the above concern, let's assume we could reduce the lattice constant from 3 μm to 2.5 μm. If we were able to scale down all the dimensions of our unit cell proportional to the scale factor of the lattice constant, including the thickness of all the layers of the membrane, the center frequency of the PnBG would scale to 960 MHz. Aside from the fact that this is not yet a truly GHz PnBG, there is another problem in our assumptions. As a matter of practical significance, in geometrical scale-down scenarios, the thickness of the membrane layers may not always be an option. One single chip might house multiple PnC structures with different center frequencies, all of which have to share a common membrane. Therefore, we prefer to keep the current membrane structure and push the boundaries of what is possible by only optimizing the pillars—both their dimensions and material—along with a conservative change to the lattice constant without altering the membrane structure.

To design a PnC with the aforementioned properties and geometrical constraints, we will be using Nickel (Ni) instead of Au as the metal of choice for the pillars. Ni is both lighter and stiffer (i.e., it has lower density and higher Young's modulus) compared to Au, pushing the center frequency of the PnBGs higher. Using Ni as the material of choice for the pillars, we conduct an exhaustive search over the height and radius of the pillar in the unit cell as well as allowing modest changes to the lattice constant. This search resulted in an optimum PnC design shown in Fig. 14. As seen in this figure, the PnC of choice has a triangular lattice structure with Ni pillars on a three-layer membrane of AlN, Mo, and Si. The radius and height of all

pillars are 750 nm and 400 nm, respectively, and the lattice constant is a =2.5 μm. The thickness profile of the composite membrane is the same as the one presented in Sec. 2.4 [see Fig. 8(b)].

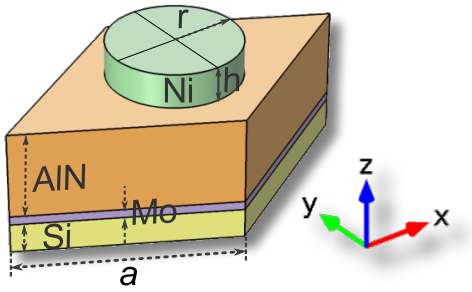

Figure 14: Unit cell of a pillar-based PnC with triangular lattice type composed of Ni pillars on a three layer membrane of AlN, Mo, and Si.

The dispersion diagram of the designed PnC is shown in Fig. 15, depicting the boundaries of a PnBG in the 1030 MHz–1155 MHz frequency range (i.e., gap-to-midgap ratio of 11.4%) along with a second narrower PnBG around 1450 MHz. It should be noted that based on our understanding of the physics of PnBG formation in pillar-based PnCs (Chapter 2), neither of these PnBGs are the result of local resonance effect. This conclusion is based on the fact that the height of pillars are still much smaller than the lattice constant (h/a = 0.16) and changing this height does not drastically affect the position of the PnBG. Additionally, these PnBGs are highly lattice-dependent, such that a square lattice does not support any of these PnBGs.

In our designs in this chapter, we will focus on utilizing the first PnBG of the proposed Ni-based PnC to form waveguides and resonators. The desired device is derived from the original PnC following various structural variations (as discussed in the next section), which introduce guided or resonant modes to the structure.

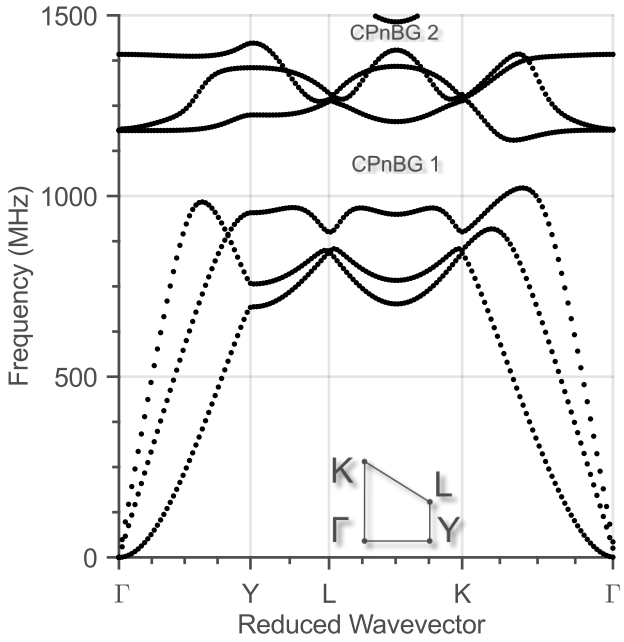

Figure 15: Band structure of the triangular pillar-based PnC membrane of Fig. 14 along the edges of the irreducible Brillouin zone of the triangular lattice, as shown in the inset. The extents of the complete PnBGs (CPnBGs) are shown by the dashed lines. The radius and height of the Ni pillars are 750 nm and 400 nm, respectively. The thicknesses of AlN, Mo, and Si layers are 1 μm, 100 nm, and 340 nm, respectively. The lattice constant is 2.5 μm.

3.2 Structure and Dispersion Diagram of PnC-based Waveguides

To construct a waveguide/resonator from the designed PnC, one may remove one column of pillars from the PnC lattice. A simple schematic of a PnC-based waveguide and its defect region is shown in Fig. 16. This type of defect in the PnC lattice usually leads to resonant modes confined inside the region without pillars, known as the *defect region*. To effectively simulate this structure, we have to define a waveguide unit cell and apply appropriate boundary conditions to reflect the periodicity and propagating nature of the elastic waves inside the defect region. Figure 17 illustrates one row of this structure, acting as the unit cell of the waveguide. The structure is periodic in the vertical direction and is ideally infinite in the lateral direction. However, to make the theoretical study and simulation of this waveguide feasible, a fixed BC is applied to a

laterally truncated structure, and a Floquet BC, to the top and bottom sides of the unit cell [see Fig. 17]. If the number of lattice periods on the two sides of the structure is large enough, the resonant modes of the laterally fixed structure will be decoupled from its fixed boundaries. Hence, an isolated waveguide/resonator can be accurately modeled. The Floquet BC, however, serves a more general purpose. A zero phase for the Floquet BC is equivalent to the periodic BC, which models a resonator, while, a nonzero phase models a PnC waveguide with guided modes propagating inside the defect region in the y direction, as shown in Fig. 17.

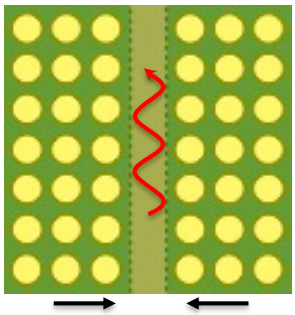

Figure 16: Schematic of a pillar-based PnC waveguide constructed by removing a row of pillars, effectively creating a line defect, and altering the distance between the two separate parts on the both sides of the structure. The curly arrow illustrates the elastic wave propagating in the defect region, i.e., the waveguide.

To calculate the dispersion diagram of this structure (for waves propagating in the y direction), we sweep the Floquet BC phase from 0 rad (i.e., high-symmetry point Γ) to π rad (high-symmetry point X), and the eigenmodes of the structure is computed using the FEM method. To accurately tune the frequency of these confined modes, the separation distance of the two sides of the structure [see Fig. 17] can be changed and the resulting dispersion diagram examined. The simulated dispersion diagrams for three separation distances of 0.7, 0.8, and 0.9 times the original distance of $a\sqrt{3}$ are shown in Figs. 18(a), 18(b), and 18(c), respectively.

For the lateral resonance, the eigenmodes at the high-symmetry point Γ are of interest. As an example, the structure with the separation factor of 0.8 has three

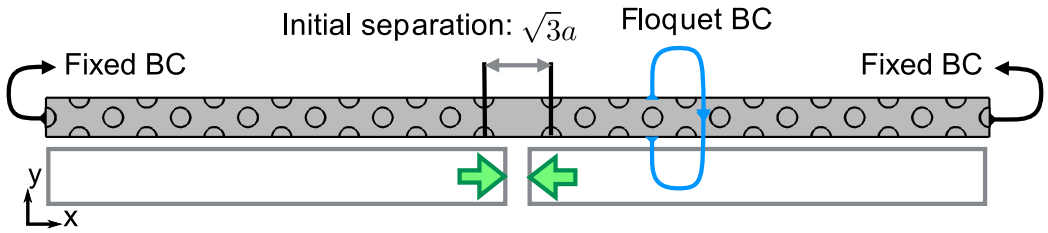

Figure 17: Unit cell of a waveguide based on pillar-based PnC composed of pillars arranged in a triangular lattice. The boundary conditions (BCs) and the separation distance between the two PnC parts are illustrated in the figure.

eigenmodes inside the PnBG (the edges of which are denoted by dashed lines in Fig. 18) at the high-symmetry point Γ point. The mode profile of these modes are shown in Fig. 19. As seen from Fig. 18(b), the resonant modes at 1082 MHz and 1090 MHz (isolated by the small oval region) are in the middle of the PnBG, providing a more reliable design. Moreover, the displacement profile of these modes have strong shear vertical (SV) component, making them suitable candidates to excitation by IDT-like electrodes on the AlN piezoelectric layer. The lower-frequency mode in the diagram is a shear horizontal (SH) mode, and, therefore, is not expected to be efficiently excited using the piezoelectric effect of the AlN layer.

To study the guided modes (propagating in the y direction), we have to consider the eigenmodes inside the PnBG with non-zero k values. We can see in Fig. 18 that all the three candidate structures have guided modes with interesting properties such as negative group velocity as well as close-to-zero group velocity. We will explain in the next section that the observable branches in the dispersion diagram associated with the waveguide modes are not of single polarization type. In fact the polarization, as well as the in-plane symmetry, of these modes gradually change as we sweep the k value from Γ to X.

Based on the considerations discussed so far, we have concluded that the structure corresponding to Fig. 18(b), with the separation distance factor of 0.8, is the optimal structure to experimentally demonstrate the waveguiding effect in a PnC-based

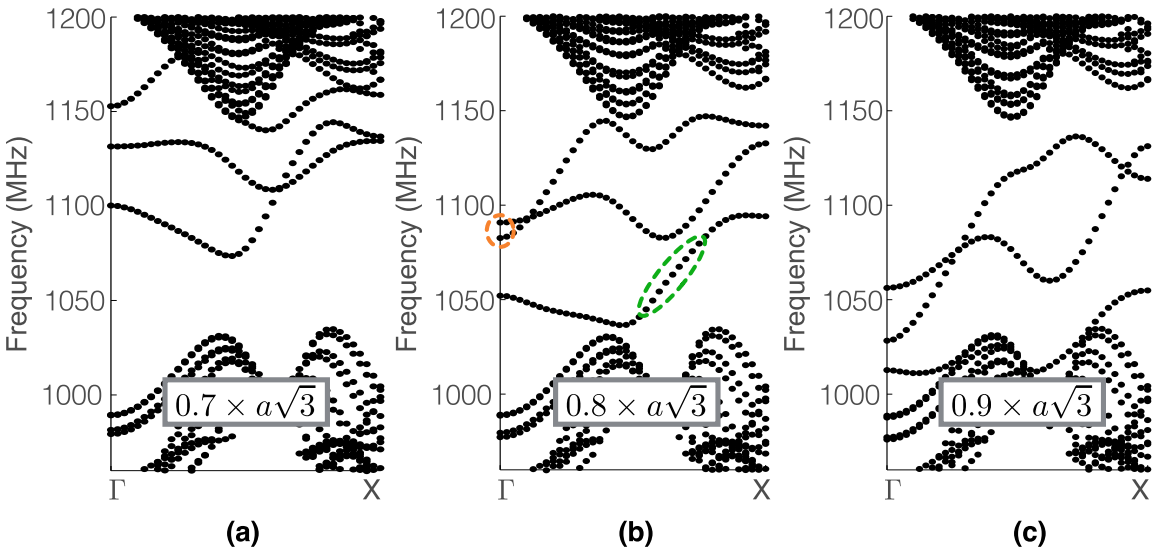

Figure 18: Dispersion diagram of the waveguide in Fig. 17 for the separation distances of (a) 0.7, (b) 0.8, and (c) 0.9 times the initial separation distance [$a\sqrt{3}$ in Fig. 17] of the two sides of the structure. Dashed horizontal lines show the boundaries of the PnBG in the original PnC. The structure and the geometric dimensions of the underlying PnC are the same as those in Fig. 15.

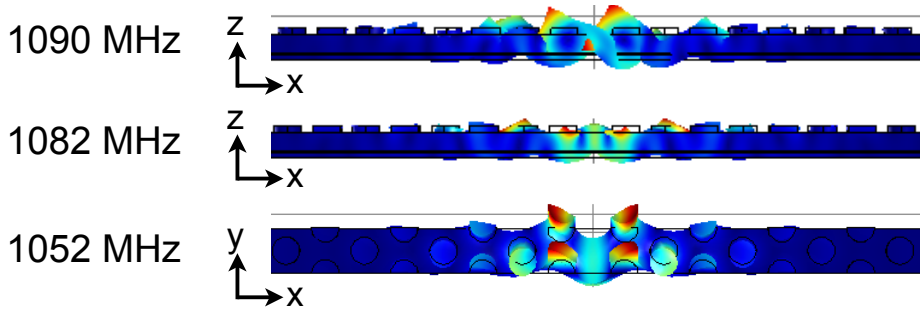

Figure 19: Displacement profiles of the stationary modes (i.e., eigenmodes at Γ point between the boundaries of the PnBG) of the membrane-based PnC waveguide, the dispersion diagram of which is shown in Fig. 18(b), where the separation factor is $0.8 \times a\sqrt{3}$.

structure. Specifically, the waveguide modes surrounded by the slanted oval have the desirable polarization of AS type while being in-plane symmetric. The displacement profile of one such eigenmode, associated with a phase difference of 0.6756π rad in the Γ–X axis, is shown in Fig. 20. The out-of-plane displacement of this mode and its lateral in-plane symmetry make this mode an ideal candidate for the study of waveguiding in this structure. The other modes (other than those inside the slanted oval region) are either of SH type or in-plane antisymmetric. Another unique property of this set of eigenmodes is that, in reasonable range of frequencies (specifically from 1060 MHz to 1090 MHz), these are the only waveguide modes supported by the structure. This property leads to a single-mode waveguide that is more desirable compared to multi-mode waveguides of the other structures in Figs. 18(a) and 18(c). In the next section, we will discuss how we can experimentally demonstrate waveguiding for the optimal structure with the separation factor of 0.8.

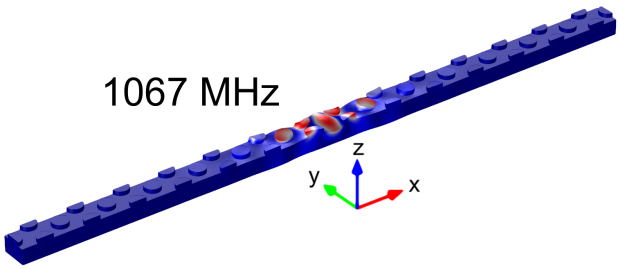

Figure 20: Displacement profile of the guided mode, with AS polarization, of the membrane PnC waveguide, the dispersion diagram of which is shown in Fig. 18(b), where the separation factor is $0.8 \times a\sqrt{3}$. The phase difference associated with Floquet boundary condition is 0.6756π rad in the Γ–X axis of the dispersion diagram.

3.3 Experimental Demonstration of Waveguiding

To experimentally demonstrate the waveguiding effect, we design a device to characterize this property. Our design consists of 9 layers of the waveguide unit cell (as shown in Fig. 17) surrounded by the excitation and sensing IDTs. The structure of this device is depicted in Fig. 21(a). As seen in this figure, the design of IDTs are

different from our previous designs. The reason for this new design is that we would like the generated acoustic energy to be concentrated on the opening aperture of the waveguide to increase the elastic energy coupling from the excitation IDT to the guided modes of the waveguide. Conversely, as the confined guided modes exit the other end of the waveguide, they would not propagate as a plane wave with a linear wave front but rather as a circular wave with a curved wave front. To be able to maximize the collection of energy from this wave front, the sensing IDTs would also need to conform to a curved pattern. The dashed lines in Fig. 21 overlayed on the excitation IDT show the approximate outline of the elastic waves generated by this IDT being focused at its focal point, where the opening aperture of the waveguide resides. The reverse of this applies to the waves diffracted from the other end of the waveguide, where their approximate outline is also illustrated by the dashed lines overlayed on the sensing IDT. Later we will discuss the simulation methodology used to design such focusing IDTs.

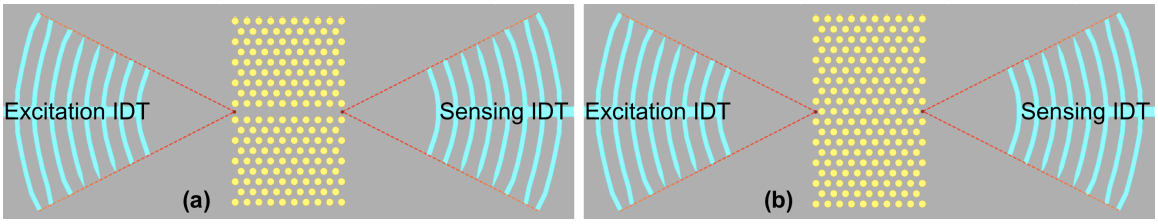

Figure 21: Arrangement of the focusing IDTs with (a) the waveguide or (b) the PnC in between in the fabricated devices. The intersection of the dashed lines show the designed focal point of the focusing IDTs.

We compare the measured S_{21} parameter of the device in Fig. 21(a) with that of a reference device, as shown in Fig. 21(b). The reference device in our experiment is similar to the waveguide with one exception: we replace the waveguide structure with the same number of layers of the corresponding PnC structure. We expect that the waveguide show higher transmission around the frequency of the waveguide mode and demonstrate similar transmission values to that of the simple PnC at frequencies

farther from the guiding region. As discussed earlier, the guiding modes of interest are the eigenmodes surrounded by the slanted oval in Fig. 18(b).

In addition to the above measurements, we have also fabricated two pairs of focusing IDTs. The first pair is the same as those shown in Fig. 21 with the waveguide removed from the middle, while the second pair is similar to arrangement of the first pair with their distance changed such that their focal points coincide. We will refer to the former as the "far IDTs" and the later as the "near IDTs," as shown in Figs. 22(a) and 22(b). Comparing the measured transmission (S_{21}) of these two sets of IDTs helps us understand the effectiveness of the focusing phenomenon augmented by the design of the IDTs. The expectation here is that when the focal points are coinciding (near IDTs) we should observe a much larger S_{21} compared to when the focal points are further apart (far IDTs). Additionally, we expect that putting a waveguide between the far IDTs (as shown in Fig. 21) will result in improved S_{21} measurement as the waveguide starts from one focal point and ends at the other.

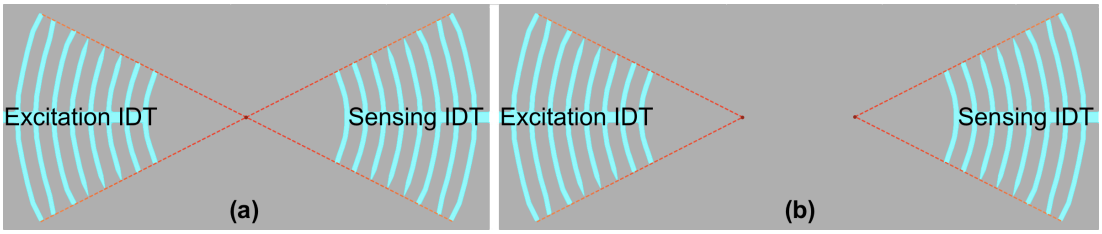

Figure 22: Arrangement of (a) the near and (b) the far focusing IDTs in the fabricated devices. The intersection of the dashed lines show the designed focal point of the focusing IDTs.

3.3.1 Design of Focusing IDTs

As discussed in the beginning of this section, to maximize the elastic energy coupled from the input IDT to the waveguide and to maximize the diffracted elastic energy from the outgoing end of the waveguide to the output IDT, in our experiments we have resorted to a specific type of IDT designs—known as focusing IDTs.

Several methods can be envisioned for designing a focusing IDT, including, but not limited to, calculating the phase velocity of the desired elastic wave polarization at the desired operating frequency and calculating the corresponding phase front (equi-phase) contours for a point source (emanating elastic waves from the focal point of the focusing IDT). By matching the location of IDT fingers to these equi-phase contours, we can design a focusing IDT for certain polarization at the desired operating frequency. However, this approach has certain limitations. First, the assumption of a pure polarization emanating from the focal point of the IDT may not always hold true. It is certainly not true for our waveguide modes as these guided modes are (in most cases) a mixture of different polarizations. Second, this design process uses the approximations used in ray tracing models. These approximations may accurately predict the behavior of the waves propagating from a point source in the far field, but they neglect the near field effects of the point source. Therefore, it limits our ability to design a focusing IDT close to its focal point, thereby, making our device more compact.

To address the aforementioned limitations, we have developed a design method for focusing IDTs that heavily relies on calculating the equi-phase contours of the elastic wave generated by a truncated waveguide—instead of a single-polarization point source—using FEM simulation. In addition to enabling near-field displacement profile calculation, this approach helps us to account for the mixed polarization nature of the waveguide mode as it enters the half-space (defined by the membrane layers) where the waveguide is truncated.

Using the above FEM-based equi-phase contour calculation requires us to choose a certain waveguide mode. Based on our previous discussion in Sec. 3.2, the structure with 0.8 separation factor has a desirable eigenmode at 1067 MHz (corresponding to a phase difference of 0.6756π rad in the Γ–X axis) as shown in Fig. 20. This mode has strong out-of-plane polarization, is in-plane symmetric, and is in the middle of the

single-mode frequency range of the waveguide dispersion diagram. Assuming that the focusing IDT is to excite this specific eigenmode, we can simulate the wave pattern exiting the truncated waveguide and entering the half-space.

The wave front calculation involves two separate FEM simulations: one to calculate the approximate boundary condition of the half-space (which has to match the displacement profile of the guided mode exiting the waveguide), and another to simulate a frequency domain analysis by applying the end-of-waveguide boundary condition to the half-space. The half-space is modeled as a half-circular domain with the perfectly-matched layer (PML) at the outer radius.

The first step is simply the eigenmode analysis of the waveguide structure with the desired phase for Floquet boundary condition followed by exporting the displacement profile of the cross-section of the waveguide. This displacement profile is used in the second simulation as the displacement boundary condition for the half-space. Figure 23 shows how the displacement profile from eigenmode analysis of the waveguide unit cell is mapped onto the boundary of the half-space. It should be noted that the displacement values extracted from the eigenmode analysis of the waveguide unit cell should be treated as phasors. Therefore, the boundary condition for the displacement phasor is formulated as the following:

$$u(x, y = 0, z) = \Re\{u_0(x, z)\} + \mathrm{i}\Im\{u_0(x, z)\}, \tag{2}$$

$$v(x, y = 0, z) = \Re\{v_0(x, z)\} + \mathrm{i}\Im\{v_0(x, z)\}, \tag{3}$$

$$w(x, y = 0, z) = \Re\{w_0(x, z)\} + \mathrm{i}\Im\{w_0(x, z)\}, \tag{4}$$

where u,v, and w represent the displacement in the longitudinal, shear horizontal, and shear vertical directions, respectively. The plane $y = 0$ is the position of the interface between the end of the waveguide and the boundary of the half-space.

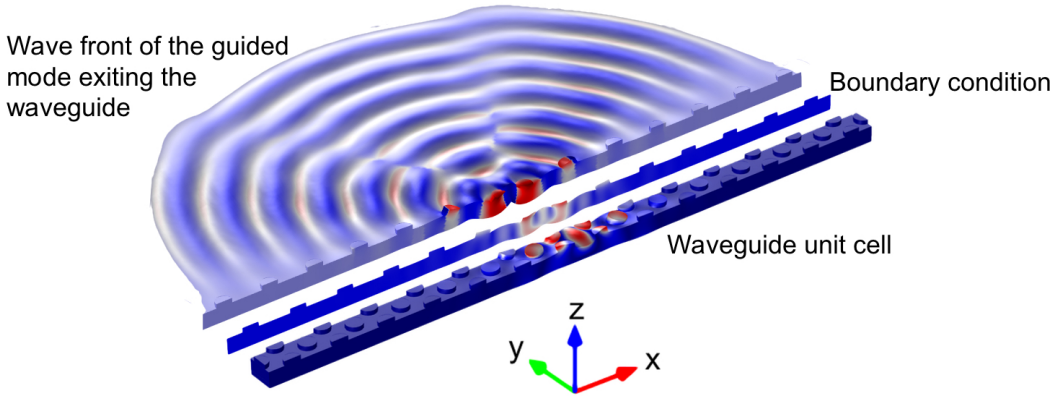

Figure 23: Displacement profile of the guided mode of the waveguide exiting the waveguide. The displacement profile of the eigenmode of the waveguide unit cell is extracted and applied to the boundary of the half-space as its driving boundary condition. The outer shell of the half-space (seen as the half-circular domain) is surrounded by PML.

After the boundary condition is applied, the second simulation, which is a frequency domain analysis, is performed. Note that the frequency setting for this simulation should be the same frequency as the eigenmode from which the boundary condition is extracted. This frequency domain analysis calculates the steady state response for the half-space when exposed to the waveguide mode. The peaks and valleys as well as a sample equi-phase contour of the diffracted wave in the half-space as calculated by the frequency response simulation is shown in Fig. 24.

Post-simulation processing of the displacement profile in Fig. 24 can reveal the exact location of the peak contours and their distance. The peak contours are used to design the position of the electrodes of the IDTs. Since we are using a ground layer at the bottom of the AlN layer (Mo layer in the middle of the membrane), we don't need the location of the valley contours. The distance of these contours is used to design the width of the electrodes of the IDTs. As seen in Fig. 24, the wave front in the half-space has a distinct diffraction pattern resulting in slight aberrations in the peak contours of the displacement profile. These aberrations help us visually identify three separate regions of the wave front, all extending approximately 60 ° azimuthally. These regions

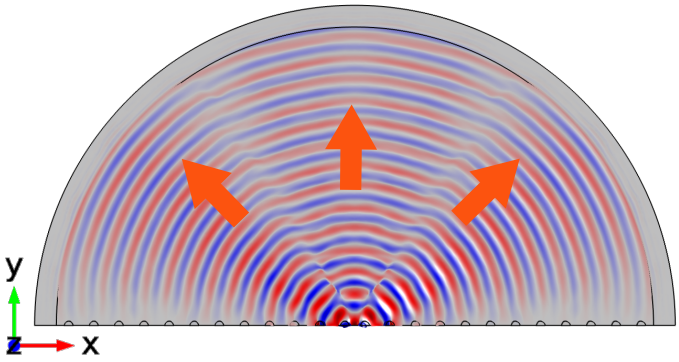

Figure 24: Wave front of the guided mode of the waveguide exiting the waveguide. The dashed curve shows an equi-phase surface of the wave front. The arrows show the direction of the wave propagation. The driving boundary condition is applied to bottom of the structure. The outer shell of the half-circle is surrounded by PML.

are highlighted in Fig. 24 by the three arrows overlayed on the displacement profile. To simplify the fabrication process and ensure the connectivity of the electrodes of the IDTs, we decided to use only the middle part of the wave front to design our focusing IDTs, leading to the patterns shown in Fig. 21.

3.3.2 Fabrication of the PnC-based Waveguides

Similar to the fabrication process of the pillar-based PnC structures to fabricate the waveguide device depicted in Fig. 21 and its corresponding reference device, we start with an SOI wafer with layers of Mo and AlN deposited on top by Tegal Corporation. Using photolithography and oxide hard mask, wide openings in the AlN is etched to enable the electrical contact, with the bottom Mo layer acting as the ground layer. The top electrodes are patterned following an EBL process with PMMA resist and the electron-beam evaporation of the Al layer, followed by the lift-off process.

Depositing and patterning the Ni pillars are more challenging, and we had to modify our process flow to accommodate for these challenges. Recall from Sec. 2.4 that the height of the Au pillars were 240 nm. Given a deposition rate of 2 Å in/sec the electron-beam evaporation step, 240 nm Au would be deposited in 20 minutes. Our

experiments show that this is a safe deposition period for the underlying PMMA so that it is not burned, and therefore, the lift-off process is performed with no problem. However, to deposit 400 nm of Ni with the same rate of 2 Å/sec, this process would take more than 30 minutes; given the higher melting point of Ni (1455 °C) compared to that of Au (1064 °C), this would result in damaging the underlying PMMA layer and therefore, destroying the outcome of the lift-off process. To solve this problem, we devised the following evaporation schedule: set the deposition rate to 3 Å/sec and run the deposition process in two steps, each depositing 200 nm of Ni while leaving the sample in the evaporation chamber for at least 30 minutes to allow enough time to cool down. Using this deposition schedule, we were able to lift-off the deposited Ni from underlying PMMA resist without any problems resulting in accurate transfer of the pillars' pattern onto the sample.

Releasing the PnC membrane using the backside alignment photolithography, Bosch process, and etching the buried oxide layer is performed similar to the steps outlined in Sec. 2.4. These fabrication processes were developed and optimized at the cleanroom facilities provided by the IEN.

3.3.3 Characterization Results

We measure the S_{21} scattering parameter of the fabricated devices using an HP 8753D network analyzer. In all of our measurements, we use an averaging factor of at least 500. This large averaging factor helps us reduce the noise in our measurements, enabling us to examine very low signal levels (down to -120 dB).

Figure 25(a) shows the measured S_{21} parameter for the near and far IDTs (as defined in Sec. 3.3) in the 1000 MHz–1150 MHz frequency range. Recall that the operating frequency of the focusing IDTs are tuned to a specific eigenmode of the waveguide at 1067 MHz. As expected, the near IDT attains its maximum transmission in the 1040 MHz–1060 MHz frequency range, which is within 2.5% of the design

specifications. We also observe that when the focal points of the IDTs are not coinciding (i.e., far IDTs), the transmission drops by at least 7 dB in comparison to the transmission of near IDTs. As discussed previously, this is completely expected for focusing IDTs; when the focal points are not coinciding, most of the elastic energy from the input IDT concentrated in its focal point diverges passing the output IDT by its sides. This result is a strong indication that our designed focusing IDTs are functioning as expected.

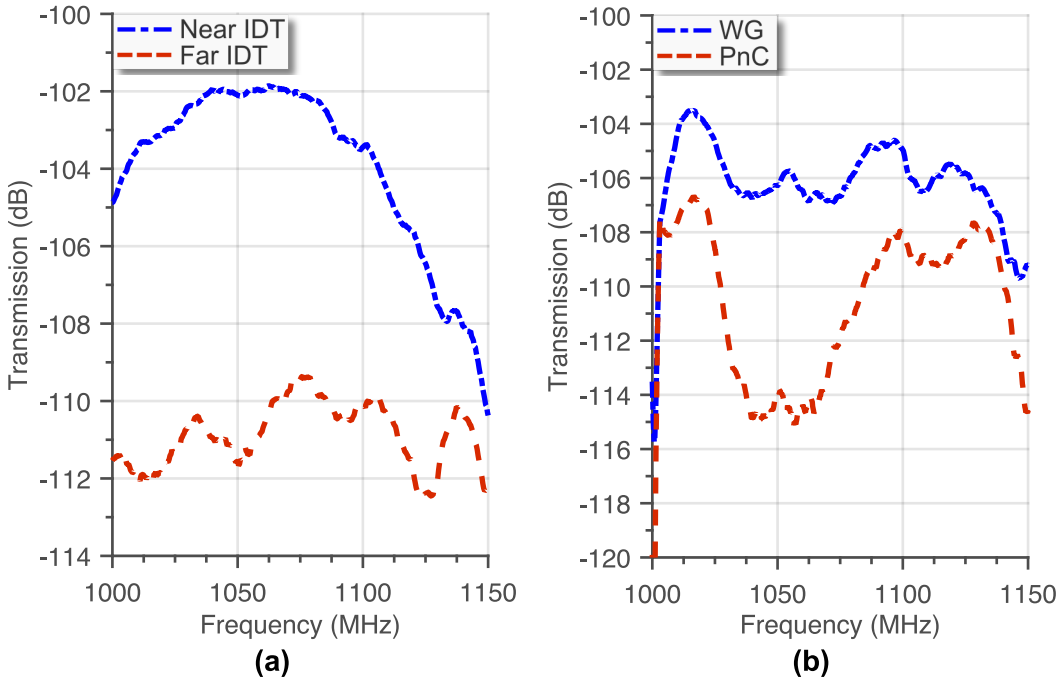

Figure 25: Measured transmission (S_{21} parameter) of (a) the near and far focusing IDTs, and (b) the far IDTs with waveguide and PnC in between. The arrangement of the fabricated devices are shown in Figs. 22 and 21. The PnC and waveguide designs are shown in Figs. 35 and 18(b).

Now that we have been able to verify the expected behavior of our focusing IDTs, we can study the effect of our designed waveguide (placed between the far IDTs) and compare it to the reference device (far IDTs with PnC in between). Figure 25(b) shows the measured S_{21} parameter for the far IDTs with waveguide in between (denoted as WG) and the reference device (denoted as PnC). We observe that WG

has larger S_{21} throughout the measured frequency range of 1000 MHz–1150 MHz compared to that of the PnC. Nevertheless, the largest difference occurs around the 1040 MHz–1060 MHz frequency range. It should be noted that since the single-frequency operation regime of this waveguide is from 1060 MHz to 1090 MHz, we expect to see the improving effect of the WG in a rather wide range of frequencies. We also expect that the elastic waves generated by the IDTs to have a non-negligible level of coupling to other modes of the waveguide, especially at the interface between the waveguide and the plain membrane, enhancing the measured S_{21} compared to that of the PnC.

To understand the effect of the polarization on the frequency response of the waveguide, Fig. 26 shows the polarization and (anti-)symmetry of the modes supported by the fabricated waveguide and compares the frequency of these modes with the frequency response of the WG normalized to the response of the PnC. We can see from this figure that the only waveguide modes inside the bandgap that have AS polarization and are in-plane symmetric are those in the single-frequency operation range of the waveguide. This range aligns, with reasonable accuracy, with the maximum normalized transmission of the waveguide. There are other in-plane symmetric modes with S polarization that also can contribute to the waveguides performance; however, we do not expect the SH modes or in-plane anti-symmetric modes to have an effect on the waveguide's performance.

To conclude this section, it is important to point out the hybrid nature of the eigenmodes supported by the fabricated waveguide. Figure 27 shows this hybrid nature by calculating the maximum normalized displacement of each eigenmode in three directions (u, v, and w) and mapping those normalized values to the red, green, and blue color code (RGB) of each point representing those eigenmodes. As seen in this figure, none of the eigenmodes have pure polarization and most importantly, the continuous branches of the dispersion diagram (as seen in Fig. 27) gradually change

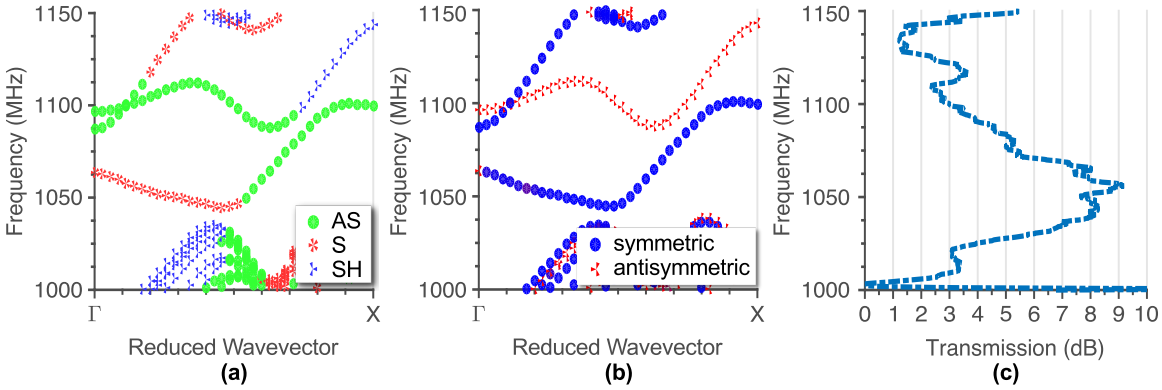

Figure 26: Comparison of (a) the types of the waveguide modes and (b) their symmetry/antisymmetry along the IPPA with (c) the measured normalized transmission of the fabricated waveguide.

in polarization as the wavevector is swept from Γ to X. These calculations verify our previous claim that strong cross-polarization coupling is possible from those generated by the focusing IDTs to those supported by the waveguide structure.

3.4 Design of PnC-based Resonators

In this section, we will discuss two types of PnC-based resonators: (1) lateral-mode and (2) waveguide-based resonators. We define a lateral-mode resonator as a PnC-based waveguide (see Fig. 16) operating at its stationary mode, i.e., high-symmetry point Γ in Fig. 18. A waveguide-based resonator is essentially a Fabry-Pérot resonator formed by a truncated PnC-based waveguide sandwiched between defect-less half-planes of multiple PnC layers, acting as the isolating mirrors. The resonant mode of this type of resonator is produced by the constructive interference of the waveguide mode reflected by the side PnC layers. We will discuss the optimum positioning of the electrodes inside lateral-mode and waveguide-based resonators to excite certain resonant modes and the theoretical verification of the validity of the proposed design.

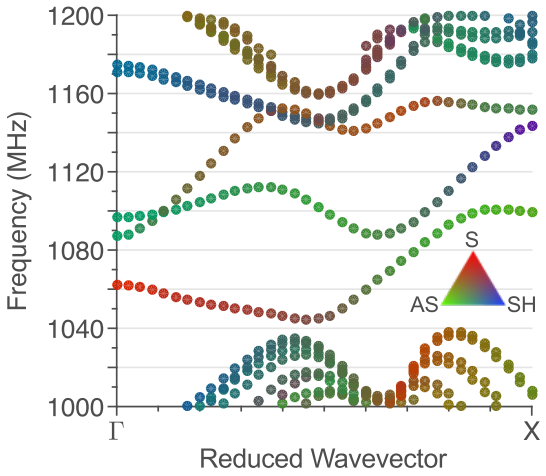

Figure 27: Hybrid polarization of the waveguide modes in Fig. 26(a). The inset shows the color spectrum used to visualize the hybridization of the S, AS, and SH modes.

3.4.1 Lateral-mode Resonator

Lateral-mode resonator is a PnC-based waveguide structure operating at the high-symmetry point Γ. As such, to identify all the lateral modes of a PnC-based wavgeuide, we only need to set the phase difference for Floquet boundary condition in Fig. 17 to 0 rad. This is equivalent to assigning a simple "periodic" boundary condition to the two sides of the unit cell of the waveguide. We will refer to the structure set up with periodic boundary condition as a lateral-mode resonator unit cell.

The geometry of a lateral-mode resonator is defined by the separation factor similar to the waveguide structure. To demonstrate our design and simulation steps, we will use the same waveguide design as in Sec. 3.2 with the separation factor of 0.8. The whole structure is on the same three-layer membrane of AlN (1 μm), Mo (100 nm), and Si (340 nm). Once the resonator unit cell with the correct geometric dimensions and boundary conditions is modeled, we can perform an eigenmode analysis to find its resonant modes. The lateral resonant modes and their polarization for the selected structure have been studied in our discussion of the dispersion diagram of the PnC-based waveguides in Sec. 3.2 (see Fig. 19). Our goal here is to design input and

output electrodes that can excite the eigenmodes at 1082 MHz and 1090 MHz. The eigenmode at 1052 MHz is a SH mode, and therefore, is not expected to be excited with the AlN piezoelectric layer.

Figure 28 shows the structure of a lateral-mode resonator with two Al electrodes added on the two sides of the cavity, acting as the excitation and sensing electrodes. This arrangement of electrodes enables us to directly excite the resonant modes inside the cavity. The thickness of the electrodes are chosen to be small (80 nm in this case) in order to prevent them from perturbing the resonant modes of the structure. The underlying Mo layer is connected to the ground port. Two PML domains are placed on both sides of the unit cell to simulate the infinite membrane beyond the truncated PnC lattice [see Fig. 28(b)].

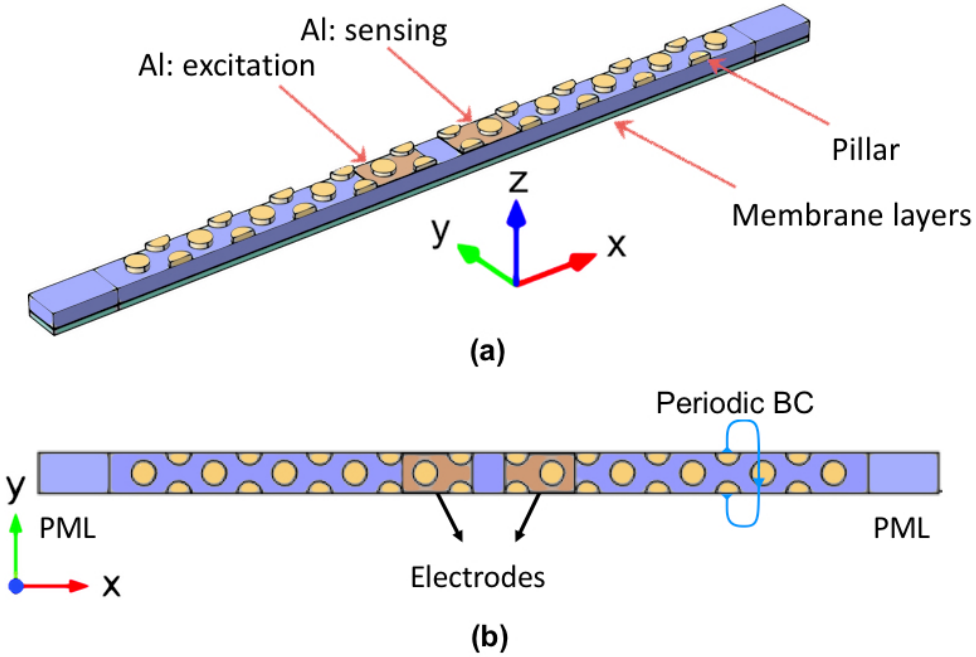

Figure 28: (a) Schematic of the unit cell of a lateral-mode resonator and (b) its top view. The pillars in the pillar-based PnC used in this structure are arranged in a triangular lattice.

In our model, the excitation and sensing electrodes are connected to 50 Ω impedance terminals. The excitation terminal is set to provide a constant power (P_{in}) into the

two-port network consisting of the excitation electrode, sensing electrode, and the common ground layer. The frequency response analysis calculates the power delivered to the output terminal via the sensing electrode, and the ratio between the input and output power determines the transmission parameter.

The frequency response of the structure illustrated in Fig. 28 is shown in Fig. 29. As expected, two resonance peaks can be observed for this structure at 1063 MHz and 1073 MHz. These resonance peaks are within 2% error margin of the theoretically calculated eigenfrequencies at 1082 MHz and 1090 MHz, respectively. This difference is due to the small perturbation of the resonator structure resulting from the addition of the Al electrode layer. Our investigation reveals that the lowest eigenmode of this resonator at 1052 MHz does not produce a resonance peak in the frequency response. This observation is also in line with our expectation as the polarization of this eigenmode is of SH type and can not effectively be excited by the AlN piezoelectric layer.

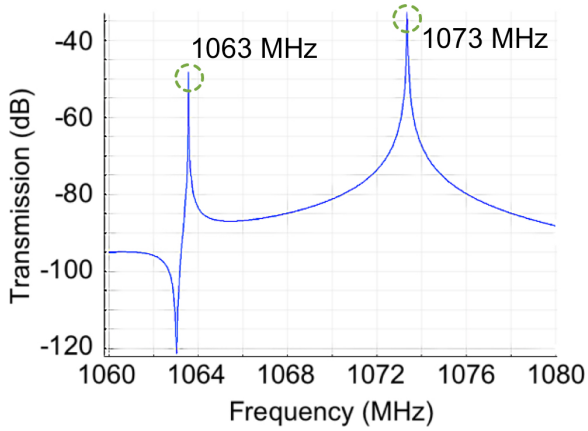

Figure 29: Frequency response of the directly excited lateral-mode resonator, the structure of which is illustrated in Fig. 28. Dashed circles show the two resonance peaks for this structure at 1063 MHz and 1073 MHz.

As seen in Fig. 29, the peak frequency for the observed resonant modes of the structure slightly differ from the result of the eigenmode analysis. However, we can alter the geometrical parameters of the directly excited structure in Fig. 28 to achieve

a limited frequency tunability. For this study, we change the location of the inner edge of the Al electrodes, i.e., the side of the electrodes facing the defect region. For example, shifting this edge by $0.5\times r$, where r is the radius of the pillars (750 nm in our designs) results in at least 7 MHz increase in the frequency of the resonance peaks. The frequency response of this modified structure is shown in Fig. 30. It should be noted that since the position of the outer edge of the electrodes is not changed, the effective result of our modification is having wider electrodes in the structure. This geometric modification scheme (i.e., altering the position of the electrodes boundaries) may prove helpful in fine-tuning the resonance frequency of the lateral-mode resonators.

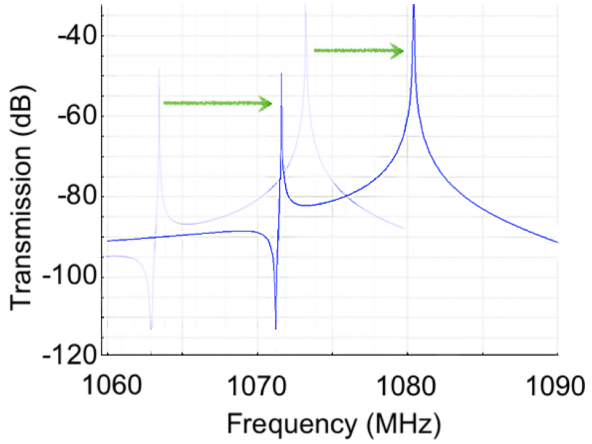

Figure 30: Comparison of the frequency response of the directly excited lateral-mode resonator, the structure of which is illustrated in Fig. 28. The light-colored curve is the same response as in Fig. 29. The dark-colored curve shows the frequency response when the inner edge of the Al electrodes are shifted by $0.5\times r$. The arrows show the correspondence between the original and modified structures' resonance peaks.

The frequency response diagrams shown in Figs. 29 and 30 provide an overview for the operation of a directly excited lateral-mode resonator. Nevertheless, we should be careful on how to interpret these results. Since one of the most important figures of merit in the functionality of resonators is quality factor (Q), it is tempting to extract the expected Q of the investigated resonator from the provided transmission diagrams

by fitting a Lorentzian function to the vicinity of each resonance peak. However, the calculated Q would account for only one source of loss, and that is the energy lost through the PML domains thanks to the non-ideal isolation of the elastic energy inside the resonator. In practice, there are other sources of loss that may dominate the overall Q of the structure. For example, we have not modeled the material loss in our calculations, and therefore, this important limiting factor on Q never shows its effect in the provided transmission diagram.

3.4.2 Waveguide-based Resonator

A waveguide-based resonator is composed of multiple periods of a waveguide unit cell enclosed by multiple PnC layers on both ends. Figure 31 depicts the top view of one such waveguide. The boundaries of the waveguide part is shown with dashed lines. The top and bottom part of this structure are truncated PnC structures (PnC caps).

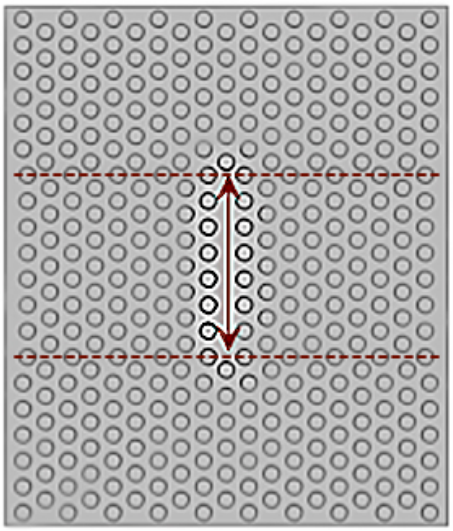

Figure 31: Schematic of a waveguide-based resonator constructed by truncating a PnC-based waveguide on both sides and enclosing it by multiple layers of the PnC. The dashed lines illustrate the edges of the truncated waveguide. The arrow shows the waveguide region and its extent.

In addition to being dependent on the choice of the separation factor of the waveguide, the resonance frequency of the waveguide-based resonator can change with the

length of the waveguide part. The number of resonant modes of the resonator is also a function of the waveguide's length. We investigate a waveguide-based resonator with 8 layers of waveguide unit cell (as shown in Fig. 31) with the separation factor of 0.8. The geometric parameters of the Ni pillars and the membrane layers are unchanged from previous sections.

To simulate a waveguide-based resonator, we have to truncate the whole structure. Our example structure is truncated after 5 layers of the PnC structure, vertically, and after 4 layers of waveguide's side layers, horizontally. The resulting structure is shown in Fig. 31. We then apply fixed boundary conditions to the 4 sides of the structure (not shown in Fig. 31) to perform eigenmode and frequency response analysis.

The choice of fixed boundary condition is due to the shorter simulation time compared to when periodic boundary condition or PML are used. It should be noted that the inherent assumption in applying the fixed boundary condition is that the surrounding PnC layers provide adequate isolation from the elastic vibrations. Our comparative study of these boundary conditions show that there is negligible difference between the results of these different boundary conditions; hence, validating the effectiveness of the PnC layers in isolating elastic vibrations. Therefore, we will only discuss the results from applying the fixed boundary condition to the sides of the chosen waveguide-based resonator.

To calculate the eigenmodes of the waveguide-based resonator, one more optimization is applied to our model to further reduce the simulation time. Since the resonator structure has a symmetric geometry, both vertically and horizontally as seen in Fig. 31, it is possible to only model one quarter of the structure, and apply (anti-)symmetric boundary conditions to the two symmetry planes of the structure. In our example, we would need to run the eigenmode analysis 4 times with different combinations of symmetry and antisymmetry boundary conditions applied to the symmetry planes to find all the resonant modes of the structure.

Figure 32 shows the displacement profile of one of the resonant modes of our resonator at 1120 MHz when the symmetric boundary condition is applied to both symmetry planes of the structure. The perspective view of the quarter of the structure and the cross-section of the underlying membrane is shown in Fig. 32(a). The displacement profile of the whole structure—reassembled using the symmetry boundary conditions—is shown in Fig. 32(b). We can see that this mode has strong out-of-plane displacement component, making this mode possible to excite with the AlN layer of the membrane.

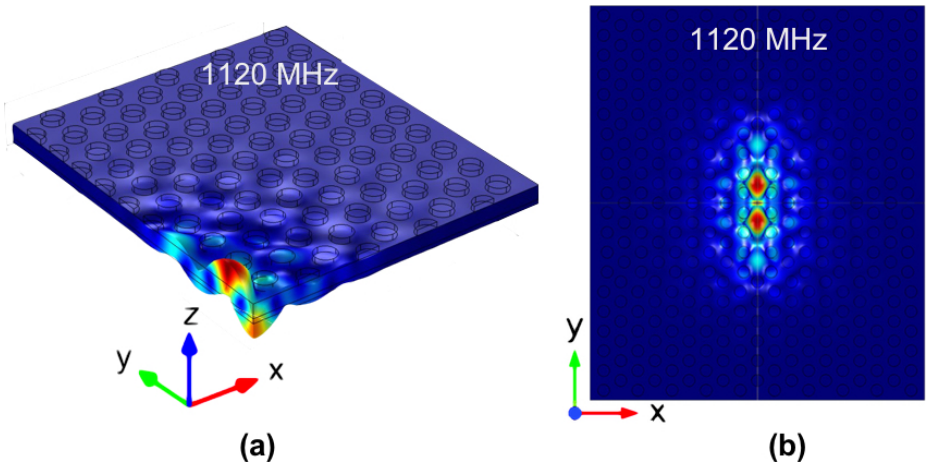

Figure 32: (a) Perspective view of the displacement profile of the resonant mode of the waveguide-based resonator and the cross-section of the underlying membrane; (b) Top view of the displacement profile of the whole structure reassembled using the symmetry boundary conditions.

The out-of-plane displacement component of the resonant mode at 1120 MHz along the center plane of the waveguide is shown in Fig. 33(a). The horizontal axis indicates the distance from the center of the resonator, increasing towards the PnC cap of the resonator. The peaks and valleys of this displacement profile are used to design the input and output electrodes to excite this resonant mode in a two-port network arrangement. One such design is shown in Fig. 33(b). The small electrodes in the cavity of the resonator are designed based on the displacement profile of the resonant mode at 1120 MHz. The two bus lines extending the length of the cavity

on both sides are added to the structure to provide the electrical connection. The electrodes and the bus line are modeled with an 80 nm thick Al layer on top of the membrane and beneath the Ni pillars. Similar to the lateral-mode resonator, we assume that the common ground of the network is connected to the underlying Mo layer.

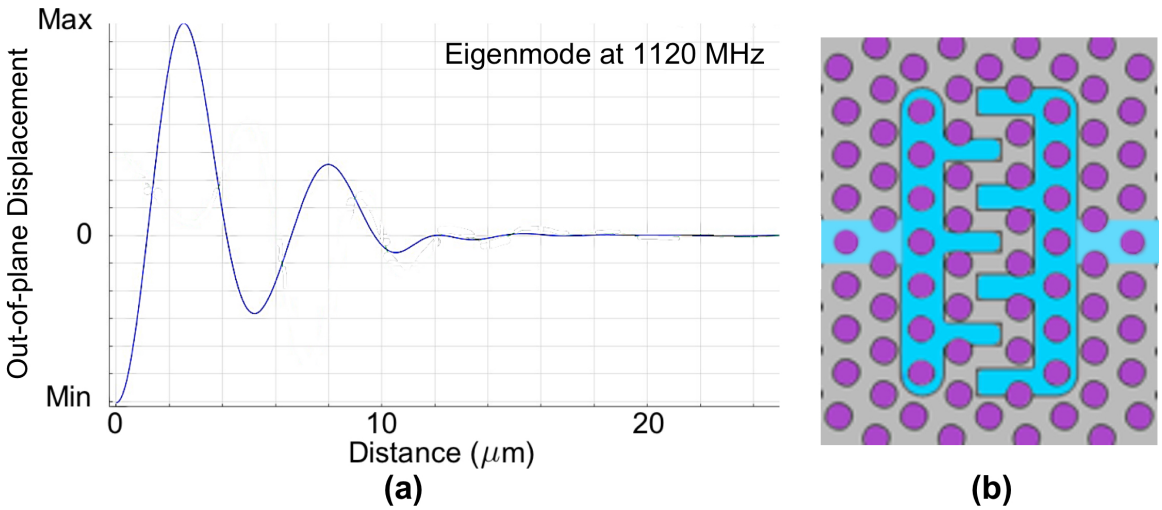

Figure 33: (a) Out-of-plane displacement of the resonant mode of the waveguide-based resonator in Fig. 32 at 1120 MHz along the center plane of the waveguide; (b) The pattern of the input and output electrodes matched to the resonant mode in Fig. 32.

With the designed electrodes, the frequency response analysis of the resonator can be conducted similar to the lateral-mode resonator. The result of this simulation is shown in Fig. 34. Multiple resonance peaks are seen in the frequency response; however, the peak at 1118 MHz is closest to the target eigenmode at 1120 MHz, and considering that this peak has the maximum transmission value, it corroborates the proposed design method for the excitation and sensing electrodes.

Several factors can cause the existence of other peaks. First, while we have designed the electrodes to have the best coupling to the eigenmode at 1120 MHz, this structure has other eigenmodes that the electrodes may excite, albeit suboptimally, at their eigenfrequencies. The second factor is that the Al bus line connecting the

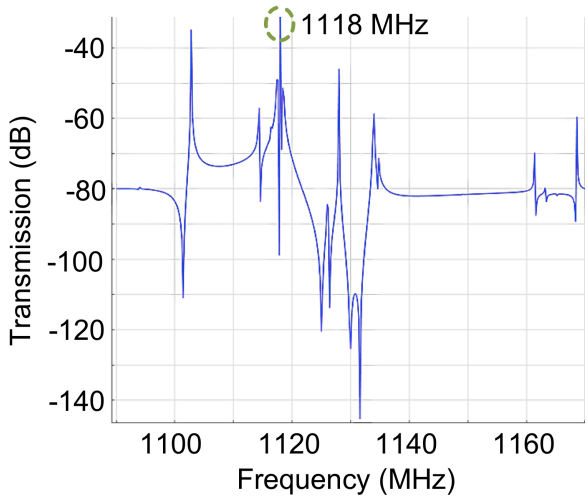

Figure 34: Frequency response of the directly excited waveguide-based resonator, the structure of which is illustrated in Fig. 33(b). Dashed circle show the resonance peak for this structure at 1118 MHz, for which the electrodes' patterns are optimized.

electrodes can itself act as an electrode exciting the lateral modes of the resonator. To minimize this effect, one can elongate the main electrodes, moving the bus line farther away from the resonator cavity.

CHAPTER IV

SURFACE ACOUSTIC WAVES AND PHONONIC CRYSTALS

SAW PnC devices, as discussed in Chapter 1, are easier to fabricate—since the device is not released as a membrane—and the final device is structurally more rigid and durable. SAW PnCs can suffer from the radiation loss and the coupling of the surface modes to the bulk modes in the interface of the SAW PnCs. Nevertheless, more straightforward fabrication process and the structural rigidity of SAW devices make this platform a viable competitor to the PnC membranes. Demonstration of very-high frequency PnBGs in SAW PnCs [1] has shown the potential for low-loss SAW PnCs.

Similar to our treatment of the membrane-based PnCs, to extend the utility of SAW PnCs in signal processing applications, design of SAW PnC waveguides are of great interest. Such designs should be made low-loss by tuning the frequency of the guided modes away from the sound cone (defined by the slowest elastic mode that is possible to propagate in the bulk material at any given frequency) to minimize the elastic energy loss from radiation to the bulk material. The waveguide designs also need to be accessible to the excitation and sensing electrodes to keep the insertion loss at reasonable levels.

In this chapter, we introduce two SAW-based PnC designs and illustrate the concept of partial PnBGs, a phenomenon observed in such devices. Building on this foundation, we introduce a simple waveguide design supporting multiple guided modes at frequencies close to the sound cone. We discuss the shortcomings of such design, and, to mitigate these limitations, step-by-step outline a waveguide design strategy that is

optimized for direct excitation, minimizes the radiation loss, and is only loosely dependent on the PnC lattice periodicity constraints—relaxing the constraints on sharp waveguide bends.

4.1 PnCs based on Surface Acoustic Waves

The building block of any periodic structure based on surface acoustic waves is similar to that based on the membrane-based PnCs, i.e., a PnC with a PnBG at the desired frequency range of operation. The unit cell of such a PnC should include a half-space bulk material and as such has, in theory, infinite depth. Modeling an infinitely deep structure can prove challenging. However, certain approximations enable us to simulate these structures with reasonable accuracy.

To model a SAW-based PnC, we should note that we are only interested in the elastic modes concentrated in the vicinity of the surface of the structure. Since these modes have limited penetration depth, the only region of the modeled geometry that can influence the surface modes is the neighborhood of the structure's surface. Therefore, choosing a sufficiently large depth for the structure should result in accurate results as far as the surface modes are concerned. We will refer to this model as the "truncated substrate" model and to the artificially created bottom boundary as the "false surface".

Under the truncated substrate model, the bulk modes inevitably will be distorted, and the simulation results pertaining to these modes should not be considered correct. In practice, we have two options related to the false surface of the truncated substrate. One choice is to use a PML boundary condition to approximate the infinite nature of the bulk material. This approach might help us obtain more accurate results on the existing bulk modes. Nevertheless, if we are not interested in bulk modes, which is the case in calculating the band structure of the SAW-based PnCs, we can opt for a second approach, applying a fixed boundary condition to the false surface. The fixed

boundary condition, unlike a simple free boundary condition, has the advantage of eliminating the unwanted surface modes of the false surface that can interfere with the results pertaining to the true surface of the structure.

To choose an appropriate depth parameter in order to approximate the bulk material, we need to keep in mind that the penetration depth of the surface modes are usually proportional to their wavelength, which itself depends on the lattice constant (a) in the case of PnC structures. In our models, we will use depth parameters ranging from $4a$ with PML on the false surface to $20a$ with fixed boundary condition on the false surface. These choices emerge from the trade-off between the need for accurate simulation results and the computational demands of the simulation.

To design a SAW-based PnC, one should introduce periodic features on the surface of the structure. These features can be etched holes with limited depth, inclusions embedded in the surface, or additional material deposited on the surface such as pillars. As such, pillar-based SAW PnCs consist of metallic or dielectric pillars deposited on the bulk material (i.e., substrate). There can be additional thin films of other material (e.g., piezoelectric layer used for excitation purposes) sandwiched between the pillars and the substrate.

As an example, Fig. 35 shows the band diagram of two square-lattice pillar-based SAW PnCs with Si substrate. Figure 35(a) shows the band diagram of a pillar-based SAW PnC made with copper (Cu) pillars, while Fig. 35(b) corresponds to a PnC with AlN pillars. The Cu pillars in Fig. 35(a) have a thickness and radius of $0.3a$ and $0.4a$, respectively, where a denotes the lattice constant. These parameters for AlN pillars in Fig. 35(b) are $0.4a$ and $0.4a$, respectively.

The thickness of the Si substrate, as discussed above, should be chosen large enough so that the surface waves on the true and false surfaces of the unit cell can be sufficiently decoupled. In these simulations, we have used a fixed boundary condition on the false side with a substrate thickness of at least $6a$.

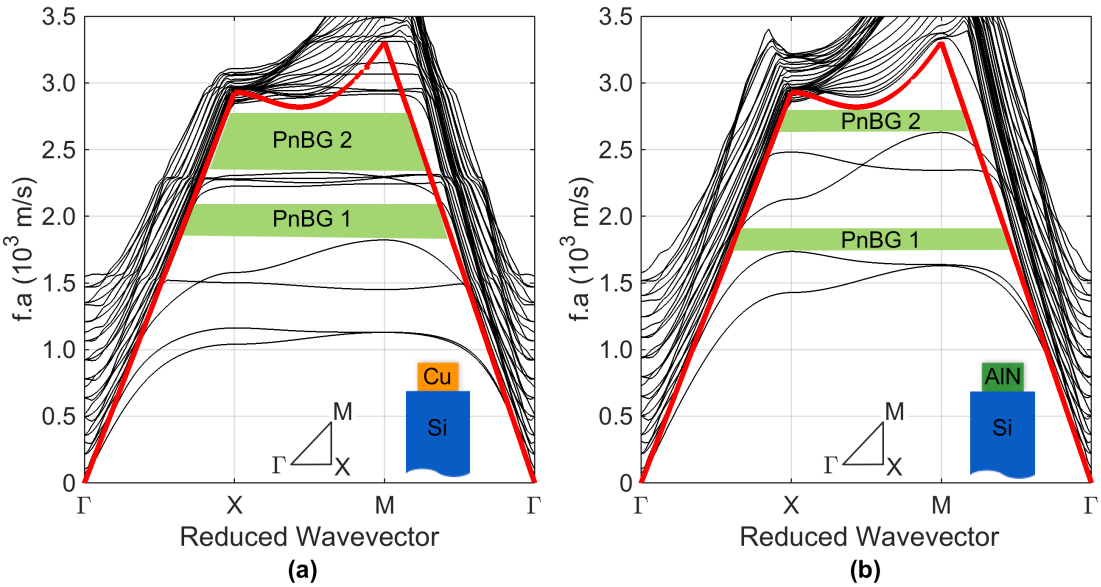

Figure 35: The band diagram of the pillar-based SAW PnCs composed of (a) Cu and (b) AlN pillars, both arranged in square lattice on a thick Si substrate. The radius and height of the Cu pillars in (a) are $0.4a$ and $0.3a$, respectively. The radius and height of the AlN pillars in (b) are $0.4a$ and $0.4a$, respectively. Thick red curves depict the sound cone, above which the bulk elastic modes appear. The extent of the partial PnBGs are shown by the light-colored boxes in the middle of the dispersion diagram. The insets in (a) and (b) show the cross-section of the truncated unit cells as well as the boundaries of the reduced Brillouin zone of the square lattice.

The sound cone [thick red curve in Figs. 35(a) and 35(b)] is calculated by finding the lowest phase velocity of the bulk acoustic modes in Si. As such, the region below the sound cone is where the surface modes appear without being coupled to the bulk modes.

The regions labeled as PnBG 1 and PnBG 2 in Figs. 35(a) and 35(b) highlight the frequency ranges where no *surface* mode exists. It should be stressed that the identified PnBG regions do not prohibit the existence of bulk modes—the modes that appear above the sound cone. It is only required for the surface modes to be out of the PnBG regions. Therefore, it is possible to identify a frequency range for PnBGs where bulk modes are present, as is the case in Figs. 35(a) and 35(b). As such, the PnBGs in SAW-based PnCs are in fact partial PnBGs, where only modes with a

minimum wavenumber at certain frequencies (as shown by the sound cone boundary) are prohibited to propagate on the surface.

To put the calculated range of frequencies of the above partial PnBGs in context, assume a lattice constant of 2μm for both the Cu- and AlN-based PnCs in Figs. 35(a) and 35(b). With this lattice constant, the radius of the pillars will be 800 nm, and their height will be 600 nm and 800 nm, for Cu and AlN pillars, respectively. These dimensions can be easily fabricated using the techniques outlined in previous chapters. With these geometric dimensions, the Cu-based PnC will support partial PnBGs around 1 GHz and 1.3 GHz. For the AlN-based PnC, the PnBGs occur around 925 MHz and 1.4 GHz. As such, we have shown a candidate design with the possibility of demonstrating GHz range PnBGs using practical pillar-based SAW PnC structures.

4.2 A Simple SAW-based Waveguide

As discussed in Chapter 3, one can design waveguiding structures by introducing a line defect in the lattice of a PnC. In the previous section, we demonstrated two SAW-based PnC designs that can be used for designing waveguides by altering their lattice structure. In this section, we will introduce practical waveguide designs using the aforementioned PnCs.

Figure 36 illustrates the schematic of the unit cell of one such waveguide design embedded in a square-lattice pillar-based SAW PnC. As shown in Fig. 36(a), a row of pillars in the middle of the structure is removed to create the defect region. The width of the waveguide region is shown in Fig. 36(a), where the initial width (i.e., the waveguide width resulting from the removal of one row of pillars without changing the distance between the two halves of the waveguide) is equal to the lattice constant a. As in Chapter 3, we can change the waveguide width to achieve the desired frequency of the guided modes.

The top and bottom sides of the waveguide unit cell in Fig. 36(a) are constrained with the Floquet boundary condition dictating the wavenumber of the eigenmodes supported by the structure. Additionally, the sides of the waveguide are truncated and enclosed between PMLs. Figure 36(b) shows that the truncated substrate is also bound by PML to approximate the infinite nature of the bulk material.

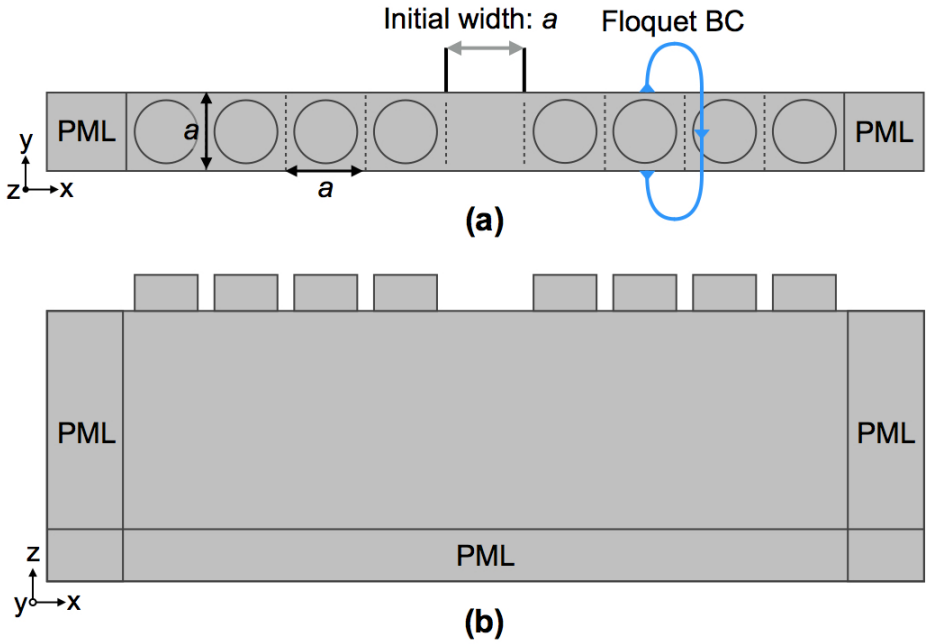

Figure 36: (a) The unit cell and (b) the cross-section of a pillar-based SAW PnC waveguide embedded in a square lattice. The thickness of the substrate layer is $4a$. The middle part of the waveguide—the defect region—is the result of removing one row of pillars from the square lattice. The number of the pillars on both sides of the structure is not representative of the actual design.

It should be stressed that the choice of PMLs instead of fixed boundary conditions is due to the large simulation domain of the SAW waveguide, which renders the simulation of large structures extremely time-consuming. Therefore, we have opted for a shallower substrate ($4a$) with fewer lateral layers of PnC to reduce the simulation time. To alleviate the effect of these approximate modeling techniques, boundary PMLs are used instead of fixed boundary conditions so as to make the models as realistic as possible.

Using the PnC design shown in Fig. 35(b), the pillars of which are AlN, we can materialize the waveguide design in Fig. 36. The dispersion diagram of this waveguide is shown in Fig. 37(a). The dashed lines indicate the extent of the partial PnBGs supported by the PnC used in this waveguide. The guided modes, therefore, are expected to appear inside the PnBG frequency range. The modes above the sound line [thick red line in Fig. 37(a)] are bulk modes and, therefore, are not of interest for our study.

As seen in Fig. 37(a), multiple modes appear in the PnBG region. We have shown the displacement profile of three of such modes at the high-symmetry point X in Fig. 37(b). It can be seen that these are waveguide modes with most of their energy concentrated in the defect region and close to the surface. However, as the frequency of these guided modes increases, the penetration depth of these modes increases as well. This is because at the high-symmetry point X, the higher the frequency is, the closer the modes are to the sound line. Of course, if we pass beyond the sound line, we should observe the modes that are not confined to the surface of the structure.

Our observation in Fig. 37(b), regarding the confinement of the modes to the surface, helps us recognize the importance of keeping a safe distance from the sound line in order to avoid large penetration depth and increased chance of radiation loss. In the next section, we will introduce more flexible designs to control the penetration depth and confinement of the guided modes.

4.3 Ridge Surface Waveguide

The waveguide design introduced in Sec. 4.2 suffers from a number of limitations:

1. Control over the penetration depth and lateral confinement of the waveguide mode in the simple waveguide design.

2. Ability to directly excite the waveguide modes. To address this problem, one might consider adding a piezoelectric layer on top of the Si substrate; however,

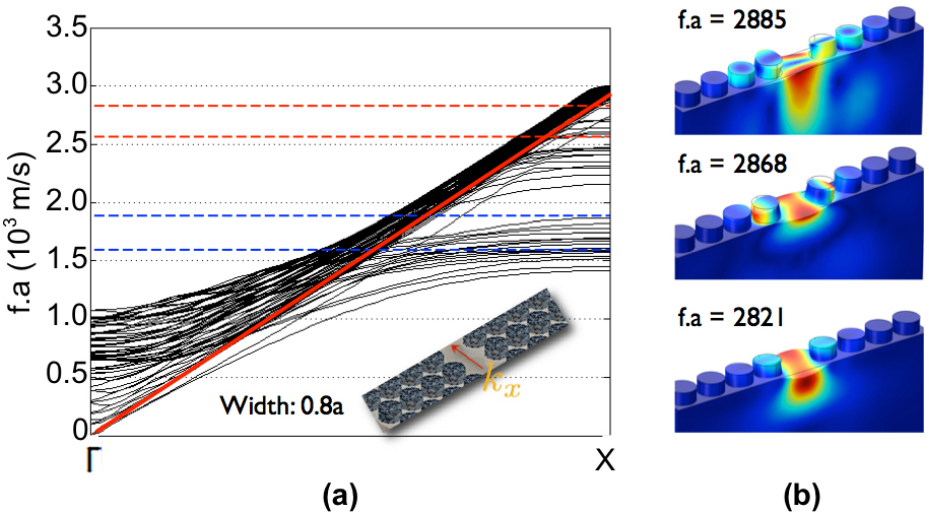

Figure 37: (a) The dispersion diagram and (b) the displacement profile of three of the guided modes of a simple pillar-based SAW PnC with AlN pillars on Si substrate. The geometric dimensions of the AlN pillars are the same as those in Fig. 35(b). The waveguide width, as defined in Fig. 36(a), is $0.8a$. The inset in (a) shows the direction of the wave propagation in the waveguide region as dictated by the Floquet boundary condition.

a structure with multilayer underlying substrate is hardly a simple design, and additional modes may exist thanks to the addition of a new layer, increasing the complexity of our design.

3. Lack of adequate design parameters to control the number of guided modes and their frequencies. As discussed previously, controlling the frequency of the guided modes—and keeping them away from the sound line—is a crucial step in designing a practical SAW-based PnC waveguide with reasonable radiation loss.

Addressing the limitations listed above requires a simple while flexible design that provides adequate design parameters to help mitigate and solve those limitations. In this section, we introduce one such design: *ridge surface waveguide*. Although this design, by itself, does not solve all the problems of the simple waveguide design in Sec. 4.2, it provides a platform that can effectively be modified and built-upon so

eventually, we end up with a practical waveguide design without the limitations of our earlier simple design.

Figures 38(a) and 38(b) show the structure of the unit cell of the ridge surface waveguide and its cross section, respectively. As shown in Fig. 38(a), the substrate of the structure is Si, and a ridge of AlN is patterned on top of the substrate. The chosen width of the AlN is $2a$, where a is the normalization parameter corresponding to the width of the waveguide unit cell, as shown in Fig. 38(a). The height of the AlN ridge is chosen to be $0.5a$, as seen in Fig. 38(b).

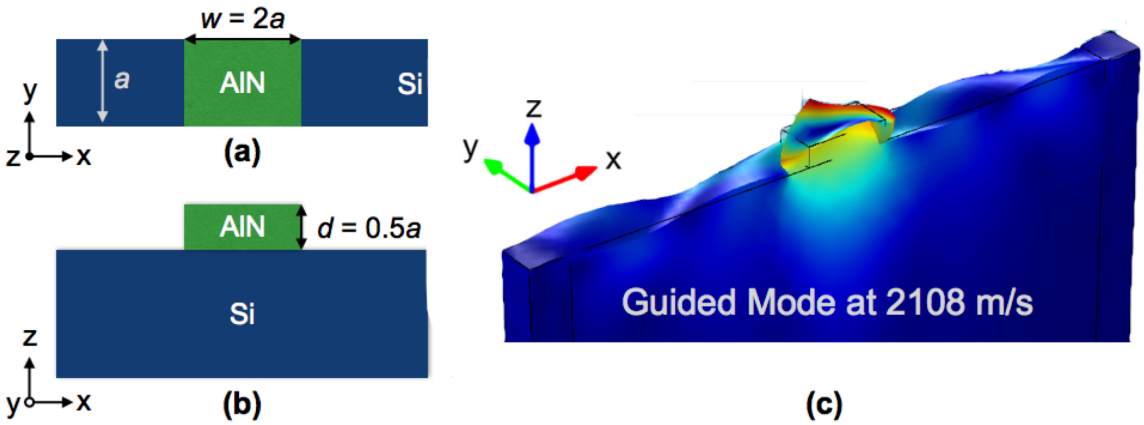

Figure 38: (a) The unit cell, (b) the cross-section, and (c) a sample displacement profile of the ridge surface waveguide, with Si substrate and AlN ridge. The normalized width and height of the AlN ridge are 2 and 0.5, respectively. The thickness of the substrate layer is $4a$. The simulated structure in (c) is surrounded by PML boundary layers.

To find the guided modes of this structure, we perform a FEM simulation following the steps detailed in Sec. 4.2. The usual PML boundary layers are applied to this structure as well, and the Floquet boundary condition applied to the sides of the structure in the y direction [as shown in Fig. 38(a)] determines the wavenumber of the eigenmode.

The displacement profile of a sample guided mode of this structure is shown in Fig. 38(c) at the normalized frequency of 2108 m/s. As seen in this mode profile, the

guided mode does not exhibit a reasonable lateral confinement, as the displacement profile easily reaches the PML boundary layers.

4.3.1 Improving the Lateral Confinement of the Ridge Surface Waveguide

One practical solution for controlling the lateral confinement of the ridge waveguide is to surround the AlN ridge between two regions of truncated SAW PnC having a PnBG at and around the guided mode's frequency. The stop band of the PnC will help improve the confinement of the guided mode.

We have already designed a PnC in Sec. 4.1 that can confine the guided modes of the ridge waveguide—the PnC with the Cu pillars. Surrounding the AlN ridge with this PnC results in the structure shown in Fig. 39. As shown in this figure, the definition of the geometric parameters of the ridge waveguide is unchanged from those of Figs. 38(a) and 38(b); however, an additional parameter ($dist$) is defined that controls the distance between the truncated PnC sections (on the left and right of the structure) and the AlN ridge. The radius and height of the Cu pillars are the same as those in Sec. 4.1, i.e., $0.4a$ and $0.3a$, respectively.

It should be noted that this structure is not a defect-based waveguide design as the one in Sec. 4.2. A defect-based waveguide design results from small perturbations in the periodic structure of the PnC lattice, e.g., slightly changing the distance between two layers of the pillars, in the case of the waveguide introduced in Sec. 4.2. On the contrary, the design illustrated in Fig. 39 shows a drastic change in the structure of the PnC that includes increasing the distance between two rows of the PnC by a multiple factor of a and adding a third structural element, i.e., the AlN ridge, between these two rows. These structural changes make the PnC-surrounded ridge waveguide a completely new structure with its unique properties compared to that of the PnCs surrounding the structure.

Examining the displacement profile of the guided modes supported by the ridge

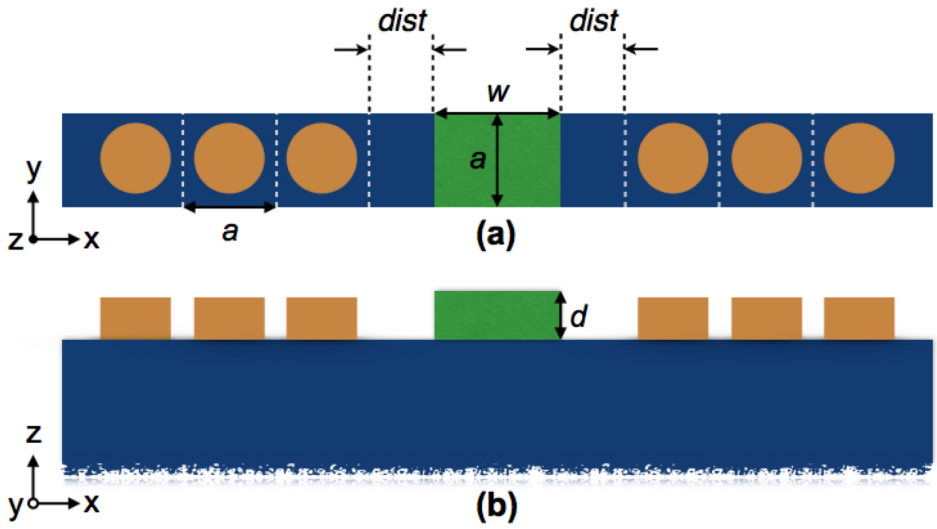

Figure 39: (a) The unit cell and (b) the cross-section of a ridge surface waveguide surrounded by the pillar-based SAW PnC with Cu pillars on Si substrate and AlN ridge. The radius and height of the Cu pillars are $0.4a$ and $0.3a$, respectively. The thickness of the Si substrate is $4a$. The number of the Cu pillars on both sides of the structure is not representative of the actual design.

waveguide and its PnC-surrounded counterpart can prove the effectiveness of PnCs in improving the lateral confinement of the guided modes. For this purpose, we choose two guided modes of the ridge waveguide at f.a = 2591 m/s and f.a = 2615 m/s with the Floquet boundary condition set at $k_y = \pi/a$. The corresponding modes, when the AlN ridge is surrounded by Cu pillars, are at f.a = 2613 m/s and f.a = 2638 m/s, respectively. Note that the width (w) and height (d) of the ridge in these simulations are $2a$ and $0.5a$, respectively. The *dist* parameter, defined in Fig. 39(a), is set to $1a$.

The displacement profiles of the PnC-surrounded ridge waveguide are shown in Figs. 40(a) and 41(a), for f.a = 2613 m/s and f.a = 2638 m/s, respectively. The displacement profiles of the corresponding ridge waveguide are shown in Figs. 40(d) and 41(d), for f.a = 2591 m/s and f.a = 2615 m/s, respectively.

The choice of these modes are such that they can be easily excited by the piezoelectric property of the ridge section, provided that a thin electrode is patterned on top of the AlN ridge [see Item 2 in the beginning of Sec. 4.3]. Both of these modes

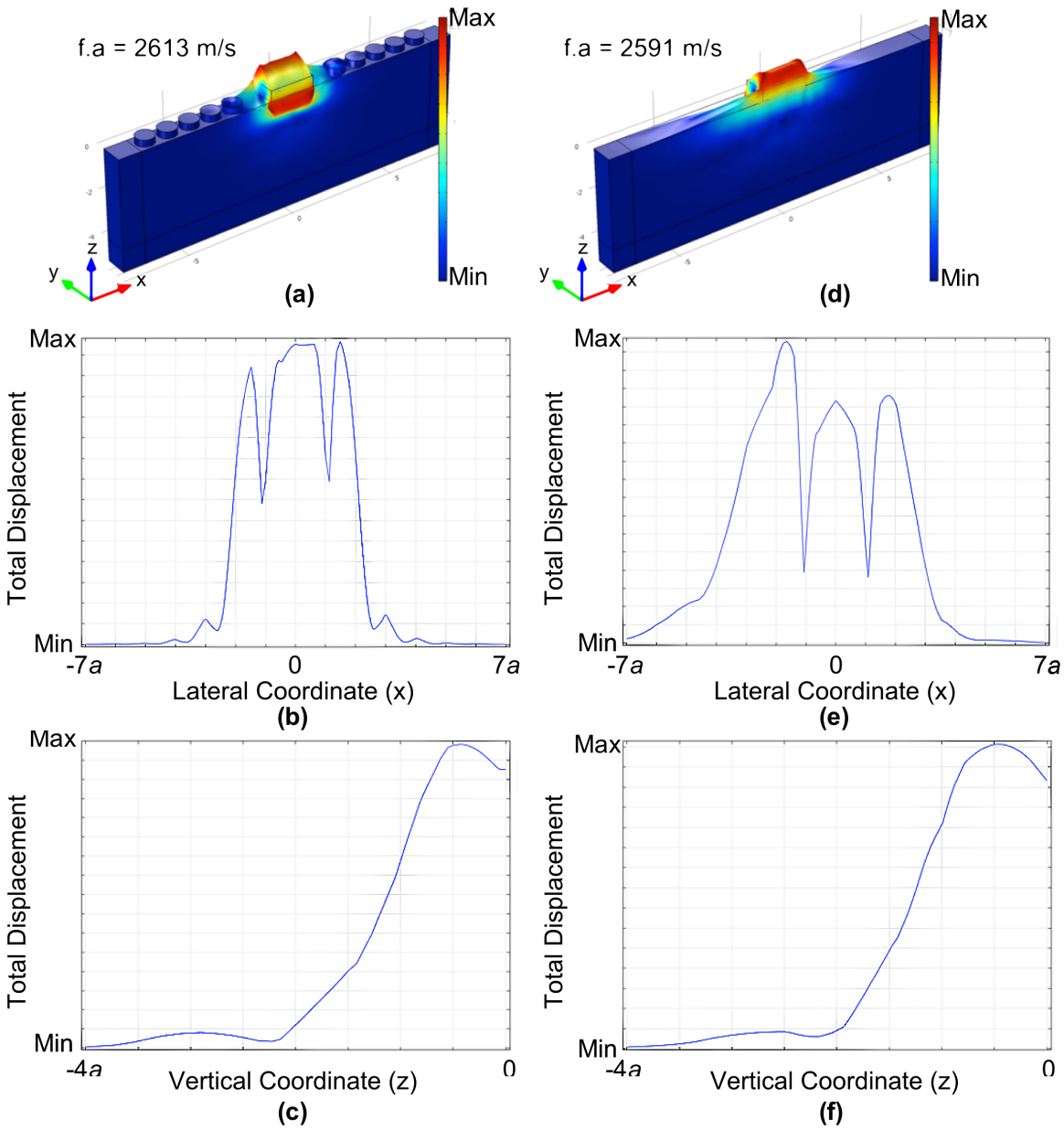

Figure 40: (a) The displacement profile and (b) its lateral and (c) vertical variation of the PnC-surrounded ridge waveguide for the guided mode at f.a = 2613 m/s. (d) The displacement profile and (e) its lateral and (f) vertical variation of the ridge waveguide for the guided mode at f.a = 2591 m/s.

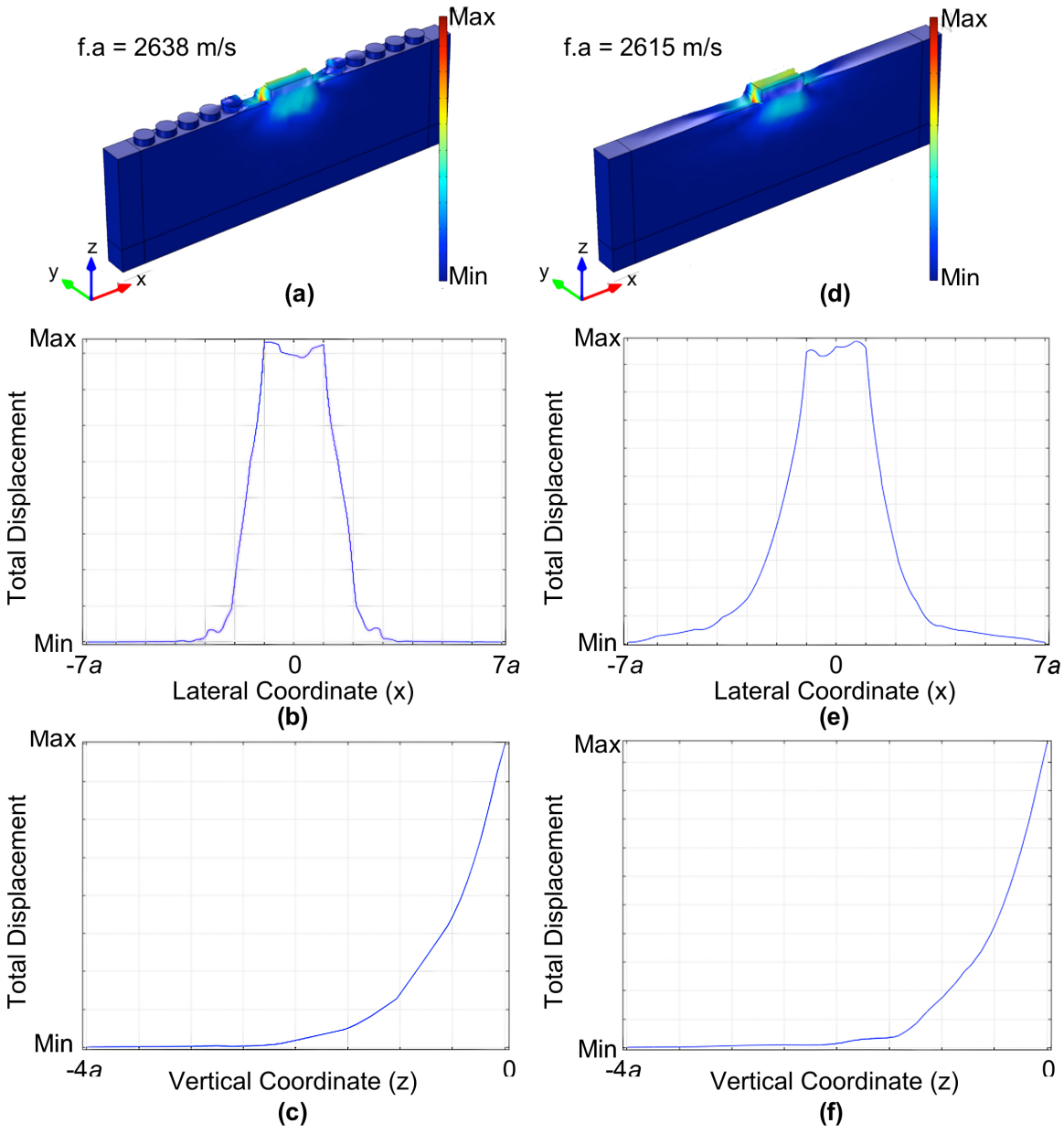

Figure 41: (a) The displacement profile and (b) its lateral and (c) vertical variation of the PnC-surrounded ridge waveguide for the guided mode at f.a = 2638 m/s. (d) The displacement profile and (e) its lateral and (f) vertical variation of the ridge waveguide for the guided mode at f.a = 2615 m/s.

have strong shear vertical (SV) and longitudinal (L)displacement components. With this consideration in mind, it should be noted that the mode shown in Fig. 38(c) can not be effectively excited by the AlN ridge, as it has a dominant shear horizontal (SH) polarization.

We can observe from the provided displacement profiles the improved lateral confinement of the guided modes when surrounded by Cu pillars. For example, Fig. 40(b) shows the total displacement of the guided mode at f.a = 2613 m/s along a line extending from $x = -7a$ to $x = 7a$ with its y and z coordinates fixed such that the line passes through the middle of the waveguide unit cell on the surface of the Si substrate and underneath the AlN ridge and Cu pillars. As such, in this figure, $x = 0$ indicates the center of the waveguide and AlN ridge. The same displacement profile for the mode at f.a = 2591 m/s is shown in Fig. 40(e).

Comparing the total displacement variation in Figs. 40(b) and 40(e) indicate that the structure with Cu pillars exhibits a stronger mode confinement, as the total displacement rapidly drops to zero for $|x| > 2a$. This is not clearly the case for the ridge waveguide without the surrounding PnC layers, as the total displacement value has a non-negligible value even for $|x| = 4a$.

Performing the comparison above for Figs. 41(b) (for the mode at f.a = 2638 m/s) and 41(e) (for the mode at f.a = 2615 m/s) reveals a similar phenomenon. The total displacement value for the PnC-surrounded waveguide become negligible for $|x| > 3a$; however, for the bare ridge waveguide, the total displacement value remains significant for $|x| = 6a$.

Adding PnC layers around the AlN ridge, while improving the lateral confinement of the guided modes, raises the logical concern about the penetration depth of the modes. To put this concern to rest, we can examine the total displacement of the guided modes for the two designs along a vertical line passing through the middle of the waveguide unit cell (i.e., $x = 0$) from $z = -4a$ to $z = 0$.

Figures 40(c) (for the mode at f.a = 2613 m/s) and 40(f) (for the mode at f.a = 2591 m/s) show the total displacement variation along the vertical line defined above. It can be seen that no significant difference between these two displacement profiles exists. The same observation can be made for the displacement profiles shown in Figs. 41(c) (for the mode at f.a = 2638 m/s) and 41(f) (for the mode at f.a = 2615 m/s), where no significant change can be observed for the structure with the Cu pillars around the AlN ridge.

The aforementioned observations corroborate our initial assumption—and design philosophy—that surrounding the ridge surface waveguide with layers of pillar-based SAW PnCs can improve the lateral confinement of the guided modes. It is interesting to see that such modification of the waveguide structure does not deteriorate the penetration depth of the guided modes; hence, having little impact on the radiation loss. These modifications, therefore, address the concerns outlined in Item 1 in the beginning of Sec. 4.3.

It should be noted that the presence of Cu pillars causes a slight increase—less than 1%—in the frequency of the guided modes. This is a small penalty to improve the mode confinement of the waveguide.

4.3.2 Optimizing the Geometric Parameters of the PnC-surrounded Ridge Waveguide

After augmenting the ridge surface waveguide with the surrounding PnC layers, the next step is to optimize the frequency of the guided modes to keep them away from the sound line. If successful, this will address the last concern discussed in the beginning of Sec. 4.3 (see Item 3).

In the previous sections, we examined the PnC-surrounded ridge waveguide with the geometric parameters that were chosen intuitively, namely $w = 2a$, $d = 0.5a$, and $dist = 1a$. Thus far, we have been investigating individual guided modes of this structure, with no regard to their relative position to the sound line. One can

visualize this relative position by calculating the dispersion diagram of this waveguide design.

Figure 42 shows the dispersion diagram of the PnC-surrounded ridge waveguide, with the mentioned geometric parameters. The red dots indicate the guided (i.e., confined) modes, while the blue ones indicate the leaky modes. The thick orange line indicates the sound line, and the dashed lines show the extent of the partial PnBGs of the SAW-based PnC with Cu pillars surrounding the AlN ridge. The bulk modes above the sound line are not shown in this figure.

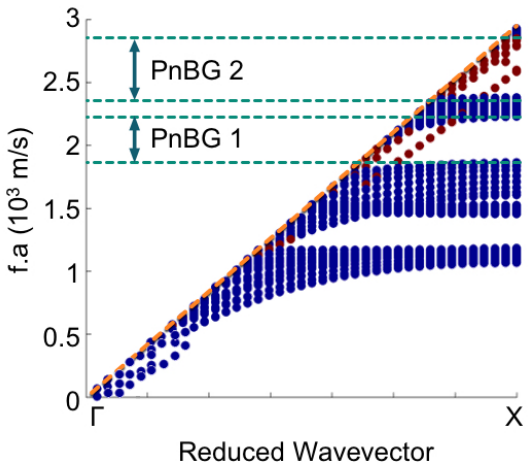

Figure 42: The dispersion diagram of the PnC-surrounded ridge waveguide. The red and blue dots indicate the guided and leaky modes, respectively. The thick orange line indicates the sound line, and the dashed lines show the extent of the partial PnBGs of the SAW-based PnC with Cu pillars surrounding the AlN ridge. The bulk modes above the sound line are not shown in this figure. The geometric parameters of the simulated structure are $w = 2a$, $d = 0.5a$, and $dist = 1a$. The radius and height of the Cu pillars are $0.4a$ and $0.3a$, respectively.

As seen in Fig. 42, two guided modes are supported by the structure at the high-symmetry point X. It can be seen that these modes are very close to the sound line, and, as discussed in Sec. 4.2, this proximity to the sound line results in suboptimal penetration depth leading to higher radiation loss.

Since our PnC-surrounded ridge waveguide has at least three design parameters—i.e., w, d, and $dist$—we can perform an exhaustive search in the design domain to

lower the frequency of the guided modes as much as possible.

One of the geometric parameters of the PnC-surrounded ridge waveguide is the height of the AlN ridge, d. It is important to have an intuitive understanding of the effect of this parameter on the frequency of the guided modes, and realize that the effects of these geometric parameters are not straightforward to predict.

Considering that the most of the elastic energy of the guided modes is concentrated in the AlN ridge section of the waveguide, given the wavelength, the higher the stiffness of this section, the higher the supported propagating wave frequency.[1]

The mass density of the ridge section can also have significant effect on the frequency of the propagating modes. Given the wavelength, the lower the mass density, the higher the guided mode frequency.

Taking into account the effect of the stiffness and mass density of the AlN ridge, we can investigate the effect of the parameter d on the frequency of the guided modes. Assuming that we reduce d, the effective stiffness of the ridge will decrease—lowering the frequency of the guided modes, while this reduction in d will result in reduced mass density (i.e., mass per unit length) of the ridge. The decrease in the mass density will have the contradictory effect of increasing the frequency of the guided modes.

The opposing effects resulting from changing the thickness of the ridge lead us to perform a parametric sweep simulation and calculate the actual frequencies of the guided modes for varying values of d. The result of this parametric sweep is shown in Fig. 43.

As seen in Fig. 43, as we decrease d, the frequencies of the guided modes of the PnC-surrounded ridge waveguide decrease. It can also be seen that the trend of the decrease flattens as the height of the ridge approaches $0.3a$. The overall effect of decreasing the height of the AlN ridge from $0.5a$ to $0.3a$ is a reduction of 1.9%

[1]This is the case here as the lattice constant is constant, and the Floquet boundary condition is applied for a given wavenumber, i.e., high-symmetry point X in the dispersion diagram.

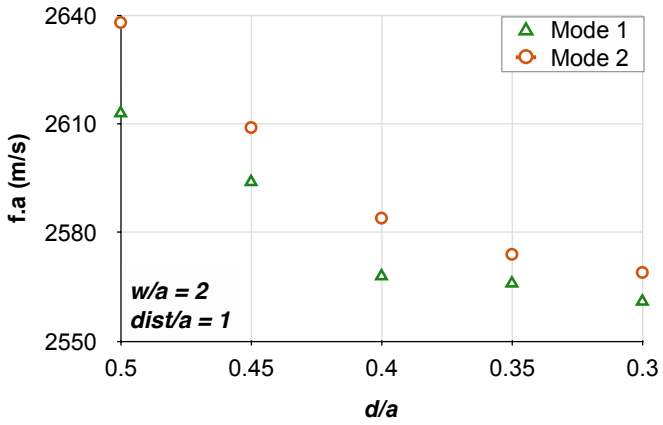

Figure 43: The frequencies of the guided modes of the PnC-surrounded ridge waveguide at the high-symmetry point X with respect to the thickness of the AlN ridge. The two guided modes supported by the structure at the high-symmetry point X are denoted by Mode 1 (green triangles) and Mode 2 (orange circles). The geometric parameters w and $dist$ are fixed at $2a$ and $1a$, respectively. The ridge is surrounded by the same Cu pillars as shown in Fig. 39.

and 2.6% in the frequencies of Modes 1 and 2 (i.e., the guided modes of the PnC-surrounded ridge waveguide), respectively.

In order to examine the effect of the width of AlN ridge on the frequencies of the guided modes, we conducted two parametric sweeps over the width parameter. The results of these simulations are summarized in Figs. 44(a) and 44(b).

Figure 44(a) shows the change of the frequency of Modes 1 and 2 with respect to the normalized value of the parameter w for the PnC-surrounded ridge waveguide with $d = 0.5a$ and $dist = 1a$. Mode 1 attains its minimum frequency in Fig. 44(a), $\mathrm{f}.a = 2584\,\mathrm{m/s}$, at $w/a = 1.8$. The minimum frequency for Mode 2 in Fig. 44(a), $\mathrm{f}.a = 2587,\mathrm{m/s}$, is obtained when $w/a = 1.7$.

The result of the parametric sweep for the PnC-surrounded ridge waveguide with $d = 0.3a$ is shown in Fig. 44(b). In comparison with Fig. 44(a), we can see that all the instances of Modes 1 and 2 for the different values of w/a for $d = 0.3a$ are below their corresponding value for $d = 0.5a$.

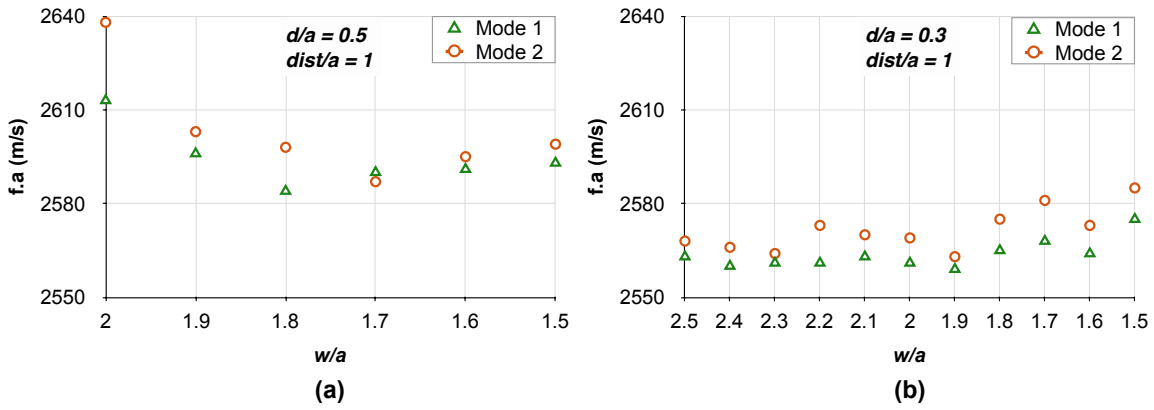

Figure 44: The frequencies of the guided modes of the PnC-surrounded ridge waveguide at the high-symmetry point X with respect to the width of the AlN ridge for (a) $d = 0.5a$ and (b) $d = 0.3a$. The two guided modes supported by the structure at the high-symmetry point X are denoted by Mode 1 (green triangles) and Mode 2 (orange circles). The geometric parameter *dist* is fixed at $1a$ for both (a) and (b). The ridge is surrounded by the same Cu pillars as shown in Fig. 39.

In order to minimize the frequencies of the guided modes, the simulation results summarized in Figs. 43 and 44 suggest that the AlN ridge with thickness $0.3a$ produces minimum frequencies for Modes 1 and 2.

Figure 44(b) also suggests that varying the parameter w, when $d = 0.3a$, from $2.5a$ to $1.5a$ can only change the frequencies of the guided modes by at most $\pm 1\%$, as compared to the baseline values for $w = 2a$. Based on this observation, we will keep w at $2a$, because the variations in w will not provide significant change in the frequencies of the guided modes.

The *dist* parameter is the last parameter whose effect on the frequencies of the guided modes can be investigated. Figure 45 shows this effect, summarizing the result of the parametric sweep study on *dist* and illustrating the frequencies of the guided modes. We have conducted this simulation on the PnC-surrounded ridge waveguide with AlN ridge height of $0.3a$, as this value gives the lower-frequency modes compared to a ridge height of $0.5a$.

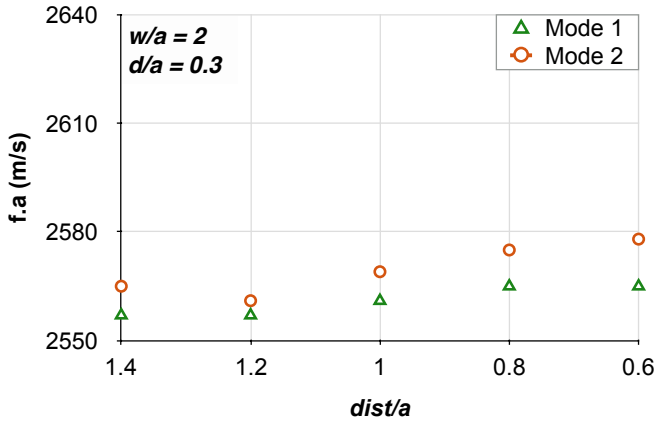

Figure 45: The frequencies of the guided modes of the PnC-surrounded ridge waveguide at the high-symmetry point X with respect to the distance of the PnC layers from the AlN ridge. The two guided modes supported by the structure at the high-symmetry point X are denoted by Mode 1 (green triangles) and Mode 2 (orange circles). The geometric parameters w and d are fixed at $2a$ and $0.3a$, respectively. The ridge is surrounded by the same Cu pillars as shown in Fig. 39.

Similar to our observation in Fig. 44(b), we can see that changing the *dist* parameter changes the frequencies of the guided modes by at most $\pm 1\%$. Therefore, we conclude that for a ridge with $w = 2a$ and $d = 0.3a$, the *dist* parameter does not have a significant effect on tuning the frequencies of the guided modes.

4.4 Ladder Surface Waveguide

In Sec. 4.3.2, we set out to optimize the geometric dimensions of the PnC-surrounded ridge surface waveguide to obtain guided modes as low-frequency—and as far away from the sound line—as possible. However, our efforts in this direction have only resulted in lowering the frequency of the guided modes by at most 2%, compared to the frequencies of the guided modes of a bare ridge surface waveguide. Consequently, our third objective in the beginning of Sec. 4.3 is not fulfilled, yet. However, we were able to develop an understanding of the effect of simple physical concepts, namely, mass density and effective stiffness, on the frequencies of the guided modes. In this

section, we use this understanding to implement changes in the structure of the PnC-surrounded ridge waveguide that can help us to lower the frequencies of the guided modes.

Recall from the previous section that reducing the effective stiffness of the AlN ridge results in lowering the frequency of the guided modes. However, as we concluded from the results shown in Figs. 43 and 44, simply changing the width or thickness of the AlN ridge changes the mass density, which nearly cancels out the opposing effect of any changes in the effective stiffness.

The limited effect of the geometric dimensions forces us to consider more drastic changes to the structure of the AlN ridge. One such change is to break apart the AlN ridge into separate *splits*, as shown in Fig. 46(a). We can study the effect of the AlN ridge splitting on the frequencies of Modes 1 and 2 using the parametric sweep study over the split length parameter (s) as defined in Fig. 46(a). Figure 46(b) shows the result of the parametric sweep for a bare split-ridge surface waveguide (i.e., with no surrounding PnC layers) with $w = 2a$ and $d = 0.3a$.

Splitting the AlN ridge produces conflicting effects of mass density and the effective stiffness—similar to the ridge surface waveguide. However, as can be seen in Fig. 46(b), reducing the split length from $s = 1a$ (which effectively is a continuous ridge) to $s = 0.8a$ results in 13% and 8% reduction in the frequency of Modes 1 and 2. This change is a significant departure from the results of our methods in the previous section and produces a much needed reduction in the frequencies of the guided modes.

While splitting the AlN ridge helps us lower the frequencies of the guided modes, it is not a practical solution. Recall from Sec. 4.3 that one of the main concerns regarding the design of a surface waveguide is our ability to directly excite the guided modes using the piezoelectric property of an active layer, i.e., AlN in our structures. Nevertheless, splitting the AlN ridge makes it practically impossible to pattern a

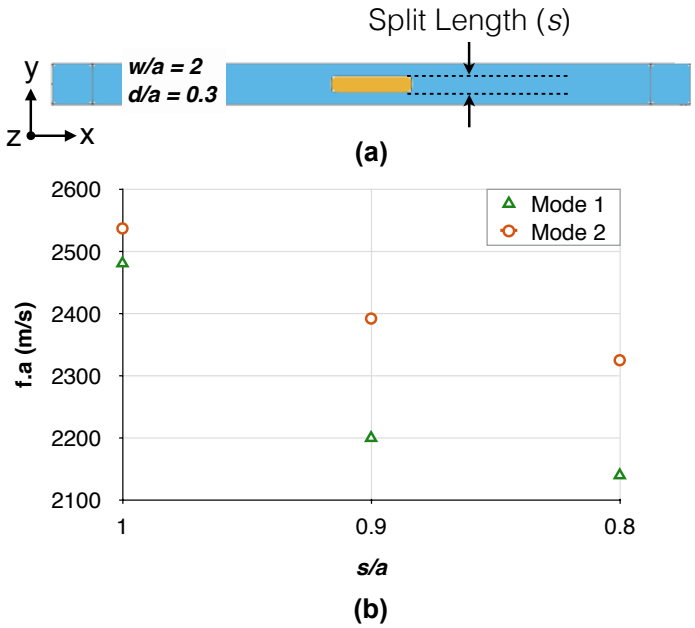

Figure 46: (a) Unit cell of the split-ridge waveguide and (b) the frequencies of the guided modes of the waveguide in (a) at the high-symmetry point X with respect to the length of the split in AlN ridge. The two guided modes supported by the structure at the high-symmetry point X are denoted by Mode 1 (green triangles) and Mode 2 (orange circles). The geometric parameters w and d are fixed at $2a$ and $0.3a$, respectively.

continuous electrode on top of the AlN.

To keep the excitability of the waveguide, we need to make a compromise in the structure of the AlN ridge, inspired by the success of the split ridge. A simple design that can keep the AlN section of the waveguide connected, while having the beneficial effect of lowering the frequencies of the guided modes, is illustrated in Fig. 47(a).

As seen in Fig. 47(a), the reduction in the stiffness of the AlN ridge is achieved by making a ladder structure from the whole ridge. This has the same benefit of completely splitting the AlN ridge, while keeping the structural continuity of the AlN layer by the side spokes. The spokes width in this design is chosen to be $0.25a$. Therefore, a ridge width of $w = 2a$ leaves a void region as wide as $1.5a$ in the middle of the AlN. The definition of the split length (s) is the same as that of the split-ridge waveguide.

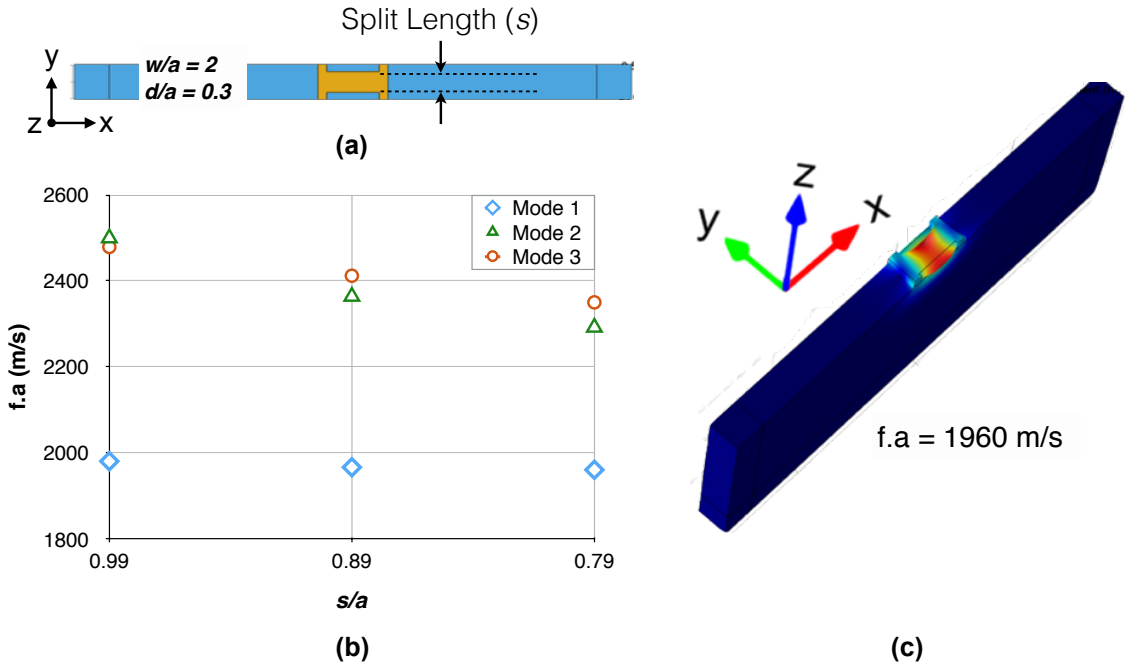

Figure 47: (a) Unit cell of the ladder waveguide, (b) the frequencies of the guided modes of the waveguide in (a) at the high-symmetry point X with respect to the length of the split in the AlN ridge, and (c) the displacement profile of a low-frequency mode supported by the ladder waveguide with the split length $0.75a$. The three guided modes supported by the structure at the high-symmetry point X are denoted by Mode 1 (blue diamonds), Mode 2 (green triangles), and Mode 3 (orange circles). The geometric parameters w and d are fixed at $2a$ and $0.3a$, respectively.

Figure 47(b) shows the frequencies of the guided modes supported by the ladder waveguide shown in Fig. 47(a) as a function of the split length parameter. In this figure, not only we can see that the two highest frequency modes (i.e., Modes 2 and 3) exhibit a significant reduction in their frequencies (as we reduce s from $0.99a$, modeling an almost continuous AlN ridge), to $0.79a$, but also we observe a third low-frequency guided mode denoted as Mode 1, the frequency of which reaches f.a = 1960 m/s. This frequency for a guided mode is the lowest we have seen in our designs, which shows a great promise in achieving our goal outlined in Item 3 in the beginning of Sec. 4.3.

Examining the displacement profile of Mode 1 of the ladder waveguide for s =

$0.75a$, shown in Fig. 47(c), reveals that this guided mode is reasonably confined—both laterally and vertically—even when it is not surrounded by the PnC layers. It also shows that Mode 1 has a strong longitudinal polarization component that can be easily excited by the piezoelectric property of the AlN layer through patterned electrodes on top of the ladder layer.

Since the ladder structure supports a new low-frequency guided mode, we can re-examine the dispersion diagram of the PnC-surrounded ridge waveguide, shown in Fig. 42, replacing the AlN ridge with the new ladder structure and the geometric parameters $w = 2a$, $d = 0.3a$, $s = 0.75a$, while surrounding the middle AlN ladder structure with the same PnC layers as those in Fig. 42 and $dist = 1a$. Figure 48 illustrates the dispersion diagram of this structure.

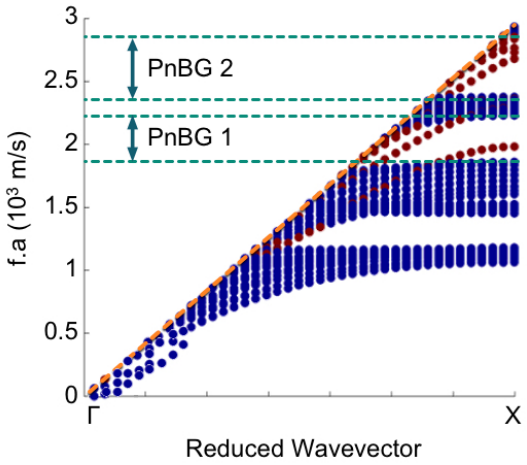

Figure 48: The dispersion diagram of the PnC-surrounded ladder waveguide. The red and blue dots indicate the guided and leaky modes, respectively. The thick orange line indicates the sound line, and the dashed lines show the extent of the partial PnBGs of the SAW-based PnC with Cu pillars surrounding the AlN ladder. The bulk modes above the sound line are not shown in this figure. The geometric parameters of the simulated structure are $w = 2a$, $d = 0.3a$, $s = 0.75a$, and $dist = 1a$. The radius and height of the Cu pillars are $0.4a$ and $0.3a$, respectively.

The three guided modes supported by the ladder waveguide can be seen in Fig. 48. Mode 1 is in the frequency range of the partial PnBG 1, while Modes 2 and 3 are in the frequency range of the partial PnBG 2. The extent of the partial PnBGs,

supported by the PnC layers around the ladder structure, is shown by dashed lines in Fig. 48. We can observe that Mode 1 is sufficiently far from the sound line, shown as the thick orange line, therefore, promising a reasonable penetration depth and low radiation loss.

4.5 Cross-bar Surface Waveguide

The ladder structure introduced in Sec. 4.4 is not the only possible geometry for keeping the continuity of the AlN section of the waveguide. While it provides the ability to pass two sets of electrodes on the two sides of the ladder, facilitating the excitation of the guided modes, as we have seen previously, we can drive an AlN layer using one bottom electrode and one on top. Consequently, we don't need two spokes on the two sides to keep the AlN a connected body, but rather a single spoke in the middle is enough for this purpose.

Figure 49(a) shows the structure of the aforementioned single-spoke ridge waveguide, surrounded by the same PnC layers as those in Fig. 39. We will refer to this structure as cross-bar surface waveguide.

To investigate the efficacy of the cross-bar surface waveguide in lowering the frequencies of the guided modes—or supporting lower-frequency modes—we calculate the dispersion diagram of the cross-bar waveguide. Figure 49(b) illustrates the calculated dispersion diagram for this structure. We can observe in this dispersion diagram that the cross-bar waveguide not only lowers the frequencies of the highest-frequency guided modes (i.e., the guided modes in the frequency range of the partial PnBG 2), but also it produces multiple lower-frequency guided modes in the frequency range of the partial PnBG 1.

While a single-mode waveguide is usually preferable in practice, the cross-bar waveguide shows the flexibility of a single piezoelectric guiding medium deposited on

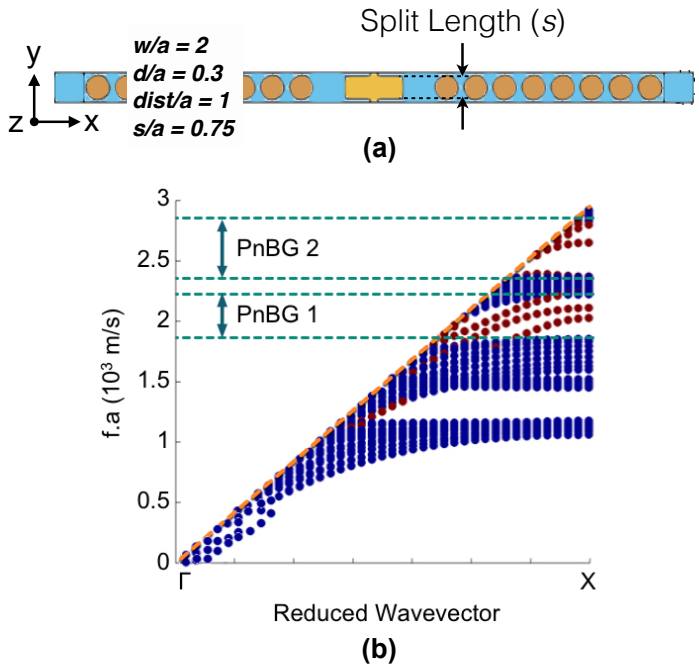

Figure 49: (a) Unit cell and (b) the dispersion diagram of of the PnC-surrounded cross-bar waveguide. The geometric parameters of the simulated structure are $w = 2a$, $d = 0.3a$, $s = 0.75a$, and $dist = 1a$. The radius and height of the Cu pillars are $0.4a$ and $0.3a$, respectively. The red and blue dots in (b) indicate the guided and leaky modes, respectively. The thick orange line indicates the sound line, and the dashed lines show the extent of the partial PnBGs of the SAW-based PnC with Cu pillars surrounding the AlN cross-bar. The bulk modes above the sound line are not shown in this figure.

the substrate. In fact, all the variations of the ridge waveguide—including the PnC-surrounded structures, the ladder waveguide, and the cross-bar structure—support our initial proposition that the ridge geometry provides much more degrees of freedom and a vast design space so that one can tailor the waveguide structure making it suitable for any application.

CHAPTER V

EPILOGUE

5.1 Brief Summary of Contributions

The objective of this thesis was to develop a novel high-frequency signal processing platform using pillar-based phononic crystals. The reason for our choice of pillar-based PnCs was their ability to provide more design parameters while reducing the stringent fabrication requirements imposed by other PnC structures. To accomplish our goal, we set out to build a theoretical and intuitive understanding of the physics of bandgap formation in the pillar-based PnCs. We then used this understanding to design and experimentally demonstrate GHz PnBGs using pillar-based PnCs. Design and demonstration of a GHz waveguide was the next step in our efforts to develop a complete toolbox for signal processing systems using pillar-based PnCs. During these investigations, we always strived for practical solutions. This consideration led us to expand our investigation to surface acoustic wave devices that provide superior structural rigidity and benefit from feasible fabrication process. We believe this thesis provides a strong foundation for future research endeavors on advancing the science and technology of phononic crystals in the GHz frequency range for signal processing applications.

Our theoretical studies started with investigating the physics of PnBG formation in pillar-based PnCs with W pillars on a Si membrane. The existence of multiple PnBGs in three lattice symmetries (i.e., square, triangular, and honeycomb) and the comparison of these PnBGs for different pillar geometries reveal that two simultaneous factors, namely, Bragg scattering and the resonance of individual pillars (a.k.a., local resonance), contribute to the formation of PnBGs in these PnCs. The dominant

effect of Bragg scattering was shown in different lattice types where the position of the PnBGs has inverse relation with the lattice period. On the other hand, the PnBGs that are formed due to the local resonance of pillars occur at similar frequency in different lattice types. Moreover, it was shown that by increasing the height of pillars the effect of local resonance became more dominant and for $h/a > 1.0$, the three studied lattice types showed identical PnBGs for identical pillar dimensions. Examining the effect of lattice perturbation on the PnBGs also shows that the PnBGs for short pillars, where the effect of Bragg scattering is dominant, are greatly affected by small perturbations whereas for taller pillars the lattice perturbation does not have significant effect on the PnBGs.

To experimentally demonstrate the existence of GHz PnBGs in the pillar-based PnC membranes, we developed fabrication processes optimized for the required feature sizes and the material platform used in our designs. The chemical compatibility of different steps were rigorously taken into consideration to achieve a reliable and repeatable fabrication process. The facilities operated by the Georgia Tech Institute for Electronics and Nanotechnology were used during our investigations. Specifically, the electron-beam lithography tool proved crucial in enabling the fabrication devices with smaller feature sizes that resulted in the demonstration of our GHz range pillar-based PnC structure.

The experimental demonstration of the pillar-based PnC membranes was based on a pillar-based PnC membrane composed of AlN thin film stacked on Mo and Si layers with Au pillars arranged in triangular lattice formation. Experimental evidence of the complete PnBG at the 800 MHz range was demonstrated for this structure. Our experimental measurements show a large attenuation of at least 20 dB in the Γ-Y, Γ-L, and Γ-K directions in the 760 MHz–820 MHz range, and this observation is in agreement with the FEM simulations.

To break the GHz barrier, we were able to modify our design of the pillar-based

PnC membranes to have a PnC with PnBG at 1.1 GHz. Based on this design, we developed and optimized a PnC-based waveguide structure that supported guided modes around 1050 MHz. The optimization process included careful selection of the geometrical dimensions of the structure as well as the frequency of operation that could be easily excited by the piezoelectric property of AlN. We were able to successfully demonstrate the waveguiding phenomenon in our designed structure, a result that was in reasonable agreement with our FEM simulations.

The successful demonstration of the wavguiding effect was the starting point for us to develop feasible designs for the resonators based on the pillar-based PnC membranes. We introduced two resonator designs based on the lateral resonance phenomenon as well as the waveguiding effect itself, which enabled a Fabry-Pérot resonator.

During the course of our experimental demonstration of both the PnBG and waveguiding effect, we developed numerical analysis techniques that could efficiently identify the polarization and symmetry properties of the theoretically calculated modes (i.e., modes surrounding the PnBG and the guided modes inside the PnBG). These techniques helped us to accurately justify the experimental results and assert their agreement with the theoretically expected results.

Additionally, we successfully demonstrated functional focusing IDTs to improve the coupling of the elastic waves to the waveguide modes. We were able to develop a simulation and design process that would efficiently produce the patterns for the electrodes of a focusing IDT specifically tailored for the desired operating frequency of the preselected guided mode of the waveguide. Our experimental results demonstrated the existence of an optimum focal point for the focusing IDTs and their effectiveness in examining the waveguiding phenomenon.

While the focus of our work in this thesis was based on PnC membranes, we also studied and developed several practical waveguide designs using the surface acoustic

waves. We optimized our designs, step-by-step, based on the results of our numerical calculations and our understanding of the physics of loss in the surface acoustic wave devices. We believe the waveguide designs developed in this thesis provide a feasible platform for the PnC-based GHz signal processing. Since these devices exist on the surface of thick substrates (i.e., compared to the wavelength), the overall geometry of these devices are different from that of the PnC membranes. Our decision to develop practical waveguides on thick substrates based on surface acoustic waves was informed by our experimental experience on the PnC membranes. The structural rigidity and straightforward fabrication process of the SAW-based PnC devices provide practical advantages over the fragile PnC membrane devices.

Considering the significance of the fast signal processing platforms in the current electronics industry, our findings open a new avenue in developing functional devices using PnC structures for such applications. However, the development of the PnC-based devices currently is at its infancy. Major practical and theoretical challenges remain to be resolved to unleash the potential of this versatile wave manipulating devices.

5.2 Future Directions

The next step in our investigation should be experimentally validating our SAW-based PnC designs and the waveguides developed based on them. Although we have strived for the design of theoretically and practically feasible devices, these devices still remain to be tested for their real-world performance. An important metric that should be the focus of these experimental demonstrations is the effect of the radiation loss on the performance of both the SAW-based PnCs and the waveguides based on them. The lessons learned from these measurements could prove crucial in the future development of such devices.

The requirement for the experimental validation of the theoretically sound devices

holds for our resonators based on the PnC membranes, as well. The effectiveness of the PnC layers in isolating the resonant modes, the upper bound on the quality factor imposed by the fabrication imperfection, and the inherent material loss can be studied during multiple rounds of experiments and design iterations. After all, our objective is to develop high-Q resonators that can be effectively integrated with other on-chip electronic elements.

The practical requirement for high-Q resonators as well as low-loss waveguides and PnCs demands deeper physical understanding and modeling techniques for the loss mechanisms such as viscoelastic damping, thermoelastic loss, electronic processes affecting the material loss specially in semiconductors, fabrication imperfection induced loss, friction modeling for the contact surfaces between different layers of the device, etc., and all of these mechanisms should be adapted and modified to effectively model the micron and sub-micron scale structures and thin films [9, 10, 21, 40, 55].

To be able to theoretically predict and optimize for the loss mechanisms, having access to reliable material properties is also of utmost importance. It is important to understand that most of the physical properties reported in the literature are for bulk materials. The data for thin films are scarce and the fact that different fabrication processes may result in slightly different physical properties (e.g., the difference between the evaporation, sputtering, and epitaxial growth techniques) makes this reality more challenging.

In the course of our design process in this thesis, we have always been wary of the fact that the AlN layer used in our devices makes the excitation of shear horizontal modes practically impossible. However, SH waves can prove advantageous as they do not exhibit significant out-of-plane displacement, resulting in experiencing lower loss of elastic energy caused by the interaction with the surrounding air or liquid. Engineering the c-axis of the AlN layer such that it can be used to excite SH waves, therefore, can be rewarding in terms of eliminating the vacuum packaging

requirements.

Finally, building practical integrated systems using the building blocks introduced in this thesis will always be the main objective in the future research projects focused on bringing the versatile PnC-based devices to mainstream applications such as signal processing, sensing, etc. The opportunities in this area are vast and the challenges seem insurmountable. However, in the course of this thesis, we have seen that PnC-based devices are flexible, both in terms of design parameters and possibility of envisioning different geometric arrangements for functional devices. This versatility is the most important advantage of this platform, i.e., the PnC-based wave manipulating devices.

Bibliography

[1] Achaoui, Y., Khelif, A., Benchabane, S., Robert, L., and Laude, V., "Experimental observation of locally-resonant and bragg band gaps for surface guided waves in a phononic crystal of pillars," *Physical Review B*, vol. 83, no. 10, p. 104201, 2011.

[2] Achaoui, Y., Laude, V., Benchabane, S., and Khelif, A., "Local resonances in phononic crystals and in random arrangements of pillars on a surface," *Journal of Applied Physics*, vol. 114, no. 10, p. 104503, 2013.

[3] Assouar, M. B. and Oudich, M., "Dispersion curves of surface acoustic waves in a two-dimensional phononic crystal," *Applied Physics Letters*, vol. 99, no. 12, p. 123505, 2011.

[4] Auld, B. A., *Acoustic fields and waves in solids*, vol. 2. Wiley New York, second ed., 1989.

[5] Bahr, B., Marathe, R., and Weinstein, D., "Theory and design of phononic crystals for unreleased cmos-mems resonant body transistors,"

[6] Bahr, B., Marathe, R., and Weinstein, D., "Phononic crystals for acoustic confinement in cmos-mems resonators," in *Frequency Control Symposium (FCS), 2014 IEEE International*, pp. 1–4, IEEE, 2014.

[7] Benchabane, S., Khelif, A., Rauch, J., Robert, L., and Laude, V., "Evidence for complete surface wave band gap in a piezoelectric phononic crystal," *Physical Review E*, vol. 73, no. 6, p. 065601, 2006.

[8] Campbell, C., *Surface acoustic wave devices for mobile and wireless communications*. Academic press, 1998.

[9] Caron, A. and Arnold, W., "Observation of local internal friction and plasticity onset in nanocrystalline nickel by atomic force acoustic microscopy," *Acta Materialia*, vol. 57, no. 15, pp. 4353–4363, 2009.

[10] Duffy Jr, W., "Acoustic quality factor of molybdenum and tungsten at low temperatures," *Journal of applied physics*, vol. 72, no. 12, pp. 5628–5634, 1992.

[11] El-Kady, I., Olsson, R., and Fleming, J., "Phononic band-gap crystals for radio frequency communications," *Applied Physics Letters*, vol. 92, no. 23, p. 233504, 2008.

[12] Gorisse, M., Benchabane, S., Teissier, G., Billard, C., Reinhardt, A., Laude, V., Defaÿ, E., and Aïd, M., "Observation of band gaps in the gigahertz range and deaf bands in a hypersonic aluminum nitride phononic crystal slab," *Applied Physics Letters*, vol. 98, no. 23, p. 234103, 2011.

[13] Hopkins, P. E., Reinke, C. M., Su, M. F., Olsson III, R. H., Shaner, E. A., Leseman, Z. C., Serrano, J. R., Phinney, L. M., and El-Kady, I., "Reduction in the thermal conductivity of single crystalline silicon by phononic crystal patterning," *Nano letters*, vol. 11, no. 1, pp. 107–112, 2010.

[14] Hsiao, F., Khelif, A., Moubchir, H., Choujaa, A., Chen, C., and Laude, V., "Complete band gaps and deaf bands of triangular and honeycomb water-steel phononic crystals," *Journal of applied physics*, vol. 101, no. 4, pp. 044903–044903, 2007.

[15] Hsu, J.-C. and Wu, T.-T., "Lamb waves in binary locally resonant phononic plates with two-dimensional lattices," *Applied physics letters*, vol. 90, no. 20, p. 201904, 2007.

[16] Huang, C.-Y., Sun, J.-H., and Wu, T.-T., "A two-port zno/silicon lamb wave resonator using phononic crystals," *Applied Physics Letters*, vol. 97, no. 3, p. 031913, 2010.

[17] Hung, C.-H., Wang, W.-S., Lin, Y.-C., Liu, T.-W., Sun, J.-H., Chen, Y.-Y., Esashi, M., and Wu, T.-T., "Design and fabrication of an at-cut quartz phononic lamb wave resonator," *Journal of Micromechanics and Microengineering*, vol. 23, no. 6, p. 065025, 2013.

[18] Hussein, M. I., Leamy, M. J., and Ruzzene, M., "Dynamics of phononic materials and structures: Historical origins, recent progress, and future outlook," *Applied Mechanics Reviews*, vol. 66, no. 4, p. 040802, 2014.

[19] Joannopoulos, J. D., Johnson, S. G., Winn, J. N., and Meade, R. D., *Photonic crystals: molding the flow of light*. Princeton university press, 2011.

[20] Joannopoulos, J. D., Villeneuve, P. R., and Fan, S., "Photonic crystals: putting a new twist on light," *Nature*, vol. 386, no. 6621, pp. 143–149, 1997.

[21] Jones, C. and Rayne, J., "Ultrasonic attenuation in tungsten and molybdenum up to 1 gc/s," *Physics Letters*, vol. 13, no. 4, pp. 282–283, 1964.

[22] Kafesaki, M., Sigalas, M., and Economou, E., "Elastic wave band gaps in 3-d periodic polymer matrix composites," *Solid state communications*, vol. 96, no. 5, pp. 285–289, 1995.

[23] Khelif, A., Aoubiza, B., Mohammadi, S., Adibi, A., and Laude, V., "Complete band gaps in two-dimensional phononic crystal slabs," *Physical Review E*, vol. 74, no. 4, p. 046610, 2006.

[24] Khelif, A., Achaoui, Y., and Aoubiza, B., "Surface acoustic waves in pillars-based two-dimensional phononic structures with different lattice symmetries," *Journal of Applied Physics*, vol. 112, no. 3, p. 033511, 2012.

[25] Khelif, A., Achaoui, Y., Benchabane, S., Laude, V., and Aoubiza, B., "Locally resonant surface acoustic wave band gaps in a two-dimensional phononic crystal of pillars on a surface," *Physical Review B*, vol. 81, no. 21, p. 214303, 2010.

[26] Khelif, A., Choujaa, A., Benchabane, S., Djafari-Rouhani, B., and Laude, V., "Experimental study of guiding and filtering of acoustic waves in a two dimensional ultrasonic crystal," *Zeitschrift für Kristallographie*, vol. 220, no. 9-10, pp. 836–840, 2005.

[27] Khelif, A., Mohammadi, S., Eftekhar, A. A., Adibi, A., and Aoubiza, B., "Acoustic confinement and waveguiding with a line-defect structure in phononic crystal slabs," *Journal of Applied Physics*, vol. 108, no. 8, pp. 084515–084515, 2010.

[28] Kittel, C. and McEuen, P., *Introduction to solid state physics*. Wiley New York, 8 ed., 1976.

[29] Kuo, N.-K. and Piazza, G., "Fractal phononic crystals in aluminum nitride: An approach to ultra high frequency bandgaps," *Applied Physics Letters*, vol. 99, no. 16, p. 163501, 2011.

[30] Kushwaha, M. S., "Stop-bands for periodic metallic rods: Sculptures that can filter the noise," *Applied Physics Letters*, vol. 70, no. 24, pp. 3218–3220, 1997.

[31] Kushwaha, M. S., Halevi, P., Dobrzynski, L., and Djafari-Rouhani, B., "Acoustic band structure of periodic elastic composites," *Physical Review Letters*, vol. 71, no. 13, p. 2022, 1993.

[32] Kushwaha, M. and Djafari-Rouhani, B., "Complete acoustic stop bands for cubic arrays of spherical liquid balloons," *Journal of applied physics*, vol. 80, no. 6, pp. 3191–3195, 1996.

[33] Kushwaha, M. and Djafari-Rouhani, B., "Sonic stop-bands for periodic arrays of metallic rods: honeycomb structure," *Journal of sound and vibration*, vol. 218, no. 4, pp. 697–709, 1998.

[34] Kushwaha, M., Halevi, P., Martinez, G., Dobrzynski, L., and Djafari-Rouhani, B., "Theory of acoustic band structure of periodic elastic composites," *Physical Review B*, vol. 49, no. 4, p. 2313, 1994.

[35] Larabi, H., Pennec, Y., Djafari-Rouhani, B., and Vasseur, J., "Multicoaxial cylindrical inclusions in locally resonant phononic crystals," *Physical Review E*, vol. 75, no. 6, p. 066601, 2007.

[36] Laude, V., Gérard, D., Khelfaoui, N., Jerez-Hanckes, C. F., Benchabane, S., and Khelif, A., "Subwavelength focusing of surface acoustic waves generated by an annular interdigital transducer," *Applied Physics Letters*, vol. 92, no. 9, p. 094104, 2008.

[37] Laude, V., Wilm, M., Benchabane, S., and Khelif, A., "Full band gap for surface acoustic waves in a piezoelectric phononic crystal," *Physical Review E*, vol. 71, no. 3, p. 036607, 2005.

[38] Lin, S.-C. S., Huang, T. J., Sun, J.-H., and Wu, T.-T., "Gradient-index phononic crystals," *Physical Review B*, vol. 79, no. 9, p. 094302, 2009.

[39] Lin, S.-C. S., Tittmann, B. R., Sun, J.-H., Wu, T.-T., and Huang, T. J., "Acoustic beamwidth compressor using gradient-index phononic crystals," *Journal of Physics D: Applied Physics*, vol. 42, no. 18, p. 185502, 2009.

[40] Lindenfeld, Z. and Lifshitz, R., "Damping of mechanical vibrations by free electrons in metallic nanoresonators," *Physical Review B*, vol. 87, no. 8, p. 085448, 2013.

[41] Liu, Z., Zhang, X., Mao, Y., Zhu, Y., Yang, Z., Chan, C., and Sheng, P., "Locally resonant sonic materials," *Science*, vol. 289, no. 5485, pp. 1734–1736, 2000.

[42] Maldovan, M. and Thomas, E., "Simultaneous complete elastic and electromagnetic band gaps in periodic structures," *Applied Physics B*, vol. 83, no. 4, pp. 595–600, 2006.

[43] Martinezsala, R., Sancho, J., Sánchez, J., Gómez, V., Llinares, J., and Meseguer, F., "Sound-attenuation by sculpture," *nature*, vol. 378, no. 6554, p. 241, 1995.

[44] Miyashita, T., "Sonic crystals and sonic wave-guides," *Measurement Science and Technology*, vol. 16, no. 5, p. R47, 2005.

[45] Miyashita, T. and Inoue, C., "Numerical investigations of transmission and waveguide properties of sonic crystals by finite-difference time-domain method," *Japanese Journal of Applied Physics*, vol. 40, no. 5S, p. 3488, 2001.

[46] Mohammadi, S., Eftekhar, A., Khelif, A., Hunt, W., and Adibi, A., "Evidence of large high frequency complete phononic band gaps in silicon phononic crystal plates," *Applied Physics Letters*, vol. 92, no. 22, pp. 221905–221905, 2008.

[47] Mohammadi, S. and Adibi, A., "On chip complex signal processing devices using coupled phononic crystal slab resonators and waveguides," *AIP Advances*, vol. 1, no. 4, pp. 041903–041903, 2011.

[48] Mohammadi, S., Eftekhar, A., Khelif, A., Moubchir, H., Westafer, R., Hunt, W., and Adibi, A., "Complete phononic bandgaps and bandgap maps in two-dimensional silicon phononic crystal plates," *Electronics Letters*, vol. 43, no. 16, pp. 898–899, 2007.

[49] Mohammadi, S., Eftekhar, A. A., Pourabolghasem, R., and Adibi, A., "Simultaneous high-q confinement and selective direct piezoelectric excitation of flexural and extensional lateral vibrations in a silicon phononic crystal slab resonator," *Sensors and Actuators A: Physical*, vol. 167, no. 2, pp. 524–530, 2011.

[50] Mohammadi, S., Eftekhar, A. A., Hunt, W. D., and Adibi, A., "High-q micromechanical resonators in a two-dimensional phononic crystal slab," *Applied Physics Letters*, vol. 94, p. 051906, 2009.

[51] Olsson Iii, R. and El-Kady, I., "Microfabricated phononic crystal devices and applications," *Measurement Science and Technology*, vol. 20, no. 1, p. 012002, 2009.

[52] Olsson III, R. H., El-Kady, I. F., Su, M. F., Tuck, M. R., and Fleming, J. G., "Microfabricated vhf acoustic crystals and waveguides," *Sensors and Actuators A: Physical*, vol. 145, pp. 87–93, 2008.

[53] Oudich, M., Li, Y., Assouar, B. M., and Hou, Z., "A sonic band gap based on the locally resonant phononic plates with stubs," *New Journal of Physics*, vol. 12, no. 8, p. 083049, 2010.

[54] Oudich, M., Senesi, M., Assouar, M. B., Ruzenne, M., Sun, J.-H., Vincent, B., Hou, Z., and Wu, T.-T., "Experimental evidence of locally resonant sonic band gap in two-dimensional phononic stubbed plates," *Physical Review B*, vol. 84, no. 16, p. 165136, 2011.

[55] Papadakis, E. P., "Ultrasonic attenuation caused by scattering in polycrystalline media," *Physical acoustics*, vol. 4, no. Part B, pp. 269–328, 2012.

[56] Pennec, Y., Rouhani, B., Larabi, H., Akjouj, A., Gillet, J., Vasseur, J., and Thabet, G., "Phonon transport and waveguiding in a phononic crystal made up of cylindrical dots on a thin homogeneous plate," *Physical Review B*, vol. 80, no. 14, p. 144302, 2009.

[57] Pennec, Y., Djafari-Rouhani, B., Vasseur, J., Khelif, A., and Deymier, P., "Tunable filtering and demultiplexing in phononic crystals with hollow cylinders," *Physical Review E*, vol. 69, no. 4, p. 046608, 2004.

[58] Pourabolghasem, R., Khelif, A., Eftekhar, A., Mohammadi, S., and Adibi, A., "Phononic bandgaps in silicon plate with metallic pillars," *Electronics letters*, vol. 48, no. 18, pp. 1147–1148, 2012.

[59] Pourabolghasem, R., Khelif, A., Mohammadi, S., Eftekhar, A. A., and Adibi, A., "Physics of band-gap formation and its evolution in the pillar-based phononic crystal structures," *Journal of Applied Physics*, vol. 116, no. 1, p. 013514, 2014.

[60] Sánchez-Pérez, J., Caballero, D., Martinez-Sala, R., Rubio, C., Sánchez-Dehesa, J., Meseguer, F., Llinares, J., and Gálvez, F., "Sound attenuation by a two-dimensional array of rigid cylinders," *Physical Review Letters*, vol. 80, no. 24, p. 5325, 1998.

[61] Sankaranarayanan, S. K. and Bhethanabotla, V. R., "Design of efficient focused surface acoustic wave devices for potential microfluidic applications," *Journal of Applied Physics*, vol. 103, no. 6, p. 064518, 2008.

[62] Senturia, S. D., *Microsystem design*. Kluwer academic publishers Boston, 2001.

[63] Sigalas, M. and Economou, E., "Band structure of elastic waves in two dimensional systems," *Solid State Communications*, vol. 86, no. 3, pp. 141–143, 1993.

[64] Sigalas, M., Kushwaha, M. S., Economou, E. N., Kafesaki, M., Psarobas, I. E., and Steurer, W., "Classical vibrational modes in phononic lattices: theory and experiment," *Zeitschrift für Kristallographie*, vol. 220, no. 9-10, pp. 765–809, 2005.

[65] Sigalas, M. and Economou, E., "Elastic and acoustic wave band structure," *Journal of Sound Vibration*, vol. 158, pp. 377–382, 1992.

[66] Soliman, Y., Su, M., Leseman, Z., Reinke, C., El-Kady, I., and Olsson III, R., "Phononic crystals operating in the gigahertz range with extremely wide band gaps," *Applied physics letters*, vol. 97, no. 19, p. 193502, 2010.

[67] Su, M., Olsson III, R., Leseman, Z., and El-Kady, I., "Realization of a phononic crystal operating at gigahertz frequencies," *Applied Physics Letters*, vol. 96, no. 5, p. 053111, 2010.

[68] Sun, J.-H. and Wu, T.-T., "Analyses of mode coupling in joined parallel phononic crystal waveguides," *Physical Review B*, vol. 71, no. 17, p. 174303, 2005.

[69] Sun, J.-H. and Wu, T.-T., "Propagation of surface acoustic waves through sharply bent two-dimensional phononic crystal waveguides using a finite-difference time-domain method," *Physical Review B*, vol. 74, no. 17, p. 174305, 2006.

[70] Sun, J.-H. and Wu, T.-T., "Propagation of acoustic waves in phononic-crystal plates and waveguides using a finite-difference time-domain method," *Physical Review B*, vol. 76, no. 10, p. 104304, 2007.

[71] Tanaka, Y. and Tamura, S.-i., "Surface acoustic waves in two-dimensional periodic elastic structures," *Physical Review B*, vol. 58, no. 12, p. 7958, 1998.

[72] Wang, X., Kushwaha, M., and Vasilopoulos, P., "Tunability of acoustic spectral gaps and transmission in periodically stubbed waveguides," *Physical Review B*, vol. 65, no. 3, p. 035107, 2001.

[73] Wang, Z., Tang, T., Chen, S., and Chen, B., "Field analysis and calculation of interdigital transducers with arbitrary finger shapes," *Journal of Physics D: Applied Physics*, vol. 39, no. 22, p. 4902, 2006.

[74] Wu, T.-T., Chen, Y.-T., Sun, J.-H., Lin, S.-C. S., and Huang, T. J., "Focusing of the lowest antisymmetric lamb wave in a gradient-index phononic crystal plate," *Applied Physics Letters*, vol. 98, no. 17, p. 171911, 2011.

[75] Wu, T.-T., Hsu, J.-C., and Sun, J.-H., "Phononic plate waves," *Ultrasonics, Ferroelectrics and Frequency Control, IEEE Transactions on*, vol. 58, no. 10, pp. 2146–2161, 2011.

[76] Wu, T.-T., Tang, H.-T., Chen, Y.-Y., and Liu, P.-L., "Analysis and design of focused interdigital transducers," *Ultrasonics, Ferroelectrics, and Frequency Control, IEEE Transactions on*, vol. 52, no. 8, pp. 1384–1392, 2005.

[77] Wu, T., Huang, Z., Tsai, T., and Wu, T., "Evidence of complete band gap and resonances in a plate with periodic stubbed surface," *Applied Physics Letters*, vol. 93, no. 11, pp. 111902–111902, 2008.

[78] Wu, T.-C., Wu, T.-T., and Hsu, J.-C., "Waveguiding and frequency selection of lamb waves in a plate with a periodic stubbed surface," *Physical Review B*, vol. 79, no. 10, p. 104306, 2009.

[79] Ziaei-Moayyed, M., Su, M., Reinke, C., El-Kady, I., and Olsson, R., "Silicon carbide phononic crystal cavities for micromechanical resonators," in *Micro Electro Mechanical Systems (MEMS), 2011 IEEE 24th International Conference on*, pp. 1377–1381, IEEE, 2011.

VITA

Reza Pourabolghasem received his B.S. in Electrical Engineering from Sharif University of Technology in 2007, where his B.S. project was on materials with a negative refractive index. He worked towards his Ph.D. in the Photonics Research Group in Georgia Institute of Technology since May 2009, under the supervision of Professor Ali Adibi. Reza's research is focused on phononic devices with applications in wireless communications and sensing. Reza ranked first in Iran's nationwide universities entrance examination for undergraduate studies in August 2003. He has also ranked first in the Ph.D. preliminary exam at Georgia Tech in 2009 and has won Oscar P. Cleaver award in recognition of his accomplishment.